BOSTON UNIVERSITY

COLLEGE OF ENGINEERING

Dissertation

ENGINEERING PHOTONIC AND PLASMONIC LIGHT EMISSION ENHANCEMENT

by

NATHANIEL LAWRENCE

B.S., University of Richmond, 2008
M.S., Boston University, 2012

Submitted in partial fulfillment of the

requirements for the degree of

Doctor of Philosophy

2013

Approved by

First Reader

Luca Dal Negro, PhD
Associate Professor of Electrical and Computer Engineering

Second Reader

Jonathan Klamkin, PhD
Assistant Professor of Electrical and Computer Engineering

Third Reader

Anna Swan, PhD
Associate Professor of Electrical and Computer Engineering

Fourth Reader

Siddharth Ramachandran, PhD
Associate Professor of Electrical and Computer Engineering

The solutions are all simple...after you've already arrived at them. But they're simple only when you already know what they are.

-Robert Pirsig, Zen and the Art of Motorcycle Maintenance

Acknowledgments

First, I would like to thank my advisor, Prof. Luca Dal Negro. Without his daily input this work would not have been possible. Whether it was hours spent pouring over textbooks and data or troubleshooting code and experiments he maintained a high level of involvement in all aspects of my work. I would also like to thank the NSF for funding my time in graduate school through the NSF Career Award (No. ECCS-0846651). Additionally, a thank you is due to the members of my committee, Prof. Jonathan Klamkin, Prof. Anna Swan and Prof. Siddharth Ramachandran for their valuable assistance and feedback on this thesis.

I would also like to thank the members of the Nanomaterials and Nanostructure Optics lab group, both past and present, who have been there on a daily basis to learn with me, work through problems and, at times, commiserate failures. Their importance is such that they should be named individually so thank you, Jacob Trevino, Dr. Emanuele Pecora, Dr. Gary Walsh, Dr. Svetlana Boriskina, Dr. Carlo Forestiere, Travis Rich, Dr. Alyssa Pasquale, Dr. Sylvanus Lee, Dr. Selcuk Yerci, Dr. Rui Li, Dr. Ashwin Gopinath, Alex Handin, Dr. Antonio Capretti, Patrick Gregg, Dianmin Lin, Yu Wang, Giuliana Di Martino and Tom Murphy.

I would next like to thank collaborators I have worked with throughout the completion of my degree. I had the opportunity to work at Lawrence Berkeley National labs for some time which was an excellent experience. I would like to thank Dr. Stefano Cabrini and other members of the Molecular Foundry for their assistance. Thank you to Prof. Alexander Sergienko, Dr. David Simon and Andrew Fraine, who worked with us on applications of Vogel spiral OAM for secure optical communication. Also, I would like to thank Dr. Alessia Irrera and Prof. Francesco Priolo who collaborated with us on Si nanowire work. Finally, I would like to thank Dr. Francesca Intonti, Niccolo Caselli and Prof. Diederik Wiersma who collaborated with us to investigate the near field scattering

of Vogel spirals.

Next, I would like to thank the staff and other students of the photonics center who's efforts keep the facilities I have relied on for the last 5 years running. In particular Paul Mak has done has an amazing job of keeping the Optoelectronic Processing Facility running and is always quick to respond to any issues that arise. Additionally, a thank you is owed to Alket Mirteri, Ronen Adato and Alex Reddington for their assistance and guidance both as colleagues and more importantly as friends.

Last but certainly not least, I would like to thank my friends and family who have been incredibly supportive of all my efforts. First my parents and my sister, I love you, thank you for always being there. Next I would like to thank Alexis Fedorchak for her daily emotional support, you have made each day brighter. To my numerous friends in Boston, thanks for the great time. I have formed many close friendships that I hope will last a lifetime, including with many of those already mentioned by name. To those not included individually yet, your support was no less important, thank you, Stefan Yohe, Ed Reznik, Margo Monroe, Eric Falde, Tim Ford, Kyle Pearson, Joe Wang, Christen Bailey and Zach Sun.

ENGINEERING PHOTONIC AND PLASMONIC LIGHT EMISSION ENHANCEMENT

(Order No.)

NATHANIEL LAWRENCE

Boston University, College of Engineering, 2013

Major Professor: Luca Dal Negro, PhD, Associate Professor,
Electrical and Computer Engineering
Materials Science and Engineering

ABSTRACT

Semiconductor photonic devices are a rapidly maturing technology which currently occupy multi-billion dollar markets in the areas of LED lighting and optical data communication. LEDs currently demonstrate the highest luminous efficiency of any light source for general lighting. Long-haul optical data communication currently forms the backbone of the global communication network. Proper design of light management is required for photonic devices, which can increase the overall efficiency or add new device functionality. In this thesis, novel methods for the control of light propagation and confinement are developed for the use in integrated photonic devices.

The first part of this work focuses on the engineering of field confinement within deep subwavelength plasmonic resonators for the enhancement of light-matter interaction. In this section, plasmonic ring nanocavities are shown to form gap plasmon modes confined to the dielectric region between two metal layers. The scattering properties, near-field enhancement and photonic density of states of nanocavity devices are studied using analytic theory and 3D finite difference time domain simulations. Plasmonic ring

nanocavities are fabricated and characterized using photoluminescence intensity and decay rate measurements. A 25 times increase in the radiative decay rate of Er:SiO_2 is demonstrated in nanocavities where light is confined to volumes as small as $0.01(\frac{\lambda}{n})^3$. The potential to achieve lasing, due to the enhancement of stimulated emission rate in ring nanocavities, is studied as a route to Si-compatible plasmon-enhanced nanolasers.

The second part of this work focuses on the manipulation of light generated in planar semiconductor devices using arrays of dielectric nanopillars. In particular, aperiodic arrays of nanopillars are engineered for omnidirectional light extraction enhancement. Arrays of Er:SiN_x nanopillars are fabricated and a ten times increase in light extraction is experimentally demonstrated, while simultaneously controlling far-field radiation patterns in ways not possible with periodic arrays. Additionally, analytical scalar diffraction theory is used to study light propagation from Vogel spiral arrays and demonstrate generation of OAM. Using phase shifting interferometry, the presence of OAM is experimentally verified. The use of Vogel spirals presents a new method for the generation of OAM with applications for secure optical communications.

Contents

List of Tables

List of Figures

Chapter 1

Introduction

The development of photonic devices which generate, modulate and detect light has been a rapidly growing research field and commercial technology in the past few decades. A wide range of applications are addressed in photonics including solar energy harvesting, solid state lighting, optical data communication and optical chemical and biological sensing. Ultimately, optical signals are converted to electronic ones which can be integrated with microelectronic technology. In many cases materials research and processing techniques developed for and used in the solid state electronics industry can be leveraged for semiconductor photonic devices in an effort to move towards cheap, scalable production and integration of photonic devices with microelectronics. This work focuses on the optical design, implementation and demonstration of novel methods for the trapping and control of light propagation most applicable to solid state lighting and integrated optical data communication. A brief overview of the challenges faced in these two areas are addressed which gives a context for this thesis.

1.1 Integrated Photonic Data Processing

As information technology advances, one of the growing limitations to overall system performance is becoming electronic data links (wires). The bandwidth of electronic communication is limited by parasitic heating and crosstalk in highly integrated systems. This limitation can be alleviated by replacing electronic links with optical ones where significantly higher data rates are possible.(Miller, 2009) In an optical data link an elec-

tronic signal is converted into an optical one, transmitted to a remote location and then converted back into an electronic signal. To accomplish this a coherent light source is needed which is either modulated directly or with an external modulator. Moreover, a waveguide is needed to transmit the signal and a photodetector. A layout for a photonic integrated circuit, aimed at terabit/s data transfer with 80 parallel data channels is shown in Figure 1·1. As the demand for bandwidth grows, photonic integrated circuits are becoming more complex requiring the integration of large numbers of individual components(Nagarajan et al., 2012). Additionally, as system size and data rates grow, integration of optical components with electrical ones will become increasingly important. For these requirements to be met, low cost, scalable systems of photonic integrated components, similar to electronic ones are crucial. One route to cheap scalable photonic components is the use of Si-based materials(Pavesi and Guillot, 2006).

1.1.1 Silicon Photonics

Silicon electronic technology has enabled the computer and telecommunications revolution that has become ubiquitous in modern society with the number of transistors on a chip growing exponentially (Moore's Law) over the last 40 years. Silicon microelectronics can now be made reliably at very low cost on an extremely large scale. However, due to the indirect bandgap of silicon, light absorption and emission processes are extremely inefficient(Ossicini et al., 2004). While compound semiconductor materials provide a fairly versatile platform for devices capable of light generation, modulation and detection(Nagarajan et al., 2012), devices based on these materials are extremely expensive compared to Si based ones. Additionally, these semiconductor materials are not compatible with CMOS processing making the monolithic integration of these devices with Si based photonic or electronic devices challenging. A large amount of research has focused on the development of Si-based or CMOS compatible photonic devices for integrated op-

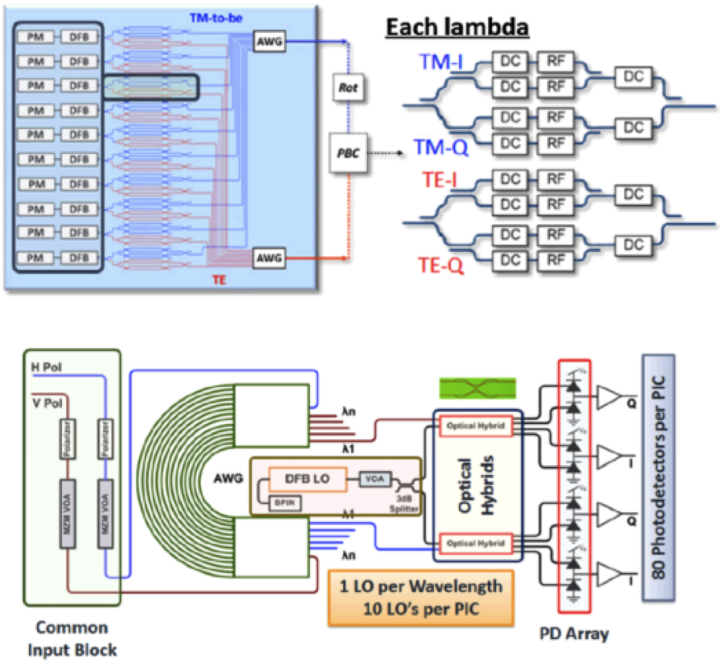

Figure 1·1: Schematic of a photonic integrated circuit intended to deliver terabit/s data transfer. On top is the layout of the transmit chip with integrated, tunable. distributed feedback lasers and Mach-Zender modulators. On bottom is the layout of the receive chip with wavelength demodulation, local oscillators and high speed photodiodes for coherent detection.(Nagarajan et al., 2012)

tical data processing(Ossicini et al., 2004). High quality Si waveguides, modulators and detectors have been demonstrated(Pavesi and Lockwood, 2004; Kang et al., 2008; Liu et al., 2007; Xu et al., 2005). Optically excited Si or Si-based lasers have been demonstrated(Liu et al., 2010; Rong et al., 2005), however electrically excited lasers Si lasers are still the topic of much research. Current methods for light generation in Si photonic circuits rely on optical gain in compound semiconductor chips which are bonded to Si chips.(Fang et al., 2006)

1.1.2 Silicon Light Emission

One of the challenges in creating Si light sources comes form the indirect bandgap of Si. In materials with an indirect bandgap, transfer of charge carriers between the valence and conduction bands requires a change in wavevector which cannot be provided by a photon. A schematic of the Si band diagram is shown in Figure 1·2(Pavesi, 2008). For electronic transitions to occur near the band edges interaction with a phonon is required, making the process much less likely to occur. The typical time scale of light emission in Si, called the radiative lifetime, is in the ms range. The non-radiative mechanisms in Si, such as Auger recombination, are quite efficient(Pavesi, 2008; Ossicini et al., 2004), making the non radiative lifetime very fast and the intrinsic quantum efficiency for Si very low, $\approx 10^{-4} - 10^{-5}$. For direct gap semiconductors the internal quantum efficiency is much higher, on the order of 10^{-1}. To make light emission in Si more efficient either the radiative lifetime must decreased or the non-radiative lifetime increased.

Many approaches have been taken to make Si-based, optically active devices through materials engineering. The creation of Si nanostructures has also been widely explored where the quantum confinement of excitons can alter light emission processes. Here, light emission and even optical gain have been observed from Si nanocrystals(Pavesi et al., 2000). Additionally, strong light emission has been observed from Si nanowires(Irrera

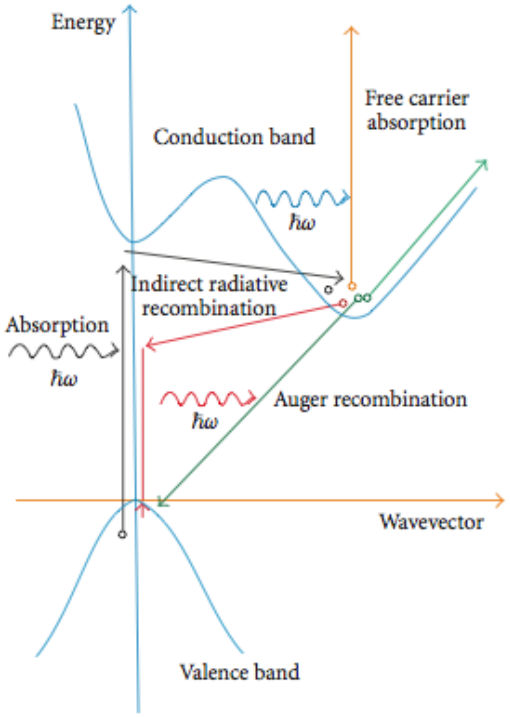

Figure 1·2: Simplified band structure of bulk Si with various transitions shown including Auger recombination, radiative recombination and free carrier absorption.(Pavesi, 2008)

et al., 2012; Guichard et al., 2006; Sivakov et al., 2010). Studies of Si superlattices(Lu et al., 1995; Ruan et al., 2003; Dal Negro et al., 2008; Warga et al., 2008) have also shown light emission. While significant progress has been made, light emission from these structures, typically in the visible, is not compatible with Si waveguides since photon energies are above the Si bandgap.

Some of the attempts include doping Si with other elements to create traps where Si excitons can be confined and radiatively recombine(Ossicini et al., 2004). Er ion doping in particular has received much attention due the possibility of generating light at $1.55\mu m$ from the ${}^4I_{13/2}$ to the ${}^4I_{15/2}$ energy state transition in the Er^{3+} ion(Becker et al., 1999). However, energy back transfer has lead to inefficient luminescence in cSi.

The Er doping of c-Si has proved ineffective, however Er doping of Si-based materials, such as SiO_2, has shown very efficient light emission and relatively broadband gain. Er emission, at $1.55\mu m$, also coincides with the absorption minima of silica fibers. For these reasons Er-doped fiber amplifiers and lasers form the backbone of the current global long-haul communication network(Desurvine, 1994). However, the small absorption cross section ($\sigma \approx 4 \times 10^{-21} cm^2$)(Becker et al., 1999), low level of possible Erbium doping due to the onset of clustering, and typically low activation percentage of Er ions, limits the achievable gain. In fiber based devices low gain can be offset with long interaction lengths and high Q resonators, however the geometry of on-chip optical sources is limited. Thus far, the low optical gain, and difficulty of electrical current injection has limited the use of Er:SiO_2 for on-chip optical sources.

To increase the absorption cross section, Er-doped materials with Si nanocrystals have been studied. In these materials energy absorbed in the relatively large Si nanocrystals can be transferred to the Er ions(Kik et al., 2000; Priolo et al., 2001). The presence of Si nanocrystals can also facilitate electrical pumping(Iacona et al., 2002; Pacifici et al., 2003). Excitation cross sections of $\approx 10^{-16} cm^2$ have been demonstrated, but free-

carrier absorption has prevented the realization of optical gain(Kik and Polman, 2002). Er-doping of Si-rich SiN_x has also shown significant increases of absorption cross section in amorphous materials(Yerci et al., 2009). In these materials the SiN_x matrix can be pumped over a wide energy range and energy transfer to Er has been shown with strong emission at $1.55\mu m$(Yerci, 2011; Yerci et al., 2010). Moreover, fast energy transfer to Er ions is observed, causing a significant reduction in free carrier absorption(Li et al., 2008; Li, 2010). The increased refractive index of SiN_x over SiO_2 makes it a preferable material for the creation of on-chip optical devices.

Despite significant material advances, Er-doped Si-based materials still exhibit low gain and have not proved effective for on-chip coherent optical sources. One method to increase this relatively weak light emission is by engineering the local density of photonic states (PDOS). By increasing the PDOS in optical micro/nanocavities (Purcell effect), increases in the radiative emission rate, quantum efficiency and stimulated emission rate can be realized(Vahala, 2003). Purcell enhancement in both photonic and plasmonic nanocavities has been studied in a large variety of resonant cavities including many examples of enhanced Er light emission(Gopinath et al., 2010; Schubert et al., 1993; Creatore et al., 2009; Bao et al., 2007; Gong et al., 2010a; Kroekenstoel et al., 2009; Gong et al., 2010b; Vredenberg et al., 1993). The focus of this thesis is the development of plasmonic and photonic devices for the enhancement of Er-based light emission in Si materials.

1.2 Review of Optical Micro/Nanocavities

The goal of this thesis is the enhancement of Er light emission, however the same principles can be applied to other material systems. In this section, an overview of photonic and plasmonic optical resonators is given along with a discussion of the advantages and disadvantages of each. The discussion presented here is by no means an exhaustive

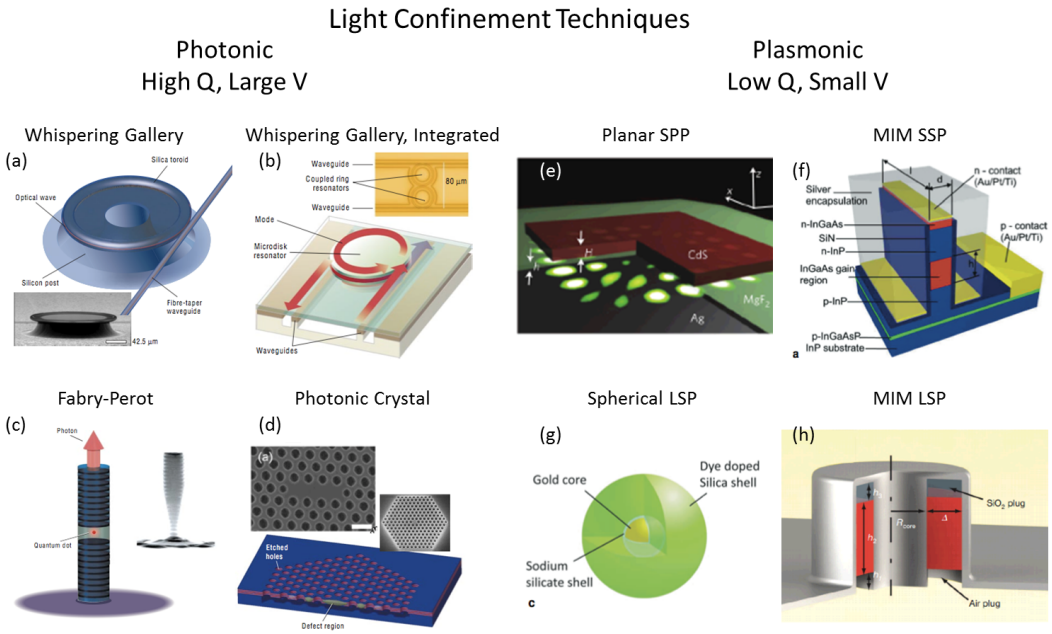

Figure 1·3: (a) Micro-toroidal photonic resonator (Armani et al., 2003) (b) Micro-disk cavity (Djordjev et al., 2002a; Choi et al., 2003; Djordjev et al., 2002b) (c) Fabry-Perot cavity formed by distributed Bragg reflectors (Vučković et al., 2002; Pelton et al., 2002) (d) Photonic crystal defect cavity (Gong et al., 2010b; Painter et al., 1999) (e) SPP laser (Ma et al., 2010) (f) MIM SPP laser (Hill et al., 2009) (g) Spherical nanoparticle SPASER (Noginov et al., 2009) (h) MIM coaxial laser (Khajavikhan et al., 2012)

study of optical cavities, which is a rich field with a wide range of applications. This discussion will focus on optical resonators for use in producing coherent radiation for on-chip data communication. The devices investigated here have been broken into two broad categories, those that use purely dielectric materials, photonic, and those that incorporate metals for the formation of surface plasmons, plasmonic. Photonic resonators typically have higher Q factors than plasmonic devices, but the optical mode size is diffraction limited. The excitation of surface plasmons allows for light confinement below the diffraction limit, but absorption in metallic layers limits the Q factor.

1.2.1 Photonic Microcavities

The first type of photonic microcavity investigated here is a micro-toroidal resonator (Armani et al., 2003; Polman et al., 2004). The micro-toroidal resonator depicted in Figure 1·3 (a) is made of a toroid of silica $120\mu m$ in diameter. Micro-toroidal resonators can have ultra-high Q factors in excess of 10^8 where whispering gallery modes are excited. The optical mode in a micro-toroid travels around the outside of the structure where it is confined by total internal reflection. Realization of ultra-high Q factors also depends on low material losses, making silica the material of choice and operation around $1.55\mu m$ typical. While the Q factors in micro-toroids are very high, coupling to and from the cavity is typically achieved using a tapered optical fiber, making integration with other devices on chip difficult. Additionally, the suspended nature of these devices makes electrical injection challenging, a requirement for light sources used in on-chip data processing. While the geometry of micro-toroidal resonators makes integration challenging, micro-disk resonators (as depicted in Figure 1·3 (b)) can readily be integrated with on-chip optical waveguides. Since micro-disk structures are not suspended, confinement of light requires the use of materials with higher index than silica (due to substrate effects), which typically also have larger losses. The changes in material choice and geometry lowers the Q factor to $\approx 10^4$. Micro-disk structures are commonly employed for on-chip resonators and add-drop filters(Djordjev et al., 2002a; Choi et al., 2003; Djordjev et al., 2002b). Micro-disk resonators also have significantly smaller mode volumes than micro-toroidal resonators, as small as $\approx 6(\lambda/n)^3$. Suspended micro-disk resonators have also been studied, including demonstration of lasing with Er(Kippenberg et al., 2006). However, suspended micro-disks, like micro-toroids, cannot be easily integrated or electrically pumped.

Another type of widely used photonic resonator is the Fabry-Perot (FP) microcavity. Photonic FP cavities, shown in Figure 1·3 (c), are typically formed by distributed Bragg

reflectors (DBRs). Due to the versatility of these microcavities, which can be formed vertically or horizontally, and their small overall size, FP cavities with DBR mirrors are widely used for semiconductor lasers. The reflectivity of DBR mirrors can be tuned electronically by applying external voltage to the device. In particular, by independently tuning the reflectivity of both mirrors, sampled grating distributed Bragg reflector (SGDBR) lasers(Jayaraman et al., 1993; Barton et al., 2003) can be tuned over wide wavelength ranges and are commonly used in photonic integrated circuits(Nagarajan et al., 2012). Modification of spontaneous emission in FP cavities has also been demonstrated(Solomon et al., 2000; Gerard et al., 1996) with Q factors of $\approx 10^3$ and mode volumes of $\approx 5(\lambda/n)^3$. As discussed in detail later in this thesis, large Purcell enhancement of Er light emission cannot be achieved with high Q factor alone, but requires the use of cavities with small mode volume. Photonic cavities with the smallest mode volume are those formed by defects in photonic crystals (PhCs), as shown in Figure 1·3 (d). Optical bandgaps can form in PhCs where light is forbidden to propagate at certain wavelengths. When made with a defect, light will be confined inside the defect region forming a photonic crystal microresonator(Painter et al., 1999; Altug et al., 2006; Gong et al., 2010b; Akahane et al., 2003). High Q factors, $\approx 6 \times 10^5$ and small mode volumes, $\approx 1(\lambda/n)^3$, make these promising photonic structures for achievement of large Purcell factors. Two-dimensional PhCs can be chip integrated and light can be coupled with waveguide structures. One drawback to PhC resonators is that while the optical mode size is small, the overall device footprint can be quite large. As with all photonic cavities, the mode size is still limited by diffraction.

1.2.2 Plasmonic Microcavities

The second class of micro-resonators relies of the formation of plasmon polaritons, allowing the confinement of light past the diffraction limit, but at the cost of increased

absorption. Figure 1·3 (e) shows a plasmonic laser where planar surface plasmon polaritons (SPPs) are formed on a Ag film and confined to an optically active region of CdS(Ma et al., 2010). A highly confined plasmon mode is formed on the Ag and the index contrast at the edges of the CdS provides reflection, forming a nanocavity. A Q factor of 450 was displayed in this device along with a mode volume of $8(\lambda/n)^3$. Lasing is achieved at 500 nm and a Purcell factor of 14 is demonstrated. The mode size in this device is limited vertically by the decay length of the field into the dielectric region. The polariton decay length can be decreased further by the excitation of gap plasmons, where modes are limited by the size of dielectric gap regions. Gap plasmon modes can exhibit strong field confinement with a large portion of energy confined to the dielectric region between two metal layers(Maier, 2006). Figure 1·3 (f) shows a metal-insulator-metal (MIM) nanocavity laser which operates at $1.5\mu m$. In this device a slab InGaAs is encapsulated in Ag to form a plasmonic MIM nanocavity with a Q factor of 140 and volume of $1(\lambda/n)^3$(Hill et al., 2009). This device is particularly interesting as lasing is observed under electrical excitation, however the mode volume is relatively large due to the length of the device.

Both plasmonic nanocavities presented so far rely on the formation of SPPs. In this case the mode size is still diffraction limited in the direction of propagation. While this approach is promising, smaller mode volumes can be achieved by the excitation of localized surface plasmons (LSPs) with plasmonic field confinement in all three dimensions. Figure 1·3 (g) shows a surface plasmon laser (SPASER) which is formed around a spherical metal nanoparticle(Noginov et al., 2009). A 14nm diameter Au particle is coated with a gain medium, and suspended in solution, which displays lasing at 525nm. The SPASER has a mode volume of $0.001(\lambda/n)^3$ but a Q factor of only 14. While the mode volume is very low, this approach is impractical for on-chip integration as it is solution based. The simplicity of the geometry also leaves little room for tuning the

wavelength response of the nanocavity. By taking advantage of both LSP, and gap plasmon formation, even smaller mode volumes can be achieved in more versatile devices. Figure 1·3 (h) shows a circular MIM resonator which has been used to demonstrate lasing at $1.55\mu m$ with an InGaAsP gain medium. Here plasmon modes, which occupy the dielectric region between two circular metallic layers, confine light to a volume of $.14(\lambda/n)^3$ with a Q factor of 50(Khajavikhan et al., 2012). Additionally, passive devices based on this geometry have been demonstrated with modes volumes as small as $0.0015(\lambda/n)^3$(Melli et al., 2013) and theoretical studies have shown mode volumes as small as $0.00073(\lambda/n)^3$(Vesseur et al., 2010). By changing the geometry, mode tunability over a wide wavelength range can be achieved, providing a versatile on-chip platform for deep subwavelength light confinement.

In this thesis, a novel method for the deep subwavelength confinement of light in plasmonic nanocavities is presented using Si-based Er-doped materials. Devices based on this concept are designed, fabricated and characterized showing strong Purcell enhancement of light emission. A perspective is given on the possibility of achieving laser action for nanoscale Er-doped Si-based sources.

1.3 Thesis Overview

This thesis is divided into two separate sections both related to the demonstration of new methods for light emission enhancement in photonic devices. The first section focuses on the use of cylindrical metal-insulator-metal devices for the enhancement of radiative emission rate relying on strong field confinement due to the formation of surface plasmons. The second section focuses on the use of photonic nanopillar arrays to increase light extraction from planar light emitting devices and to encode orbital angular momentum onto light.

In this chapter an overview of the motivation and context of the work was given. In

Chapter 2 a theoretical framework for light emission enhancement is given with a focus on enhanced radiative emission rate caused by increases in the photonic density of states (PDOS). A brief overview of the formation of surface plasmon polaritons and localized surface plasmons is given. In Chapter 3 an overview of the optical design methods used in this thesis are given with particular focus on a method derived and implemented for the calculation of PDOS in multilayered concentric cylinders. In Chapter 4 the optical properties of metal-insulator-metal structures are explored which provide strong field confinement and increased PDOS due to plasmon formation. In Chapter 5 plasmonic ring nanocavities, which operate on the same principles discussed in Chapter 4, are designed, fabricated and characterized displaying an increase in the PL intensity and spontaneous decay rate of Er ions by over 20 times. A perspective is given on how lasing with Er as an active medium could be achieved.

The second part of this thesis contains work related to the enhancement of extraction efficiency, control of radiation patterns and generation of OAM. Chapter 6 contains the optimization, fabrication and demonstration of aperiodic arrays of nanopillars for light extraction. In Chapter 7 a theoretical formulation for light propagation through arbitrary arrays of nanoparticles is derived and the ability of Vogel spiral arrays to encode OAM onto scattered light is demonstrated. In Chapter 8 an experimental technique for the measurement of OAM is introduced and used to show the generation of OAM from Vogel spirals. Finally in Chapter 9 conclusions are drawn from this work and future related work is discussed.

Chapter 2

Theory and Background

2.1 Introduction

In this chapter some general principles of light emission and its modification in photonic devices is discussed. First, spontaneous emission, absorption and stimulated emission are studied in an idealized two-level system with emphasis on how each process is affected by the density of photonic states. A more detailed quantum theory of light emission is presented to reinforce these conclusions. Next, the topic of light emission enhancement in photonic devices by modification of fundamental radiative processes is discussed. The Purcell enhancement factor for increased spontaneous emission rate is discussed along with its limitations for materials with emission bandwidth comparable to resonant cavity linewidth. A more rigorous calculation of enhanced spontaneous emission rate is shown and applied to Er light emission for resonant cavities with increasing Q factor. The results of this calculation show that confinement of light to small volumes is more important for realizing large emission rate enhancement than resonator Q factor. Finally, the formation of propagating and localized surface plasmon polaritons is discussed as a route for the subwavelength confinement of light.

2.2 Fundamentals of Light Emission

2.2.1 Idealized Two Level System

The fundamentals of light emission can be expressed most simply using an idealized two-level system where an electron can occupy one of two quantized energy levels. The electron can move from one state to the other through the absorption or emission of a photon who's energy equals that of the difference between the two allowable energy states. In Figure 2·1 (a) the process of spontaneous emission is depicted where an electron spontaneously (without the prior presence of a photon) moves from the upper energy state E_2 to the lower energy state E_1 through the emission of a photon with energy $\hbar\omega = E_2 - E_1$. The change in population of the two energy states, n_1 and n_2 can be expressed as

$$\frac{dn_1}{dt} = A_{21}n_2 \tag{2.1}$$

$$\frac{dn_2}{dt} = -A_{21}n_2 \tag{2.2}$$

where A_{21} is the Einstein A coefficient(Saleh and Teich, 2007; Einstein, 1916). The change in populations must be equal and of opposite sign so that electron number is conserved in the system. In Figure 2·1 (b) absorption is depicted where an electron moves from the lower to upper energy state by absorbing an incoming photon. In this case the change in population of the lower energy state is given by

$$\frac{dn_1}{dt} = -B_{12}n_1\rho(\omega) \tag{2.3}$$

where $\rho(\omega)$ is the spectral energy density. Finally, Figure 2·1 (c) depicts stimulated emission where a photon causes an electron to move from the upper to lower energy state producing a photon which is identical to the first. The change in population due

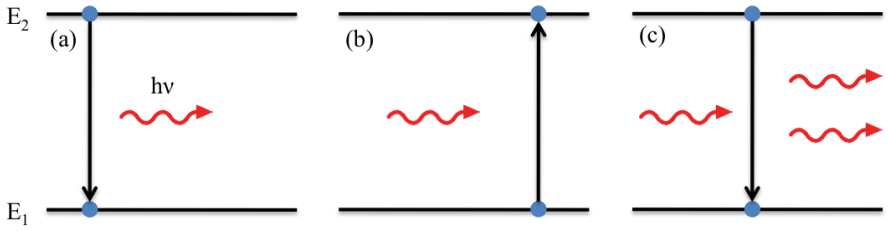

Figure 2·1: Light emission processes depicted in a two level system. (a,b,c) show spontaneous emission, absorption, and stimulated emission respectively. The states have energies E_1 and E_2 and the photons have energy $\hbar\omega = E_2 - E_1$.

to stimulated emission is given by

$$\frac{dn_1}{dt} = B_{21} n_1 \rho(\omega). \tag{2.4}$$

Since both absorption and stimulated emission depend on an incoming photon, the rate of change is dependent on the photon density of the incident radiation. Absorption and stimulated emission are often considered to be time reversed processes and for non-degenerate energy states $B_{12} = B_{21}$. Spontaneous emission on the other hand can be considered a stimulated emission process where the vacuum field energy provides the input causing photons to decay to the lower energy level.

We can see from the form of Equation 2.1 and 2.2 that the rate of photon emission from a population of electrons in state 2 will follow an exponential decay in time with the decay rate determined by the magnitude of A_{21}. We can then define A_{21} as,

$$A_{21} = \frac{1}{t_{sp}} \tag{2.5}$$

where t_{sp} is the spontaneous emission lifetime. Einstein showed that there is a fundamental relationship between the A and B coefficients which can be expressed as

$$\frac{A_{21}}{B_{21}} = \frac{\omega^3}{\pi^2 t_{sp}}, \tag{2.6}$$

allowing us to express B_{21} as

$$B_{21} = \frac{\lambda^3}{8\pi h t_{sp}}. \tag{2.7}$$

While the value of A_{21} can be calculated from the principles of quantum mechanics if the composition of the material is known it usually more practical to measure it experimentally(Saleh and Teich, 2007).

The energy states and photons in the idealized system are considered to have single well defined energy values. The fundamental uncertainty relationship between energy and time however prohibits this behavior in dynamical systems. The finite bandwidth of an energy level transition is described by the transition cross section, $\sigma(\omega)$, which determines the spectral lineshape of photon emission. Photons at different energies occupy different modes in free space and the likelihood of an energy level transition taking place (which determines t_{sp}) is dependent on the number of photon modes available over $\delta\omega$, the bandwidth of the transition. The density of photon modes in free space, $\rho_{fs}(\omega)$, is given by

$$\rho_{fs}(\nu) = \frac{2\omega^2}{\pi c^3} \tag{2.8}$$

Since $\rho_{fs}(\omega)$ varies slowly over $\sigma(\omega)$ for most materials we can express the, t_{sp} as

$$\frac{1}{t_{sp}} \propto \rho_{fs}(\omega_0)\delta\omega \tag{2.9}$$

where ω_0 is the center frequency of the transition cross section.

2.2.2 Quantum Theory of Electron Photon Interaction

Though an idealized two-level system can be used to describe fundamental light matter interactions, a more rigorous definition these processes must consider the quantum interaction of electrons and photons(Chuang, 2009). Consider an unperturbed system described by the hamiltonian, H_0, in the weak coupling regime. Incident light on the

system causes a perturbation allowing a new Hamiltonian to be written as,

$$H \approx H_0 - \frac{e}{2m_0}(\vec{A} \cdot \vec{p}) \tag{2.10}$$

where $\vec{A}$ is the vector potential, m_0 is the electron mass, e is the electron charge and $\vec{p}$ is the momentum operator. Equation 2.10 takes into account the Coulomb gauge, $\nabla \cdot \vec{A} = 0$, and $|e\vec{A}| \ll |\vec{p}|$, which allows the elimination of terms dependent on larger powers of $\vec{A}$. Choosing the incident optical field of a plane wave gives $\vec{A}$ the form,

$$\begin{aligned} \vec{A} &= \hat{e}A_0 cos(\vec{k} \cdot \vec{r} - \omega t) \\ &= \hat{e}\frac{A_0}{2}e^{i\vec{k}\cdot\vec{r}}e^{-i\omega t} + \hat{e}\frac{A_0}{2}e^{-i\vec{k}\cdot\vec{r}}e^{i\omega t} \end{aligned} \tag{2.11}$$

where $\vec{k}$ is the wavevector, ω is the optical frequency and $\hat{e}$ is the electric field unit vector. The interaction Hamiltonian, $H'(\vec{r},t)$ can now be written as $H'(\vec{r},t) = H'(\vec{r})e^{-i\omega t} + H'^{+}(\vec{r})e^{i\omega t}$ where

$$H'(\vec{r}) = -\frac{eA_0 e^{i\vec{k}\cdot\vec{r}}}{2m_0}\hat{e} \cdot \vec{p} \tag{2.12}$$

and $H'^{+}(\vec{r})$ is the Hermitian adjoint of $H'(\vec{r})$. Using this formalism the transition rate of electrons due absorption by an incident photon is given by,

$$W_{abs}(\omega) = \frac{2\pi}{\hbar}|\langle 2| H'(r) |1\rangle|^2 \delta(E_2 - E_1 - \hbar\omega) \tag{2.13}$$

where $|1\rangle$ and $|2\rangle$ are the initial and final energy states indicated in Figure 2·1. The rate of stimulated emission with an incident photon is given by

$$W_{emis}(\omega) = \frac{2\pi}{\hbar}|\langle 1| H'^{+}(r) |2\rangle|^2 \delta(E_1 - E_2 + \hbar\omega). \tag{2.14}$$

Equation 2.13 and Equation 2.14 assume that initially the electron is in state $|1\rangle$ and $|2\rangle$, respectively. Similarly, and consistently with the model presented in Section 2.2.1,

the rate of spontaneous emission is given by

$$W_{spon}(\omega) = \frac{2\pi}{\hbar}|\langle 1| H'^{+}(r) |2\rangle|^2 \delta(E_1 - E_2 + \hbar\omega)\rho(\omega) \tag{2.15}$$

where $\rho(\omega)$ is the photonic density of states. Scattering relaxation can be taken into account by replacing the delta function with a Lorentzian of the form,

$$L(E_b - E_a - \hbar\omega) = \frac{\gamma/\pi}{(E_b - E_a - \hbar\omega)^2 + \gamma^2} \tag{2.16}$$

where the area under the curve has been normalized to one. This will give a linewidth of 2γ to the spontaneous emission, absorption and stimulated emission spectrums.

2.2.3 Purcell Enhancement

It was once thought that the spontaneous decay rate was a fundamental material property however as suggest by Purcell(Purcell, 1946) it is now known that the decay rate can be altered by the surrounding environment. By changing the density of photonic states the rate of spontaneous emission can be either suppressed or enhanced. One example of an optical device which alters the density of states is a photonic crystals in which strong fluctuations of refractive index on a length scale similar to the optical wavelength can cause the formation of photonic bandgaps where the density of states is strongly suppressed. A second example is an optical cavity where the trapping of light at resonant frequencies can increase the photonic density of states. The increase in the photonic density of states in a resonant cavity is given by the so called Purcell factor,

$$F_p = \frac{3}{4\pi^2}(\frac{\lambda_c}{n})^3(\frac{Q}{V}) \tag{2.17}$$

where Q is the resonator quality factor and V is the resonator volume. Purcell enhancement has been shown to strongly modify the spontaneous emission rate in resonant cavities of many different geometries over the past several decades (Vredenberg et al.,

1993; Kroekenstoel et al., 2009; Noginov et al., 2006; Russell et al., 2012). We can see however, from the relationship between spontaneous emission, stimulated emission and absorption outlined in this section that increased spontaneous emission rate will also increase the optical absorption rate and the rate of stimulated emission. Much of the work in thesis focuses on the design of Purcell enhancement in photonic and plasmonic devices as well as the ability to exploit enhanced stimulated emission to make Si-based lasers.

2.3 Light Emission Enhancement

With the basic details surrounding the modification of radiative processes laid out in the previous section it is time to address how these effects can be used to enhance light emission. Though there are many forms of luminescence the focus of this discussion will be on photoluminescence (PL), where light is emitted after the absorption of a photon. The rate of PL photon flux, ϕ_{PL}, is given by

$$\phi_{PL} = \phi_{pump}\eta_{abs}\eta_{IQE}\eta_{ext} \tag{2.18}$$

where ϕ_{pump} is the rate of pump photon flux, η_{abs} is the absorption efficiency, η_{IQE} is the internal quantum efficiency and η_{ext} is the extraction efficiency(Novotny and Hecht, 2006). The photoluminescence process involves the absorption of a pump photon, decay of excited electron through production of PL photon and extraction of that photon. Each part of the process has an associated efficiency, η_{abs}, η_{IQE} and η_{ext}, respectively. The modification of the density of states in photonic and plasmonic devices can affect all three of these processes.

The first way to enhance light emission is through an increase in the absorption efficiency, η_{abs}. In Equation 2.3 the rate of light absorption was shown to be proportional to the B_{12} coefficient. The magnitude of the B_{12} coefficient is dependent on the

spontaneous emission lifetime and hence the PDOS. By increasing the PDOS (and also local electric field) light absorption rate can be significantly increased. Since the rate of absorption varies with incoming number of photons it is more common to express absorption in terms of the propagation length (instead of time) needed for absorption which will be decreased by an increase in the B_{12} coefficient. In a finite sized device a shorter absorption length will lead to a larger absorption efficiency though the amount of increase depends on the starting absorption efficiency.

The second way to enhance light emission is by changing the internal quantum efficiency, η_{IQE}, given by

$$\eta_{IQE} = \frac{\Gamma_r}{\Gamma_r + \Gamma_{nr}} \tag{2.19}$$

where Γ_r is the radiative emission rate, the rate at which electrons loose energy by the production of photons, and Γ_{nr} is the non-radiative emission rate. When the population of the lower energy state exceeds that of the upper, or at low photon flux, the main contribution to Γ_r will be from spontaneous emission. If the spontaneous emission rate increases so will Γ_r leading to an increase in η_{IQE}. In devices with optical gain and large photon flux, such as lasers, stimulated emission can significantly increase Γ_r as well. This increase in η_{IQE} due to stimulated emission is what gives lasers such high efficiencies. As with changes in η_{abs} the total possible increase in η_{IQE} depends strongly on the starting value, materials with low η_{IQE} experience stronger enhancements with increased photonic density of states(Novotny and Hecht, 2006).

The final factor which leads to light emission enhancement is the extraction efficiency, η_{ext}. Here the effect of an increased photonic density of states in not as obvious. One detrimental factor to η_{ext} is reabsorption of photons which would be increased as discussed previously. However, many photonic devices are designed to redirect light out with minimal propagation length in the device, leading to lower total absorption. Since this is a complex topic which depends strongly on device design and application it will

not be discussed here but covered in detail in the second part of this thesis.

2.3.1 Saturation of Purcell Effect

In the derivation of Equation 2.17 the density of states is considered to be constant, limiting its applicability cases where the spontaneous emission bandwidth is smaller than the resonant cavity bandwidth(Purcell, 1946). This distinction is important as using Equation 2.17 to calculate spontaneous emission rate enhancement in high Q cavities will lead to a large overestimation. To calculate the enhancement of spontaneous emission rate accounting for finite emission bandwidth a more rigorous definition of the spontaneous emission rate, R_{sp}, must be used, given by,

$$R_{sp} = \int\int A_{21}\rho_{el}(E)\rho_{op}(\hbar\omega)L(E-\hbar\omega)d\hbar\omega dE \tag{2.20}$$

where $\rho_{el}(E)$ is the electronic density of states $\rho_{op}(\hbar\omega)$ is the photonic density of states (PDOS) and $L(E-\hbar\omega)$ is the lineshape function due to homogeneous broadening of the emitter linewidth. Equation 2.20 takes into account both a non-uniform $\rho_{op}(\hbar\omega)$ and finite spontaneous emission bandwidth through the product $\rho_{el}(E)L(E-\hbar\omega)$. When $\rho_{op}(\hbar\omega)$ does not strongly depend on frequency (i.e., free space) the spontaneous emission lineshape is proportional to $\rho_{el}(E) \times L(E-\hbar\omega)$. In the limit of $\rho_{el}(E) \times L(E-\hbar\omega) \rightarrow \delta(E-\hbar\omega_c)$, where $\hbar\omega_c$ is the resonance frequency of the cavity, Equation 2.20 will be proportional to $\rho_{op}(\hbar\omega)$ at the cavity central frequency, equivalent to its definition in Equation 2.17. By comparing Equation 2.20 in a resonant cavity with that of free space a more rigorous spontaneous emission enhancement can be calculated.

To calculate spontaneous emission rate the resonant cavity PDOS, $\rho_{cav}(\omega)$, must be used, which is given by

$$\rho_{cav}(\omega) = \frac{N_c(\omega)}{V} = \frac{\delta\omega}{2\pi V}\frac{1}{(\omega-\omega_0)^2 + (\frac{\delta\omega}{2})^2} \tag{2.21}$$

where $\delta\omega$ is the linewidth of the cavity. Though the PDOS in the cavity increases at the resonance frequency, the PDOS integrated over frequency ($-\infty$ to ∞) is independent of Q (and $\delta\omega$). New photon states are not created by a resonant cavity they are just redistributed in frequency. This means that as the Q factor of a resonator increases and $\delta\omega$ becomes more narrow than the spontaneous emission bandwidth in the cavity there will be a saturation in the enhancement with further increase of Q. Using Equation 2.20 the spontaneous emission enhancement factor for cavities of different volume and Q factor is calculated considering Er as the active material, the results are shown in Figure 2·2. The blue, red and green solid line show the increased spontaneous emission rate (according to Equation 2.20) in cavities with increasing Q factor and volumes of $0.01(\frac{\lambda}{n})^3$, $0.1(\frac{\lambda}{n})^3$ and $1(\frac{\lambda}{n})^3$ respectively while the dotted lines show the calculation of F_p using Equation 2.17. The vertical dotted black line is the Q factor corresponding to the FWHM of Er light emission. This shows that as the lineshape of the resonator becomes more narrow than the light emission bandwidth of the material in the cavity the increase of spontaneous emission rate saturates. Thus, large spontaneous emission enhancement cannot be achieved by large Q factor alone, shrinking the cavity volume is crucial.

2.4 Light Localization by Surface Plasmons

In Section 2.3 factors for light emission enhancement are discussed which largely rely on the confinement of light. In particular, high spontaneous emission enhancement factors for materials with homogeneously broadened light emission can only be achieved in small volume cavities due to the saturation of Purcell enhancement. One challenge in confining light to small volumes is that its wave nature typically precludes it from occupying volumes smaller than λ^3. One way to confine light beyond the diffraction limit is through the excitation of surface plasmons.

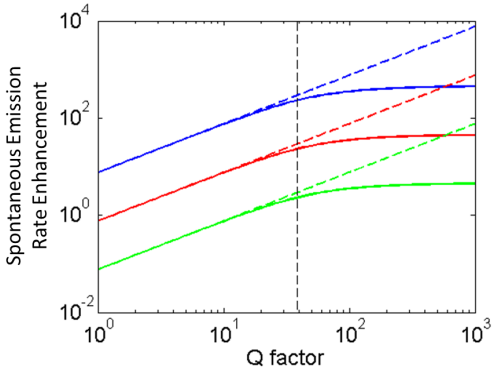

Figure 2·2: Enhancement of spontaneous emission rate calculated for Er emission using the spontaneous emission rate given by Equation 2.20 (solid lines) as a function of cavity Q factor. Three cavity Volumes are considered with normalized volumes of $0.01(\frac{\lambda}{n})^3$ (blue), $0.1(\frac{\lambda}{n})^3$ (red) and $1(\frac{\lambda}{n})^3$ (green). The vertical dotted black line shows the FWHM of Er spontaneous emission. When the cavity Q factor surpasses FWHM of Er spontaneous emission the rate enhancement saturates. The colored dotted lines show the Purcell factor calculated according to Equation 2.17 which ignores the homogeneous linewidth broadening.

2.4.1 Surface Plasmon Polaritons

A plasmon is the quantum of oscillation of the free electron charge density which takes place at the plasma energy. Using the free electron model the plasma energy, E_p, is given by,(Kittel, 1996)

$$E_p = \hbar\sqrt{\frac{ne^2}{m\epsilon_0}}. \tag{2.22}$$

In noble metals the bulk plasma frequency, $\nu_p = \frac{E_p}{h}$, is in the visible spectrum(Novotny and Hecht, 2006). Excitation of a bulk plasmon can be understood as a collective longitudinal oscillation of the conduction electron density relative to the fixed changes of the atomic nuclei. The displacement of electrons establishes an electric field inside the metal as charge density accumulates on the surface. The electric field from this charge build up in turn provides a restoring force for the conduction electrons. The plasma frequency is the natural frequency of this oscillation(Maier, 2007).

At the interface of a metal and dielectric material, it is possible for a photon to

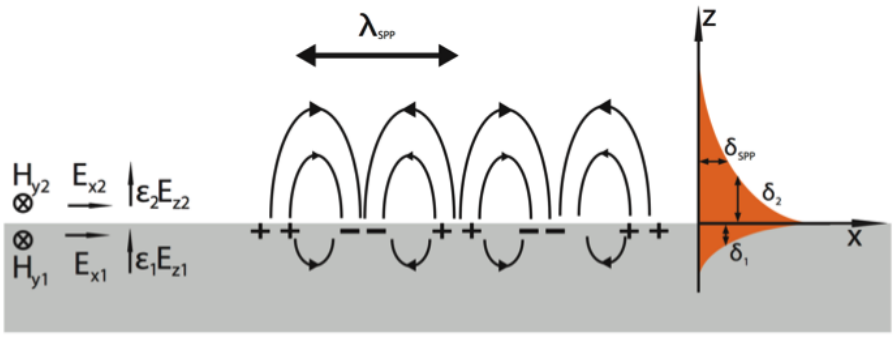

Figure 2·3: Schematic of a surface plasmon polariton at the interface of a metal and a dielectric.

couple to a plasmon and form a surface plasmon polariton (SPP). The electric field fluctuations provided by the plasmon causes confinement of the optical field to lengths significantly smaller than the wavelength, which strongly increases the local electric field. A schematic of a SPP is shown in Figure 2·3 with propagation along the metal surface.

The electric field of a time harmonic electromagnetic wave in 2-dimensions is given by,

$$E(x,z) = E_0 e^{i(k_x x + k_z z)} \tag{2.23}$$

with the wave propagating in the X-direction. A surface wave exists at the boundary of two materials with E field decaying exponentially in the Z-direction (as depicted in Figure 2·3) with propagation constant $\beta = k_x$ given by(Novotny and Hecht, 2006)

$$\beta = \frac{\omega}{c}\left(\frac{\epsilon_1 \epsilon_2}{\epsilon_1 + \epsilon_2}\right)^{1/2}. \tag{2.24}$$

β is a complex number where the SPP propagation length, L, is given by $L = \frac{1}{2Im[\beta]}$. The field profile in the vertical direction decays exponentially as $e^{-|k_z||z|}$ where $k_z = \sqrt{k_0^2 - \beta^2}$. The formation of an SPP is only possible in TM polarization and when the electric permittivities of the materials are of opposite sign and satisfy $\epsilon_1 + \epsilon_2 < 0$(Shalaev and Kawata, 2006; Maier, 2007).

2.4.2 Localized Surface Plasmons

Additionally to propagating SPPs, localized SPPs (LSPs) can be excited on metal nanoparticles. In this case the free electrons of the metal nanoparticle couple with the photon, similar to SPPs. Due to the confinement of free electrons to the particle, the dispersion of LSPs depends on the size and geometry of the metal nanoparticle. The curved surfaces of the nanoparticle provide a restoring force for the oscillating electrons and a resonance can occur, called the plasmon resonance. When the particle is excited by photons near the plasmonic resonance energy, its electromagnetic response increases dramatically(Novotny and Hecht, 2006; Maier, 2007). The excitation of LSPs can cause confinement of light to smaller volumes than propagating SPPs, due to plasmon formation in 3-dimensions. The decay length of the electric field into the dielectric region will still limit the overall electric field confinement.

For a spherical metallic particle in the quasi-static limit, $d \ll \lambda$, where d is the particle diameter, the dipole moment, $\vec{p}$, is given by(Maier, 2007)

$$\vec{p} = 4\pi\epsilon_0\epsilon_m a^3 \frac{\epsilon - \epsilon_m}{\epsilon + 2\epsilon_m}\vec{E}_0 \tag{2.25}$$

where a is the particle radius, ϵ is the permittivity of the imbedding medium, and ϵ_m is the permittivity of the metallic particle. A schematic of the particle is shown in Figure 2·4 (a). By defining the polarizability as, $\vec{p} = \epsilon_0\epsilon_m\alpha\vec{E}_0$, we find that the polarizability of a sphere is given by,

$$\alpha = 4\pi a^3 \frac{\epsilon - \epsilon_m}{\epsilon + 2\epsilon_m}. \tag{2.26}$$

Interestingly, we can see that, α, will have a maximum when $|\epsilon + 2\epsilon_m|$ is minimized. In this condition the dipolar surface plasmon mode of the particle is excited. The magnitude of the polarizability of Ag and Au nanoparticles with 50nm diameter is

shown in Figure 2·4 (b) which is calculated using experimentally measured material data(Johnson and Christy, 1972). For the Ag nanoparticle, shown in blue, there is a strong resonant increase in α around 350nm and for the Au nanoparticle, shown in red, there is a significantly weaker resonant response around 520nm. The resonance of both particles happens when $Real(\epsilon_m) = -\epsilon/2$, however $Imag(\epsilon_m)$ limits the increase in polarizability. The resonant effect of the Ag particle is much stronger due to the weaker absorption in Ag. The electromagnetic field profile of a Au nanoparticle, excited at the dipolar resonance, is shown in Figure 2·4 (c). Strong field confinement is observed at the surface of the particle quickly decaying into the dielectric medium(Noginov et al., 2009). The large polarizability of the particle at the plasmonic resonance will increase the scattering and absorption cross sections, C_{sca} and C_{abs}, respectively. Generally, the scattering (absorption) cross seciton is given by the scattered (absorbed) power, normalized by the incident intensity, $C_{sca} = \frac{W_{sca}}{I_i}$. In the quasi-static limit, C_{sca} and C_{abs} can be approximated as(Bohren and Huffman, 1998),

$$C_{sca} = \frac{k^4}{6\pi}|\alpha|^2 = \frac{8\pi}{3}k^4a^6|\frac{\epsilon - \epsilon_m}{\epsilon + 2\epsilon_m}|^2 \tag{2.27}$$

$$C_{abs} = kIm[\alpha] = 4\pi ka^3 Im[\frac{\epsilon - \epsilon_m}{\epsilon + 2\epsilon_m}] \tag{2.28}$$

for particles with $a \ll \lambda$. Interestingly, C_{abs} scales with a^3 while C_{sca} scales with a^6. Due to this behavior the absorption of very small particles tends to dominate the scattering.

2.5 Conclusions

In conclusion, this chapter outlines many of the theoretical concepts which will be used later in this thesis. First, light emission and absorption processes are discussed in an idealized 2-level system and the relation of each process to the PDOS is described. A quantum theory of light emission is also presented to reinforce these conclusions. Next,

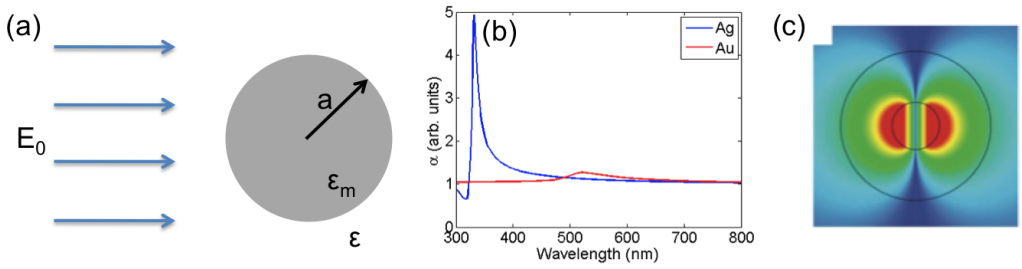

Figure 2·4: (a) Schematic of a metallic nanoparticle excited by a planewave. (b) Polarizability of Au (red) and Ag (blue) nanoparticles (50nm diameter) calculated using Equation 2.26 (c) Local electric field on a 14nm diameter Au nanoparticle excited at the plasmonic resonance. (Noginov et al., 2009)

the modification of the PDOS in resonant cavities (ie Purcell enhancement) is discussed along with limitations of the Purcell formula when spontaneous emission bandwidth is larger than the resonant cavity linewidth. A more rigorous definition of enhanced spontaneous emission rate is shown and calculations of enhanced rate are provided for resonant cavities of increasing Q factor considering Er as an active medium. It is found that high spontaneous emission enhancement cannot be achieved by large Q factor alone and shrinking the cavity volume is crucial. Finally, the formation of surface plasmon polaritons is discussed as a way of confining light past the diffraction limit.

Chapter 3

Computational Methods

3.1 Introduction

In this chapter the computational methods used in this thesis for the calculation of scattering, near-field enhancement and PDOS in plasmonic structures are explained. First, a detailed derivation of the electromagnetic response of a 2D system of multilayered, concentric cylinders is presented. This method is based on a Mie theory type approach where the electric and magnetic fields are expressed in a set of circular basis functions which allow for the matching of boundary conditions at layer interfaces and calculation of electromagnetic fields to an arbitrary degree of accuracy. Using this method, the response of a multilayered cylinder to plane wave excitation is calculated providing the scattering properties and the local electromagnetic fields within the device. Next, the response of the multilayered cylinder to a point source excitation is derived which is used to calculate the local density of photonic states. Though this method is accurate and efficient the geometry which can be simulated is limited, to investigate other systems and calculate the response of 3-dimensional devices the finite difference time domain (FDTD) method is used. A brief summary of the FDTD method is presented here along with a discussion of its pros and cons as a method for simulating photonic devices.

3.2 Analytic Calculation of Optical Properties in Concentric Multilayered Cylinders

In general the propagation of electromagnetic waves through an arbitrarily shaped particle cannot be solved analytically. However, for certain systems, having a high degree of symmetry, closed form solutions do exist. One example was discovered nearly a century ago by Gustav Mie (Mie, 1908) who solved for the wave propagation inside a sphere of arbitrary size and electric permittivity. Similar solutions have been derived for infinite cylinders that take advantage of their circular symmetry(Bohren and Huffman, 1998). Due to the separability of time and space in the wave equations, spatial solutions for wave propagation must satisfy the Helmholtz equation,(Novotny and Hecht, 2006; Saleh and Teich, 2007)

$$\nabla^2 A(\vec{r}) + k^2 A = 0. \tag{3.1}$$

In 2-dimensions the solution to Equation 3.1 can be expressed as a linear combination of Bessel functions in the radial variable and complex exponential functions in the azimuthal variable,(Bohren and Huffman, 1998)

$$A(\vec{r}) = \sum_{n=-\inf}^{\inf} [A_n J_n(kr) + B_n H_n(kr)] e^{-in\phi} \tag{3.2}$$

where $J_n(kr)$ is the Bessel function of the first kind and $H_n(kr)$ is the Hankel function of the first kind. By expressing the electromagnetic field using Equation 3.2 the scattering from an cylinder of arbitrary electric permittivity can be calculated. The origin of the coordinate system is chosen to be at the center of the cylinder and the field on the inside and outside of the cylinder are related by the boundary conditions at the interface. For the boundary conditions to be satisfied at the surface of the cylinder the tangential component of the electric field and the normal component of the electric displacement must be constant across the boundary. The orthogonality of the terms

in Equation 3.2 allows for the boundary conditions to be satisfied independently for each summation order. By solving the system of equations formed by the boundary conditions the coefficients A_n and B_n are found and the field can be reconstructed using Equation 3.2(Bohren and Huffman, 1998).

This same formulation can be extended to solve for the electromagnetic response of a concentric multilayered cylinder(Lawrence and Dal Negro, 2010). In this case the out of plane (Z-direction) field component in the l_{th} layer, $U^l(r,\phi)$, is given by

$$U^l(r,\phi) = \sum_{n=-\inf}^{\inf} [A_n^l J_n(k_l r) + B_n^l H_n(k_l r)] e^{-in\phi}. \tag{3.3}$$

A schematic of the problem is shown in Figure 3·1 where a multilayered concentric cylinder with m layers is constructed, centered at the origin. The thickness of the layers is specified by $(r_1, r_2, ..., r_m)$ and the electric permittivity is specified by $(\epsilon_1, \epsilon_2, ..., \epsilon_m, \epsilon_{m+1})$, where ϵ_{m+1} is the permittivity of the surrounding medium. Within each layer the field is determined by the A_n^l and B_n^l terms where the J_n terms give the contribution of waves propagating towards $r = 0$ and H_n terms give the contribution of waves propagating towards $r \to \infty$. Due to the divergence of $H_n(0)$ and oscillatory behavior of $J_n(r \to \infty)$ the coefficients A^{m+1} and B^0 are set to 0. Using this formulation of the problem the homogeneous Helmholtz equation can be solved to find eigenfunctions of the system or the inhomogeneous Helmholtz equation can be solved to find the response of the system to an arbitrary source(Boriskin and Nosich, 2002; Lawrence and Dal Negro, 2010).

3.2.1 Plane Wave Excitation

In this section the solutions for a planewave excitation will be presented. To add a source to the problem Equation 3.3 must be modified as(Lawrence and Dal Negro, 2010)

$$U^l(r,\phi) = U_s^l(r,\phi) + \sum_{n=-\infty}^{\infty} [A_n^l J_n(k_l r) + B_n^l H_n(k_l r)] e^{-in\phi}. \tag{3.4}$$

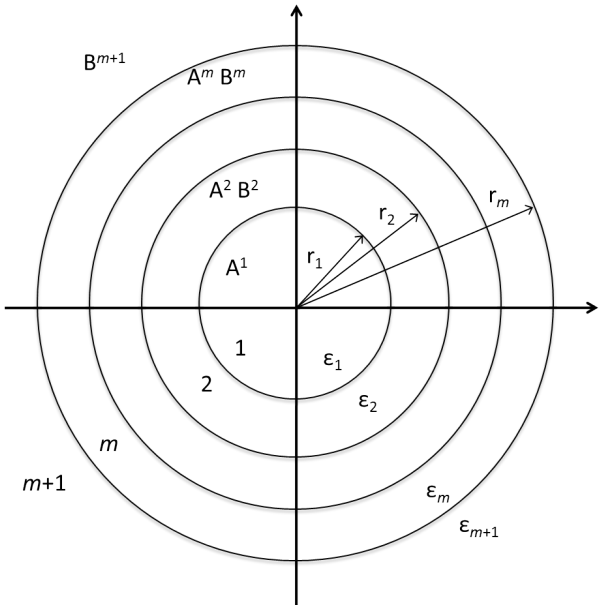

Figure 3·1: The geometry of a multilayered cylinder of m layers each having outer radius r_m, forming m+1 zones each specified by a complex permittivity ϵ_m. The three coefficients in each zone, A, B and C will give the value of the fields in that zone. The $\vec{r}_s$ indicates the location of the source for point source excitation.

where $U_s^l(r,\phi)$ is the source contribution to the field in the l_{th} layer. The contribution of the source is only explicitly added in the layer containing the source, in all other layers the source contribution is included in the transmitted field components. It is necessary to express the source as a sum of Bessel functions so that the boundary conditions can be matched for each Bessel order. Using the Jacobi-Anger expansion, a plane wave traveling in the X-direction can be expressed as,(Bohren and Huffman, 1998)

$$e^{ikx} = e^{ikr\cos\phi} = \sum_{n=-\infty}^{\infty} i^n J_n(kr) e^{in\phi}. \tag{3.5}$$

By combining this with Equation 3.4 we arrive at a new expression for the field,

$$U_s^l(r,\phi) = \sum_{n=-\infty}^{\infty} [A_n^l J_n(k_l r) + B_n^l H_n^{(1)}(k_l r) + C_n^l J_n(k_l r)] e^{-in\phi} \tag{3.6}$$

where(Bohren and Huffman, 1998)

$$C_n^{m+1} = i^n. \tag{3.7}$$

With the problem of excitation by a plane-wave explicitly stated a solution can be found by solving the matrix equation formed from the boundary conditions. Using Equation 3.6 the Z-component of the field is calculated which corresponds to either the electric (TE) or magnetic (TM) field depending on the input. Using the time harmonic formulation of Maxwell's equations(Saleh and Teich, 2007; Novotny and Hecht, 2006)

$$\nabla \times H = i\omega\epsilon E \tag{3.8}$$

$$\nabla \times E = -i\omega\mu H \tag{3.9}$$

the other field components can be calculated. The calculation of the curl can be done numerically or more accurate solutions can be found which analytically relate the other field components to the A_n^l, B_n^l and C_n^l coefficients. When the incident light is polarized orthogonal to the axis of the cylinder (TM) the non-zero field components are,

$$H_z = \sum_{n=-\infty}^{\infty} [A_n J_n(k_l r) + B_n H_n(k_l r)] e^{-in\phi} \tag{3.10}$$

$$E_r = \sum_{n=-\infty}^{\infty} \frac{n}{\epsilon\omega r} [A_n J_n(k_l r) + B_n H_n(k_l r)] e^{-in\phi} \tag{3.11}$$

$$E_\phi = \sum_{n=-\infty}^{\infty} \frac{1}{i\epsilon\omega} [A_n \frac{\delta J_n(k_l r)}{\delta r} + B_n \frac{\delta H_n(k_l r)}{\delta r}] e^{-in\phi} \tag{3.12}$$

and when the incident light is polarized along the axis of the cylinder the non-zero field components are given by

$$E_z = \sum_{n=-\infty}^{\infty} [A_n J_n(k_l r) + B_n H_n(k_l r)] e^{-in\phi} \tag{3.13}$$

$$H_r = \sum_{n=-\infty}^{\infty} \frac{-n}{\omega r}[A_n J_n(k_l r) + B_n H_n(k_l r)]e^{-in\phi} \tag{3.14}$$

$$H_\phi = \sum_{n=-\infty}^{\infty} \frac{-1}{i\omega}[A_n \frac{\delta J_n(k_l r)}{\delta r} + B_n \frac{\delta H_n(k_l r)}{\delta r}]e^{-in\phi}. \tag{3.15}$$

Additionally to the electric field we would like to find the scattering efficiency for multilayered cylinders which is calculated by finding the power of the field that is scattered away from the structure. The power in the far-field, W, is given by integrating the Poynting vector flux through a cylindrical surface around the structure,(Bohren and Huffman, 1998)

$$W = RL \int_0^{2\pi} (S)_r d\phi \tag{3.16}$$

where R is the radius of the cylindrical surface, L is the length and $(S)_r$ is the radial component of the Poynting vector in the outer region problem (m+1 layer). The Poynting vector is given by $S = E \times H^*$ which will require all of the field components for calculation. When the expressions for each field component are substituted in for E and H, the following expression is found

$$(S)_r = \sum_{n=-\infty}^{\infty} \frac{1}{i\epsilon\omega} H_n^*(k_l r) \frac{\delta H_n(k_l r)}{\delta r} |B_n^l|^2 \tag{3.17}$$

for the case of non-zero H_z and

$$(S)_r = \sum_{n=-\infty}^{\infty} \frac{1}{i\omega} H_n(k_l r) \frac{\delta H_n^*(k_l r)}{\delta r} |B_n^l|^2 \tag{3.18}$$

for the case of non-zero E_z. The integration in Equation 3.16 is now trivial as the expression does not depend on ϕ and the scattering efficiency can be expressed as(Bohren and Huffman, 1998)

$$Q_{scat} = \frac{\lambda}{\pi r_M} \sum_{n=-\infty}^{\infty} |B_n^{M+1}|^2. \tag{3.19}$$

A similar technique is used to calculate the extinction efficiency, Q_{ext}, expressed as,

$$Q_{ext} = \frac{\lambda}{\pi r_M} Re(B_0^{M+1} + 2\sum_{n=1}^{\inf} B_n^{M+1}). \tag{3.20}$$

With the solution to planewave excitation laid out, the excitation by a point source can now be considered.

3.2.2 Point Source Excitation

In this section solutions to a point source excitation are given which will allow for the calculation of the PDOS. The PDOS, $\rho(r_s;\omega)$, can be obtained according to(Novotny and Hecht, 2006),

$$\rho(r;\omega) = -\frac{2\omega n^2}{\pi c^2} Im[Tr[G(r,r;\omega)]]. \tag{3.21}$$

where n is the refractive index and $G(r,r_s;\omega)$, the Green's Tensor, is the system impulse response to a point source located at located at r_s. To find the three diagonal components of the Green's tensor we will have to solve the problem for the three different source orientations, considering a source with dipole moment oriented along the x, y and z axis of the Cartesian coordinate system. Averaging over orientation gives the response of randomly oriented emitters. By calculating the Green's tensor at the location of the source we find how field generated by a source is reflected and acts on itself.

Similarly to the procedure used to solve for the response to a planewave, in order to take advantage of the cylindrical symmetry of the problem, we need to express the source term as an expansion of Bessel and Hankel functions centered at the origin of our reference system (see Figure 3·1). As a result, we obtain the following representation for the fields everywhere in the structure:

$$U_s^l(r,\phi) = \sum_{n=-\infty}^{\infty} [A_n^l J_n(k_l r) + B_n^l H_n(k_l r) + C_n^l X_n(k_l r)] e^{-in\phi} \tag{3.22}$$

where,

$$X_n(k_l r) = \begin{cases} J_n(k_l r), & r < r_s \\ H_n(k_l r) & r > r_s \end{cases} \tag{3.23}$$

and C_n^l are the expansion coefficients of a source with an arbitrary field profile. The function X_n^l is a Bessel function in regions including the origin and becomes a Hankel function in unbounded regions in order to correctly handle singularities and to allow for power conservation in the system. The z-component of the field (electric or magnetic, depending on the dipole orientation) for an electric dipole can be expressed as:(Asatryan et al., 2007; Lawrence and Dal Negro, 2010)

$$U_{s,z} = H_0(k|\vec{r} - \vec{r}_s|)/(4i) \tag{3.24}$$

$$U_{s,x} = -H_1(k|\vec{r} - \vec{r}_s|)sin(\phi)/(4) \tag{3.25}$$

$$U_{s,z} = H_1(k|\vec{r} - \vec{r}_s|)cos(\phi)/(4) \tag{3.26}$$

where $U_{s,a}(a = x, y, z)$ is for an a-oriented dipole and $\phi = arg(\vec{r} - \vec{r}_s)$. To use these source profiles in Equation 3.22 the functions must be expanded in a sum of Bessel and Hankel functions centered at the origin. This can be done using Graf's addition theorem

$$H_m(k|\vec{r} - \vec{r}_s|) = \begin{cases} \sum_{n=-\infty}^{\infty} J_n(kr)H_{n-m}(kr_s)e^{in\phi - i(n-m)\phi_s}, & \text{if } r < r_s \\ \sum_{n=-\infty}^{\infty} H_n(kr)J_{n-m}(kr_s)e^{in\phi - i(n-m)\phi_s}, & \text{if } r > r_s \end{cases} \tag{3.27}$$

which expresses a Bessel/Hankel function centered in one location as a sum of weighted Bessel/Hankel functions centered at a different location. The source coefficients for a dipole are(Lawrence and Dal Negro, 2010)

$$C_n^s = \begin{cases} \frac{-1}{8i}[H_{n-1}(k_s r_s)e^{-i(n-1)\phi_s} + H_{n+1}(k_s r_s)e^{-i(n+1)\phi_s}], & \text{if } r < r_s \\ \frac{-1}{8i}[J_{n-1}(k_s r_s)e^{-i(n-1)\phi_s} + J_{n+1}(k_s r_s)e^{-i(n+1)\phi_s}], & \text{if } r > r_s \end{cases} \tag{3.28}$$

for an x-oriented source,

$$C_n^s = \begin{cases} \frac{1}{8}[H_{n-1}(k_s r_s)e^{-i(n-1)\phi_s} - H_{n+1}(k_s r_s)e^{-i(n+1)\phi_s}], & \text{if } r < r_s \\ \frac{1}{8}[J_{n-1}(k_s r_s)e^{-i(n-1)\phi_s} - J_{n+1}(k_s r_s)e^{-i(n+1)\phi_s}], & \text{if } r > r_s \end{cases} \tag{3.29}$$

for a y-oriented source and,

$$C_n^s = \begin{cases} \frac{1}{4i} H_n(k_s r_s) e^{-in\phi_s}, & \text{if } r < r_s \\ \frac{1}{4i} J_n(k_s r_s) e^{-in\phi_s}, & \text{if } r > r_s \end{cases} \tag{3.30}$$

for a z-oriented source. The C_n^s coefficients are zero outside of the layer containing the source. With the source properly defined for each orientation the problem can now be solved and calculation of the field at the location of the source will give the PDOS, according to Equation 3.21. Since the matrix equation which will be formed for each problem separates the source from the rest of the structure, computation time can be decreased by doing a single matrix inversion and multiplying the inverted matrix by many different source vectors, giving the PDOS at many locations. In addition to the PDOS it is interesting to find the power that is radiated to the far-field as opposed to being absorbed inside a device. Using the formulation in the derivation of scattering cross section in Section 3.2.1, radiated power from a dipole source can also be calculated.

3.2.3 Notes on Implementation

The matrix equation for a three-layered structure is shown below, where each set of two rows are the two field continuity equations that exist at each boundary, starting from the innermost boundary. The zeros arise for coefficients associated with fields that are not present at that boundary.

$$\begin{bmatrix} J_n(k_1r_1) & -J_n(k_2r_1) & -H_n^{(1)}(k_2r_1) & 0 & 0 & 0 \\ \frac{1}{\epsilon_1}J_n'(k_1r_1) & -\frac{1}{\epsilon_2}J_n'(k_2r_1) & -\frac{1}{\epsilon_2}H_n'^{(1)}(k_2r_1) & 0 & 0 & 0 \\ 0 & J_n(k_2r_2) & H_n^{(1)}(k_2r_2) & -J_n(k_3r_2) & -H_n^{(1)}(k_3r_2) & 0 \\ 0 & \frac{1}{\epsilon_2}J_n'(k_2r_2) & \frac{1}{\epsilon_2}H_n'^{(1)}(k_2r_2) & -\frac{1}{\epsilon_3}J_n'(k_3r_2) & -\frac{1}{\epsilon_3}H_n'^{(1)}(k_3r_2) & 0 \\ 0 & 0 & 0 & J_n(k_3r_3) & H_n^{(1)}(k_3r_3) & -H_n^{(1)}(k_4r_3) \\ 0 & 0 & 0 & \frac{1}{\epsilon_3}J_n'(k_3r_3) & \frac{1}{\epsilon_3}J_n'(k_3r_3) & -\frac{1}{\epsilon_4}H_n'^{(1)}(k_4r_3) \end{bmatrix}$$

$$\begin{bmatrix} A_n^1 \\ A_n^2 \\ B_n^2 \\ A_n^3 \\ B_n^3 \\ B_n^4 \end{bmatrix} = \begin{bmatrix} C_n^2 X_n(k_2r_1) - C_n^1 X_n(k_1r_1) \\ C_n^2 \frac{1}{\epsilon_2} X_n'(k_2r_1) - C_n^1 \frac{1}{\epsilon_1} X_n'(k_1r_1) \\ C_n^3 X_n(k_3r_2) - C_n^2 X_n(k_2r_2) \\ C_n^3 \frac{1}{\epsilon_3} X_n'(k_3r_2) - C_n^2 \frac{1}{\epsilon_2} X_n'(k_2r_2) \\ C_n^4 X_n(k_4r_3) - C_n^3 X_n(k_3r_3) \\ C_n^4 \frac{1}{\epsilon_4} X_n'(k_4r_3) - C_n^3 \frac{1}{\epsilon_3} X_n'(k_3r_3) \end{bmatrix} \tag{3.31}$$

The A_n^{m+1} coefficients (outermost layer) and B_n^1 coefficients (innermost layer) have been set to zero and do not appear in the matrix equation for reasons detailed in (Bohren and Huffman, 1998; Boriskin and Nosich, 2002). The contribution of the source has been moved to the right hand side of the equation so the matrix is only dependent on the geometry, materials and wavelength of the problem, but not on the source location or its field profile. As mentioned above, the C_n^l coefficients are non-zero only in the source layer; therefore most of the terms on the right hand side will vanish once the position of the source is determined. Since the source field profile is not yet specified, this matrix equation can be used to calculate the system's response to a plane wave or to localized point sources.

3.3 Finite Difference Time Domain Method

While the analytic methods typically have high accuracy and take a relatively small amount of computational power they are only applicable to specific problems. Though they are typically slower and can be less accurate, the use of numerical methods allows for the investigation of light propagation in arbitrary geometries. Specifically, in this thesis, a commercially available implementation(Lumerical,) of the finite difference time domain (FDTD) method is used to investigate light confinement in 3-dimensional plasmonic structures.

The FDTD method is a well established numerical technique that relies on the discretization of space in units called Yee Cells(Yee, 1966) which are used to numerically approximate solutions to differential equations, in this case Maxwell's Equations. A schematic of a Yee Cell is shown in Figure 3·2 where the edges of a cube are formed by the 3 cartesian electric field component vectors and the magnetic field component

vectors are normal to the faces. In particular, the finite difference equation,

$$\frac{\delta f}{\delta x} \approx \frac{f(x+\Delta x) - f(x-\Delta x))}{2\Delta x} \tag{3.32}$$

is used to calculate derivatives, with accuracy increasing with decreasing mesh size, Δx. Maxwell's Equations can be expressed as a set of six scalar equations as,(Jin, 2011)

$$\frac{\delta E_x}{\delta t} = \frac{1}{\epsilon}(\frac{\delta H_z}{\delta y} - \frac{\delta H_y}{\delta z} - \sigma E_x) \tag{3.33}$$

$$\frac{\delta E_y}{\delta t} = \frac{1}{\epsilon}(\frac{\delta H_x}{\delta z} - \frac{\delta H_z}{\delta x} - \sigma E_y) \tag{3.34}$$

$$\frac{\delta E_z}{\delta t} = \frac{1}{\epsilon}(\frac{\delta H_y}{\delta x} - \frac{\delta H_x}{\delta y} - \sigma E_z) \tag{3.35}$$

$$\frac{\delta H_x}{\delta t} = \frac{-1}{\mu}(\frac{\delta E_z}{\delta y} - \frac{\delta E_y}{\delta z}) \tag{3.36}$$

$$\frac{\delta H_y}{\delta t} = \frac{-1}{\mu}(\frac{\delta E_x}{\delta z} - \frac{\delta E_z}{\delta x}) \tag{3.37}$$

$$\frac{\delta H_z}{\delta t} = \frac{-1}{\mu}(\frac{\delta E_y}{\delta x} - \frac{\delta E_x}{\delta y}). \tag{3.38}$$

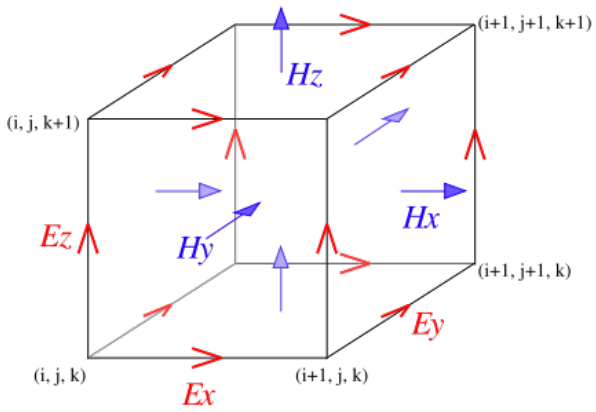

Figure 3·2: Schematic of a 3D Yee Cell who's edges are defined by the electric field vectors and faces are normal to magnetic field vectors.

In addition to the discretization of space, a discrete time step must be chosen in the FDTD method which determines the time intervals the simulation will take place at. For

each time interval the electric and magnetic field will be calculated at each of the Yee cell locations. To ensure the stability of the method care must be chosen in picking the time step, with relation to the spatial gridding. Both the spatial and temporal griding must satisfy $(\Delta x, \Delta y, \Delta z) < \lambda/20$ and $\Delta t < (\lambda/c)/20$, such that the wave nature of the light can be properly captured. It has also been shown that stability of the method requires that the spatial and temporal step sizes satisfy(Jin, 2011)

$$\Delta t \leq \frac{1}{c\sqrt{\Delta x^{-2} + \Delta y^{-2} + \Delta z^{-2}}}. \tag{3.39}$$

Using the FDTD method will allow for the calculation of the electromagnetic response of an arbitrary structure. Typically one of the most interesting calculations would be the continuous-wave (CW) response of the device over a broad wavelength range. If a CW wave was launched into the simulation it would take a long time to build to the steady state response and a separate calculation would have to be done for each wavelength making the technique far too time consuming and resource intensive for most applications. A way around this problem is to launch a short optical pulse into the system which is composed of CW waves covering a broad spectral range. The light is allowed to propagate in the system until the field has decayed to a reasonably low level and a Fourier transform of the time signal is taken to find the CW response. This method allows for the calculation of the broadband electromagnetic response with a single simulation.

One challenge introduced by using this Fourier transform is that materials with complex permittivity, which are typically specified at discrete points in the frequency domain, must be fit with a continuous time function that does not violate causality (Kramers-Kronig relations). This material data fitting is handled differently by each implementation of the software and can be done quite well for a wide range of materials.

Another aspect that must practically be considered with this method is the size of

simulation domain and the method for terminating that finite window. Obviously for the simulations to be of a reasonable computational difficulty a limited number of mesh cells must be used and since the simulation window cannot abruptly be terminated without causing a large reflection of the light (due to impedance mismatch) a method for terminating the simulation's domain must be devised. One common approach is to make the boundaries periodic so that the field at one side is set equal to the field at the other. In addition to solving the boundary problem this allows for the simulation of infinite sized structures. One limitation is that the structure can no longer be of arbitrary shape but must be periodic.

A second way to terminate the simulation boundary without causing a perturbation to the structure is with a perfectly matched layer (PML)(Berenger, 1994). A PML is a mathematically constructed material meant to absorb a wave traveling in one direction without causing any reflection. This is accomplished by applying the following transformation to the wave equation(Berenger, 1994),

$$\frac{\delta}{\delta x} \rightarrow \frac{1}{1 + \frac{i\sigma(x)}{\omega}} \frac{\delta}{\delta x} \tag{3.40}$$

leading to the following transformation in the propagating wave,

$$e^{i(kx-\omega t)} \rightarrow e^{i(kx-\omega t) - \frac{k}{\omega}\int \sigma(x')dx'} \tag{3.41}$$

which is attenuated for a positive sigma. With the boundary conditions taken care of the FDTD method can be used to simulate a device with arbitrary geometry excited by an arbitrary source, most commonly a plane wave or a point source. The FDTD method can be used to calculate the scattering, reflection, transmission, near-fields and PDOS of photonic and plasmonic devices.

3.4 Conclusions

In conclusion, the computational methods used in this thesis have been presented in this chapter. First, a detailed derivation of the electromagnetic properties of concentric multilayered cylinders has been shown using a Mie theory type approach in 2D. This method is used to calculate the electromagnetic response of multilayered cylinders to a plane wave excitation and the calculation of scattering cross section is discussed. The same method is then used to calculate the response of a multilayered cylinder to a point source excitation allowing for investigation of changes in the local density of photonic states. While this analytical method is fast and accurate, the device geometry that can be investigated is limited. To study other geometries and preform calculation of 3D devices the FDTD method is used. A summary of the FDTD method is presented and pros and cons of this method are discussed.

Chapter 4

Gap Plasmons in Coaxial Plasmonic Nanowires

Reprinted (adapted) with permission from Lawrence, N., Dal Negro, L. *Light scattering, field localization and local density of states in co-axial plasmonic nanowires*, Optics Express, Vol. 18, Issue 15, pp. 16120-32.

4.1 Introduction

Nanoscale structures consisting of layered metal and dielectric interfaces in different geometries are a promising platform for plasmonic field confinement due to the possibility of engineering plasmonic mode coupling, sub-wavelength localization and transport phenomena with unprecedented flexibility across wide spectral regions (Maier, 2007; Zia et al., 2006; Zia et al., 2004; Catrysse and Fan, 2009; Rybczynski et al., 2007; Kushwaha and Djafari-Rouhani, 2003). It has been shown that planar Metal-Insulator-Metal (MIM) slot structures support highly localized electromagnetic fields confined in nanoscale insulator regions due to the excitation of coupled plasmon modes (Maier, 2007; Zia et al., 2006; Zia et al., 2004), and optical devices based on this concept have been demonstrated(Brongersma and Kik, 2007). Additionally, circularly symmetric MIM plasmonic nanoshells and ring-disk structures have also been largely investigated in the context of hybridization plasmon theory due to their ability to strongly localize polariton fields across the visible and near-IR spectrum by tuning of their geometrical parameters(Prodan et al., 2003; Prodan and Nordlander, 2003; Hao et al., 2007). The

subwavelength field confinement achieved in these structures make them particularly attractive for a variety of nanoscale sensing and light emitting device application(Duan et al., 2003; Hu et al., 1999; Tian et al., 2007; Colombo et al., 2009).

In this chapter, using the computational method outlined in Section 3.2 for the calculation of scattering, near fields and PDOS in multilayered cylinders, concentric MIM cylindrical nanostructures, or coaxial plasmonic nanowires (CPNs) are investigated(Lawrence and Dal Negro, 2010). First, the scattering and absorption properties of two representative devices are calculated and the multiple resonance behavior of CPNs is studied by examination of the local electromagnetic fields in the device. The formation of gap plasmon modes in the dielectric region of the CPN is shown and the pattern of energy flow through the device is studied, revealing the formation of optical vortices. Next, the PDOS is calculated inside the dielectric gap region of CPNs and a large increase, over 1000X, is found at the plasmonic resonance for structures with thin dielectric gaps. Next, the tunability of resonance energy is investigated over a large range of geometrical parameters demonstrating the versatility of CPNs for use in different wavelength regions. By studying the shift in resonance energy the coupling mechanism which give rise to the behavior are also explored. Next, the possibility of achieving similar behavior in circular multilayered dielectric structures is explored. Confinement of light to low index regions due to the continuity of electric displacement in these structures is shown to produce subwavelength light confinement as well as increased PDOS in devices with no optical losses. A fabrication method for multilayered pillars is demonstrated and some preliminary optical measurements are shown.

4.2 Optical Properties of CPNs

In this section, an overview of the scattering and near field enhancement properties of CPNs is presented by investigating two representative structures with the method

shown in Section 3.2.1 which calculates the response of a multilayered cylinder to a plane wave excitation. The structures each consist of 3 layers having an inner metallic core surrounded by a thin dielectric layer and then a thin outer metal coating. For the metallic layer Ag is chosen due to its large negative permittivity and low loss in the visible and NIR (material data from (Johnson and Christy, 1972)), and SiO_2 (n=1.5) is used for the dielectric gap region. The first structure under consideration will have an inner core radius of 60nm, a dielectric gap thickness of 50nm and an outer metal cladding thickness of 20nm. The second will have a smaller dielectric gap thickness of 12nm and identical metallic regions.

4.2.1 Scattering and Absorption

The scattering and absorption efficiencies for the two structures are shown in Figure 4·1. In Figure 4·1(a) the scattering (blue) and absorption (green) is shown for the device with a 50nm dielectric gap which simultaneously supports strong plasmonic resonances in the visible and in the near-IR spectral regions. In Figure 4·1(b) the scattering (blue) and absorption (green) is shown for the device with a 12nm dielectric gap supporting similar resonances but with significantly reduced scattering resonance. The dotted blue line in Figure 4·1(b) shows the scattering of the same device when the dielectric region is filled with Ag as a limiting case. For both devices there are increases in the absorption that coincide with the increased scattering efficiency due to local field enhancement at the plasmonic resonance. The scattering cross section interestingly displays an asymmetric shape with a decrease in the scattering at wavelengths shorter than the resonance. We find that the scattered far-field can be almost entirely suppressed at the wavelengths of the scattering dips in Figure 4·1(a) and Figure 4·1(b), while the internal field in the dielectric gap remains appreciably high. These spectra are calculated by excitation with a TE polarized plane wave.

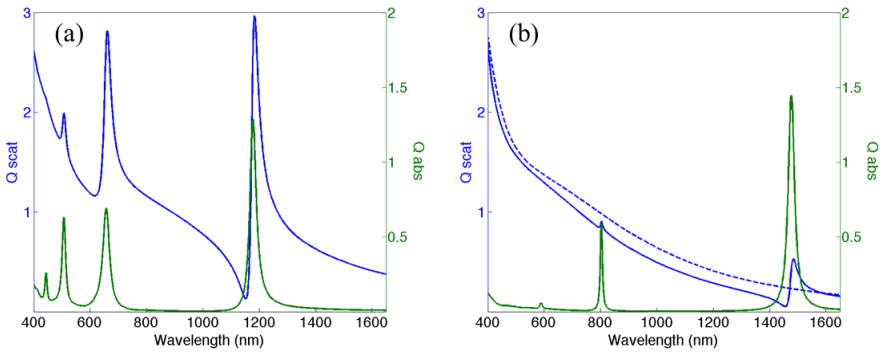

Figure 4·1: (a) and (b) show the scattering efficiency (blue) and absorption efficiency (green) for two different MIM structures. The insulating layer for (a) has a thickness of 50nm and the insulating layer for (b) has a thickness of 12nm. The radius of the inner metallic core for both structures is 60nm and the outer shell thickness is 20nm. The blue dotted line in (b) is the scattering efficiency for a solid Ag wire 92nm radius.

4.2.2 Local Field Enhancement

In order to further understand the physical nature of these plasmonic resonances the electric field profiles of strongly scattering resonances corresponding to the structures in Section 4.2.1 are calculated using the expression for the field in Equation 3.4. The electric field (relative to a plane wave with unity strength) excited at 1152nm in an MIM device with 50nm gap thickness is plotted in Figure 4·2 (a) where a dipolar type field profile is seen with strong localization to the dielectric gap region. Figure 4·2 (b,c) show the electric field for the 12nm gap structure discussed earlier, excited by a plane wave at a wavelength of 1492nm and 803nm, respectively. Here we see in (b) that a similar dipolar mode has been excited once again with strong field confinement to the gap region. In (c) a quadrupolar type mode with 4 minima/maxima of the electric field has been excited at a shorter wavelength. In both (b,c) the electric field strength is significantly higher than in (a) due to confinement of the field to a smaller region.

To further characterize the near field properties of CPNs the radial and azimuthal components of the electric field are plotted in Figure 4·3. Since these modes are excited

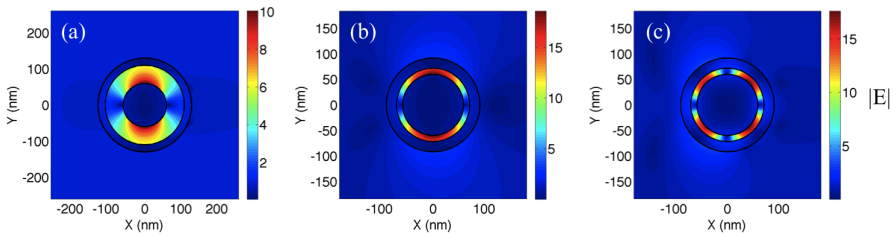

Figure 4·2: (a) Shows the electric field for an MIM structure with inner radius of 60nm, dielectric gap thickness of 50nm and outer metal shell thickness of 20nm excited by a plane wave at 1152nm. (b,c) Shows the electric field for an MIM structure with inner radius of 60nm, dielectric gap thickness of 12nm and outer metal shell thickness of 20nm excited by a plane wave at wavelengths of 1492nm and 803nm respectively.

by a plane TE wave there is no electric field component out of the plane. We can see from Figure 4·3 that the electric field amplitude corresponding to the strongly confined plasmon modes is primarily radially polarized within the sub-wavelength dielectric gap regions. This is consistent with the excitation of a gap plasmon mode between the two metal dielectric interfaces. The azimuthal components of the fields, Figure 4·3 (d-f), are found to be much weaker and spread spatially throughout the structures. The discontinuity of the field at the metal-dielectric interface demonstrates a build up of charge and formation of plasmon polaritons.

4.2.3 Optical Vortices

To learn more about the formation of plasmon resonance in CPNs the energy flow through the structure is calculated by plotting streamlines parallel to the Poynting vector. Interestingly, the formation of optical vortices is found in CPNs. Optical vortices (or whirlpools) are formed by closed loops of the Poynting vector flow and have been shown to form in nanoparticles based on studies using analytical Mie theory(Wang et al., 2004; Bashevoy et al., 2005). The formation of an optical vortex shows the location of an energy sink within the nanostructure. Interestingly, optical vortices have the

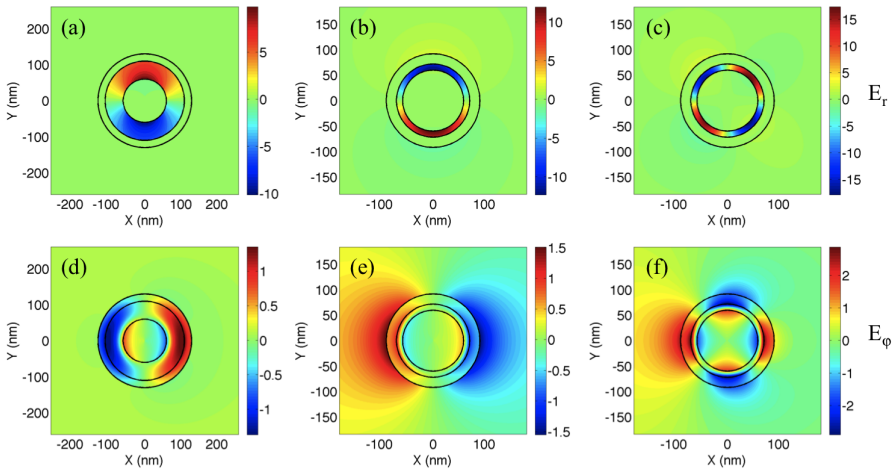

Figure 4·3: Electric field components for the field profiles shown in Figure 4·2. (a-c) shows the radial component of the field at the same excitation wavelength as Figure 4·2 (a-c) respectively. (d-f) shows the azimuthal field component of the field.

potential to induce optical bistability and hysteresis effects on the nanoscale. Recently it has been shown (Wang et al., 2004) that two different types of whirlpools exist in plasmonic nanoparticles. In the so-called outward vortex, the energy flow streamlines first penetrate into the particle near its center then, on exiting the particle, the flow lines turn away from the centerline and begin a spiral trajectory. These vortices are formed at wavelengths shorter than the dipolar plasmon resonance. For wavelengths longer than the plasmon dipolar resonance, inward vortices can form, and their power streamlines pass around the sides of the particle before entering the particle to enter a spiral trajectory.

Figure 4·4 shows optical vortex formation around the dipolar resonance of the 12nm dielectric gap structure as the excitation wavelength is increased from 1462nm, to 1482nm and finally 1492nm in Figure 4·4 (a-c) respectively. In Figure 4·4 a planewave is incident from the left side of the panel and the Poynting vector streamlines go from left to right. In Figure 4·4 (a) most of the flow lines go around the outside of the particle while some go inside traveling through the dielectric gap region, still going left to right,

and back out again. A few of the lines terminate inside the particle indicating absorption of light. As the excitation wavelength increases, in Figure 4·4 (b) the direction of energy flow inside the dielectric region switches, now opposing the direction of energy flow outside the structure. As the wavelength increases further, Figure 4·4 (c) shows the formation of an optical vortex centered around the outer layer of metal. This complex whirlpool behavior, similar to the formation of inward vortices, in agreement with (Bashevoy et al., 2005), can additionally be supported by the quadrupolar resonances of CPNs.

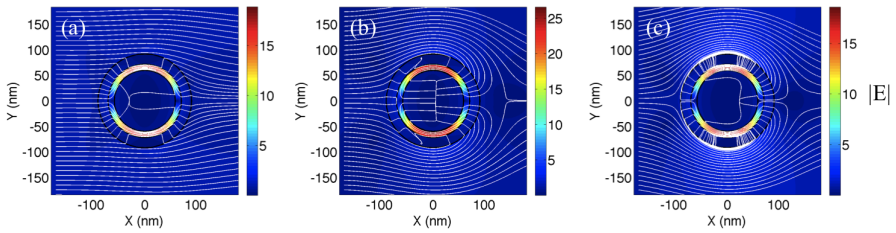

Figure 4·4: Electric field magnitude with streamlines parallel to the Poynting vector in an MIM structure with a 12nm gap identical to the one shown in Figure 4·2. (a-c) Excitation wavelengths are 1462nm, 1482nm and 1492nm respectively.

4.3 Radiation Rate Modification in CPNs

In this section modification of the photonic density of states (PDOS) caused by light confinement in CPNs is investigated. The method for the calculation of the PDOS is presented in Section 3.2.2 and all results shown are for randomly oriented sources where the PDOS has been normalized to the PDOS in a homogeneous medium. Increases in the PDOS cause a change in the radiative decay rate inside the resonator and can lead to enhanced light emission intensity, quantum efficiency and lasing at reduced Q factors.

4.3.1 Enhancement of the Photonic Density of States

Since the PDOS is calculated for a particular point in the structure, calculations with many source locations must be carried out. Luckily this can be done relatively fast using the matrix formulation presented in Chapter 3 as the location of the source is separated from the matrix describing the problem. Changing the source location can be done without subsequent matrix inversions, the most time consuming part of the calculation. By placing a source at different points in the structure and varying the wavelength of the source the enhancement of the PDOS by CPNs is investigated.

The largest change in the PDOS takes place for sources inside the dielectric gap which is consistent with the localization of the electric field to this same region under plane wave excitation. In fig. Figure 4·5 the PDOS calculated at the center of the dielectric gap region from a randomly oriented dipole source is shown for the two structures investigated in Section 4.2. At wavelengths corresponding to the plasmonic resonances of the device the PDOS is increased significantly, reaching a maximum of over 1000 times that of a homogeneous medium. In comparison to excitation by a planewave the higher order resonances are more pronounced in the PDOS due to the ability of localized fields to more efficiently excite higher order modes in the device. The PDOS enhancement in Figure 4·5 (b) is stronger than in (a) due to the stronger confinement of light in a smaller dielectric gap region. The multiple resonance behavior offers the potential to simultaneously enhance radiative processes at multiple wavelengths. In order to better engineer this effect a systematic study of the PDOS enhancement for varying refractive indices and geometrical parameters is carried out later in this chapter.

4.3.2 Radiated Power

Another important device aspect to investigate is the absorption of light due to the large amount of metal in MIM devices. If the PDOS is enhanced but most of the emitted light

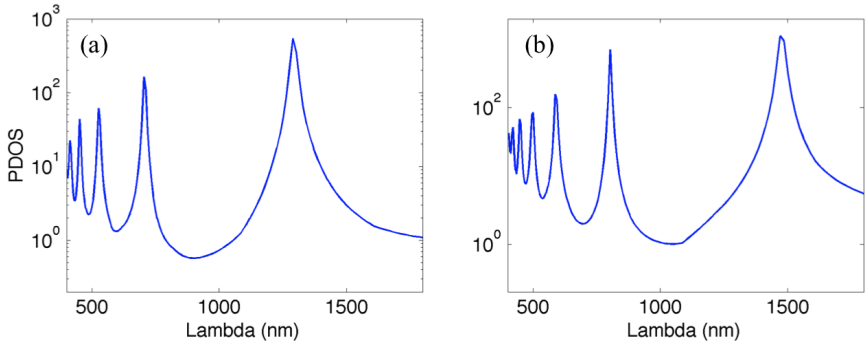

Figure 4·5: The PDOS for a randomly oriented point source placed in the center of the dielectric region of CPNs is plotted normalized to the PDOS in a homogeneous medium. (a,b) correspond to the two different structures investigated in Section 4.2. Device in (a) has inner radius of 60nm, dielectric gap thickness of 50nm and outer metal shell thickness of 20nm. Device in (b) has inner radius of 60nm, dielectric gap thickness of 12nm and outer metal shell thickness of 20nm.

is absorbed locally it is unlikely that the total energy radiated away the device will be increased. Using the theory derived in Section 3.2.2 we can calculate the rate that light is radiated to the far-field and the rate of light absorption within the device. Looking at the same two devices from Figure 4·5, in Figure 4·6 the normalized PDOS (blue) is plotted along with the density of states that result in light emission to the far-field (red) and absorption within the device (green). We can see that in the device with a 12nm gap (a) the total increase in density of states is larger but that the rate of absorption is significant, almost 3/4 of the emitted photons will be absorbed. In contrast the device with 50nm gap (b) thickness has a lower rate of absorption but about 2/3 of the emitted photons will radiate to the far field. It is also interesting to note that at shorter wavelengths the portion of radiated photons drops and the absorption increases. This is likely due to the fact that the skin depth of light propagation is shorter and photons are unable to escape through the outer metallic layer. Though the field enhancement and PDOS is highest in small dielectric gap structures, this comes with increased light absorption due to the closer proximity of metallic layers. This analysis shows that rate

of absorption is an important factor which must be considered in the overall device design, smaller dielectric gaps may not always lead to the best performance.

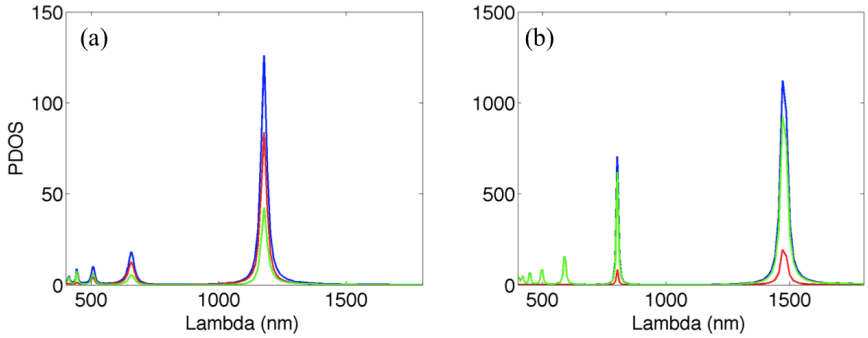

Figure 4·6: The PDOS for a randomly oriented point source placed in the center of the dielectric region in an MIM cylindrical devices is plotted normalized to the PDOS in a homogeneous medium. (a,b) correspond to the two different structures investigated in Section 4.2. Device in (a) has inner radius of 60nm, dielectric gap thickness of 50nm and outer metal shell thickness of 20nm. Device in (b) has inner radius of 60nm, dielectric gap thickness of 12nm and outer metal shell thickness of 20nm. Blue is the total relative PDOS, red shows the density of states that lead to radiation of light to the far-field and green shows the density of states that lead to absorption in the device.

4.4 Engineering Resonance in CPNs

In order to engineer the resonant behavior of CPNs for a particular device application or wavelength of operation it is necessary to investigate the respective roles of geometry and dielectric index on the optical response of these complex structures. In this section, a systematic study is undertaken of each of the geometrical parameters of CPNs to determine its effect on plasmon mode formation. The analytic method developed for multilayered cylinders is ideally suited to this type of large parametric study due to the relative speed of the algorithm. In this study the geometrical parameters, inner core size, dielectric gap thickness and outer metallic core thickness will be varied and the device response will be calculated over a wide bandwidth. This will require a very large

number of independent calculations, each requiring only a small amount of memory. The Boston University College of Engineering computational grid is well suited to this task and has been used for computation.

4.4.1 Geometry Dependent Scattering Resonance

To study the effect of geometry on the far-field response of CPNs I have calculated the scattering efficiency under illumination by a TE polarized plane wave. The sketch in Figure 4·7 (a) shows the geometry of the device and parameters which are varied, namely the radius of the core region (referred to as r_1), the thickness of the dielectric layer (referred to as d_2), and the thickness of the outer metal shell (referred to as d_3). The results of the analysis, shown in Figure 4·7, reveal the formation of two main resonances observed in the scattering efficiency corresponding to the dipolar and the quadrupolar modes of the structures. The intensities of these resonances are maximized within separate wavelength regions, depending on the geometrical parameters and the dielectric index of the structures.

The plot in Figure 4·7 (b) show the scattering efficiency as a function of r_1 and wavelength. The other two geometrical parameters of the structure are kept constant at $d_2 = 20nm$ and $d_3 = 20nm$, while the dielectric gap index is fixed at $n = 1.5$. We notice that strong dipolar and quadrupolar resonant peaks can be supported for a wide range of r_1 values. As the size of the core increases in radius from 10nm to 100nm, both resonances red-shift almost linearly, the dipolar resonance shifting at a higher rate across the entire visible and near-IR spectrum (up to 1650nm). This can be explained by a simple azimuthal standing wave model where resonances are formed when half integer numbers of wavelengths close around the core of the structure. We found that the scattering efficiency of the dipolar mode is optimized for a smaller core size around r_1=30nm. On the other hand, the scattering efficiency of the quadrupolar mode remains

very small across the entire parameter space.

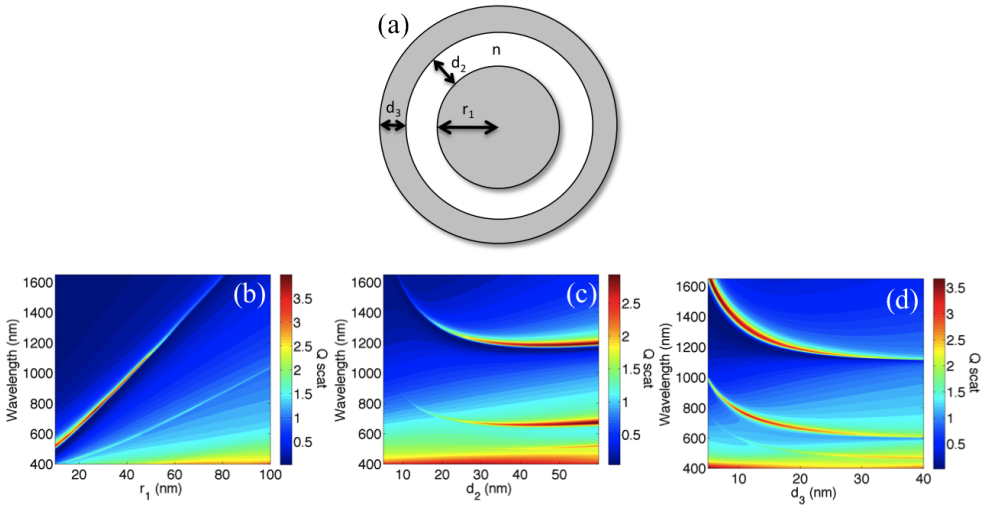

Figure 4·7: (a) geometry used for studying structural resonance where the gray layers are Ag and the dielectric gap region has refractive index n=1.5, illuminated by a TE planewave. (b) shows the scattering efficiency as a function of wavelength and inner core radius r_1 with $d_2 = 20nm$ and $d_3 = 20nm$. (c) shows the scattering efficiency as a function of wavelength and dielectric gap thickness d_2 with $r_1 = 60nm$ and $d_3 = 20nm$. (d) shows the scattering efficiency as a function of wavelength and outer metal cladding thickness d_3 with $r_1 = 60nm$ and $d_2 = 20nm$.

In Figure 4·7 (c) the effect of thickness variations of the dielectric layer d_2 on the resonances of the structure is studied, while other parameters are fixed at $r_1 = 60nm$, $d_3 = 20nm$ and $n = 1.5$. The scattering efficiency shows two largely tunable resonance bands with energy undergoing a non-linear blue-shift as the thickness of the dielectric region is increased to 40nm. At thicknesses larger than 40nm the resonance energy remains roughly constant. This behavior is understood based on the plasmon hybridization model(Prodan et al., 2003; Hao et al., 2007) where the resonances of the CPN systems originate from the hybridization of coupled modes of the core and outer metallic shell. Therefore, by increasing the thickness of d_2 the coupling between these modes decreases and shifts the resonance of the coupled system to shorter wavelengths (larger energy). Moreover, as already discussed in Figure 4.2.1, the scattering efficiency of CPN

systems dramatically reduces by decreasing the dielectric gap thickness, since dark plasmon modes form inside the dielectric region. In Figure 4·7 (d) the tunability of the resonances with respect to the thickness of the outer metallic layer is shown, while fixing $r_1 = 60nm$, $d_2 = 20nm$ and $n = 1.5$. Two distinct modes (dipolar and quadrupolar) can be clearly observed and their spectral positions blue-shift non-linearly by increasing d_3, similar to changes in d_2. Once again, this effect is due to the reduced coupling of the hybridized resonances(Prodan et al., 2003; Hao et al., 2007; Prodan and Nordlander, 2003). Finally, Figure 4·7 (d) shows that within the range of interest (5nm-40nm) the scattering efficiency drops significantly by increasing the metallic outer layer thickness, since external plane waves cannot penetrate into the structure.

4.4.2 Geometry Dependent PDOS

In this section the effect of changing geometry and refractive index on the relative PDOS in CPNs is explored. Figure 4·8 (a) shows the calculated PDOS as a function of wavelength and r_1, the radius of the metallic core, while the other parameters are fixed to $d_2 = 20nm$, $d_3 = 20nm$ and $n = 1.5$. Multiple resonances occur in Figure 4·8 (a) and as the core size increases, all the resonances in the PDOS red-shift and their intensity increases. Figure 4·8 (b) shows the effect of varying the thickness of the dielectric layer d_2, while the other parameters are fixed to $r_1 = 60nm$, $d_3 = 20nm$ and $n = 1.5$. As the size of the dielectric gap decreases the strength of the relative PDOS increases strongly as energy is confined to a smaller volume. For both cases, shifts in the resonant energy follow the shifts observed in the far-field.

Next, the effects of varying the refractive index of the dielectric gap layer are explored. In order to keep the analysis simple, a CPN structure with fixed geometry $r_1 = 60nm$, $d_2 = 20nm$, $d_3 = 20nm$ and a purely real refractive index is considered. The results in Figure 4·8 (c) show that the dipolar and quadrupolar resonances can be

engineered across a wide range of refractive index values. As the refractive index increases the resonance energy decreases, consistent with typical red-shifting behavior at higher refractive indices in plasmonics. The results in Figure 4·8 demonstrate that it is possible to obtain large PDOS enhancement within deep sub-wavelength gaps (20nm) at both the dipolar and quadrupolar resonances across the entire range of explored refractive index values, potentially enabling significant light emission/absorption enhancement effects at multiple wavelengths in a large range of dielectric materials. Based on this analysis, CPN structures can be flexibly optimized, for instance, to strongly confine and to resonantly increase the pump intensity and PL radiation rate within nanoscale dielectric layers over well-separated spectral regions, paving the way to the engineering of novel plasmonic nanowires devices for multi-spectral light emission, energy harvesting and optical sensing .

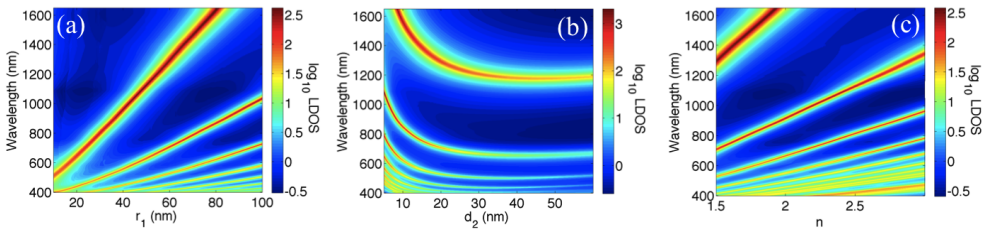

Figure 4·8: Relative PDOS is calculated with varying geometrical parameters and dielectric gap index. (a) shows the relative PDOS as a function of wavelength and inner core radius r_1 with $d_2 = 20nm$, $d_3 = 20nm$ and $n = 1.5$. (b) shows the relative PDOS as a function of wavelength and dielectric gap thickness d_2 with $r_1 = 60nm$, $d_3 = 20nm$ and $n = 1.5$. (c) shows the relative PDOS as a function of wavelength and outer metal cladding thickness d_3 with $r_1 = 60nm$, $d_2 = 20nm$ and $n = 1.5$.

4.5 Light Confinement in Multilayered Dielectric Pillars

In addition to light confinement by the excitation of surface plasmons light can be confined in purely dielectric materials. Two examples of this are the formation of guided

modes in optical fibers or modes in dielectric resonators such as micro-disk and micro-ring resonators. In both cases light is confined by total internal reflection in a high index medium. In contrast to confinement by surface plasmons, in these cases it is typically not possible to confine light in volumes smaller than a cubic wavelength. However, it has been recently shown that subwavelength light confined is possible in low index gaps within dielectric structures. One example of this phenomenon is the slot waveguide where a low index gap is formed between two high index materials. The contrast of the refractive index and continuity of the electric displacement across the boundary between the two materials causes an increase in the electric field inside the gap for light polarized with electric field vector normal to the interface(Creatore et al., 2009; Jun et al., 2009). Studies on slot waveguides have focused on planar structures however if the same light confinement properties can be exploited in other geometries, such as in cylinders, low loss, subwavelength field confinement with resonant behavior may be possible.

The analytical method used to study CPNs is also well suited to investigate purely dielectric multilayered cylinders. Light confinement should be possible in multilayered cylinders within a thin layer of material having a low refractive index surrounded by layers with higher refractive indices, termed a low index gap cylinder (LIGC). The analysis presented here will focus on Si-based materials with the high index core and outer cladding regions composed of Si (n=3.5) and the low index gap region composed of SiN (n=2). For simplicity material dispersion is ignored in this analysis.

The results of PDOS and near field intensity calculations for LIGCs using the multilayered cylinder code are presented in Figure 4·9. Figure 4·9 (c) shows the relative PDOS calculated for a randomly oriented source in the gap region of a LIGC with inner high index core radius $r_1 = 175nm$, low index gap thickness $d_2 = 30nm$ and outer high index cladding thickness $d_3 = 75nm$. There are two resonances which form in the near-IR spectral range that show an increase in the PDOS. Though the increase

is much smaller than in metallic structures it can be achieved without introducing any material loss. The electric field inside the low index gap structures is calculated (under TE planewave excitation) to examine resonant behavior further. Figure 4·9 (a) shows the electric field amplitude excited at 1130nm and Figure 4·9 (b) shows the electric field excited at 1513nm. Both wavelengths show localization of energy to the gap region, the field at 1513nm shows the excitation of a dipolar mode and at 1130nm the excitation of a quadrupolar mode, similar to CPN devices. The LIGC provides a second platform to achieve radiation rate enhancement due to strong field confinement however without the introduction of large optical losses due to the presence of metal.

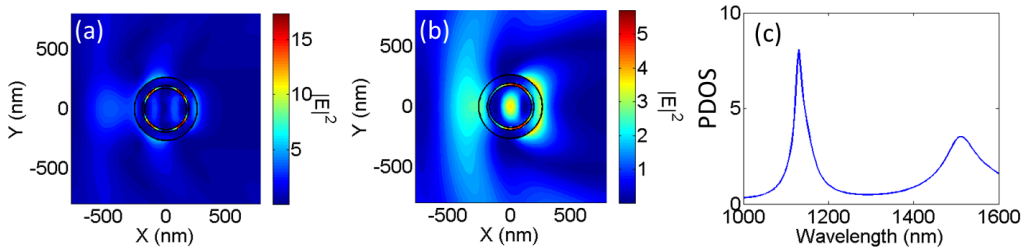

Figure 4·9: Near-field intensity and PDOS for a low index gap nanopillar made of Si and SiN. (a) Near-field intensity of a low index gap nanopillar excited by a plane wave at 1130nm showing a quadrupolar mode confined in the gap region. (b) Near-field intensity of a low index gap nanopillar excited by a plane wave at 1513nm showing a dipolar mode confined in the gap region. (c) Relative PDOS for a randomly oriented point source located in the center of the low index gap region.

4.6 Fabrication and Characterization of High Aspect Ratio Pillars

The simulations of multilayered cylinders so far were done in two-dimensions therefore fabrication of devices exactly matching the calculations is impossible. Many studies have shown though that high aspect ratio structures can be approximated by two-dimensional simulations very well so the first attempt made to fabricate multilayered

cylinders was using top-down fabrication techniques to create high aspect ratio pillars. Top-down fabrication of high aspect ratio metal pillars is challenging due to the typically poor performance of anisotropic etching techniques on metals. However, anisotropic etching of Si is significantly easier, either by wet etching along crystallographic grain boundaries or by plasma etching. Starting with a silicon pillar, conformal sputtering can be used to coat pillars and realize multicoated high aspect ratio pillar systems. Figure 4·10 shows a schematic of the pillar fabrication process for multilayered MIM cylinders. Figure 4·10 (a) shows the fabrication process flow for high aspect ratio Si pillars starting with electron beam lithography using poly-methyl methacrylate (PMMA) electron beam resist. The exposed areas of the resist are developed using a 1 to 3 mixture of methyl iso butyl ketone and isopropyl alcohol (1 MIBK : 3 IPA) and a thin layer of Al is deposited by electron beam evaporation. The remaining PMMA and excess Al are removed by liftoff in Acetone leaving a pattern of Al on a Si substrate. Reactive ion etching (RIE) is used to transfer the Al pattern to the underlying Si material in an inductively coupled plasma RIE system where a mixture of SF_6 and CH_4 is used to achieve a highly anisotropic etch profile. Finally, the remaining metal is removed with a commercially available Al etchant to leave high aspect ratio Si pillars. Figure 4·10 (b) shows a schematic of the coating of the pillars by conformal sputtering. Deposition of materials by sputtering can be less directional than by evaporation because sputtering is done in a higher pressure environment. Collisions between the sputtered ions and gas in the chamber during deposition will somewhat randomize the trajectory of the ions to create a conformal layer. Additionally in the sputter chamber at Boston University the targets are angled with respect to the sample positioning (consistent with drawing) and the sample stage is rotating during deposition which should increase the uniformity of the pillar coverage. The schematic in Figure 4·10 (b) shows the coating of a Si pillar with subsequent layers of Ag, SiN and Ag to form a CPN. Though the center Si region

was not present in the 2D simulations of CPNs, if the inner metal layer is sufficiently thick little light will leak through and only a small perturbation in the device behavior will be caused.

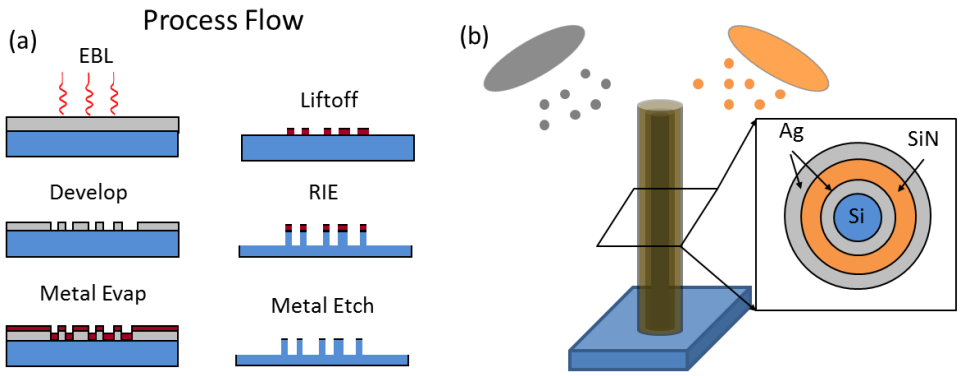

Figure 4·10: (a) Process flow for Silicon pillars by electron beam lithography (EBL) and reactive ion etching (RIE) (b) Schematic of CPN fabrication by sputter.

Results of fabricated CPNs are shown in Figure 4·11. Figure 4·11 (a) shows a scanning electron micrograph (SEM) of an array of multicoated high aspect ratio pillars and Figure 4·11 (b-e) shows single pillars at each stage during fabrication. Figure 4·11 (b) shows the initial Si pillar made by the process flow in Figure 4·10 (a). The pillar shown here has a diameter of 120nm and a height of $1.5\mu m$ giving it an aspect ratio of 12.5, sufficient to be considered 2D. Figure 4·11 (c) shows the Si pillar after coating with a conformal layer of Ag. Figure 4·11 (d) shows the same structure after deposition of a layer of Er:SiN and Figure 4·11 (e) after a final coating with Ag. The schematics below the images show a pillar cross section where, blue is Si, gray is Ag and orange is Er:SiN.

The same process can be used to make purely dielectric pillars by sputtering Si instead of Ag to coat the pillars. In Figure 4·12 fabricated multilayered dielectric pillars are shown. Figure 4·12 (a1-3) shows Si pillars of varying size, made with electron beam lithography and reactive ion etching. Figure 4·12 (b1-3) shows the same devices with a

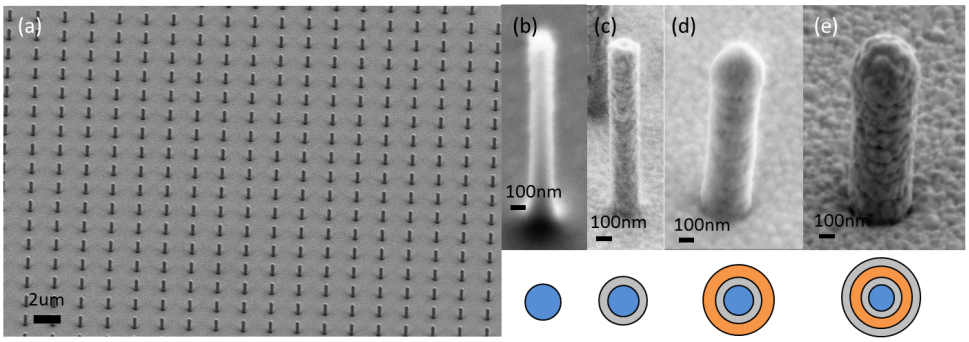

Figure 4·11: (a) SEM of an array of CPNs (b-e) SEM of single CPN after each step of processing, (b) Si pillar, (c) Si pillar after Ag metallization, (d) Addition of Er:SiN dielectric layer, (e) Addition of final metal layer.

conformal coating of Er:SiN_x applied with RF reactive cosputtering. Figure 4·12 (c1-3) shows the same devices once again after a conformal coating of aSi has been sputtered to form multicoated dielectric pillars. Figure 4·12 (a4-c4) shows a schematic of the structure at each step. The thickness of the Er:SiN_x coating is 35nm and the thickness of the outer aSi coating is 130nm.

To verify the quality of the fabricated devices, passive optical measurements are made and compared to 2D analytic calculations. Calculations of the scattering cross section for Si pillars of varying diameter are shown in Figure 4·13 (a) and dark-field scattering measurements from fabricated pillars of matching sizes are shown in Figure 4·13 (b). Overall, an excellent agreement between the calculated and measured data of the Si pillars is found. This indicates that the scattering is not adversely affected by any pillar roughness or the presence of the substrate. Also, the pillars are of sufficient length to be approximated by 2D simulations.

Next, dark field scattering measurements of multilayered dielectric pillars are made and compared to scattering calculations made using 2D analytical theory. Calculated scattering spectra for devices of varying inner Si pillar diameter, all with 35nm coatings of Er:SiN_x and 130nm coatings of aSi, are shown in Figure 4·12 (a). Scattering signal

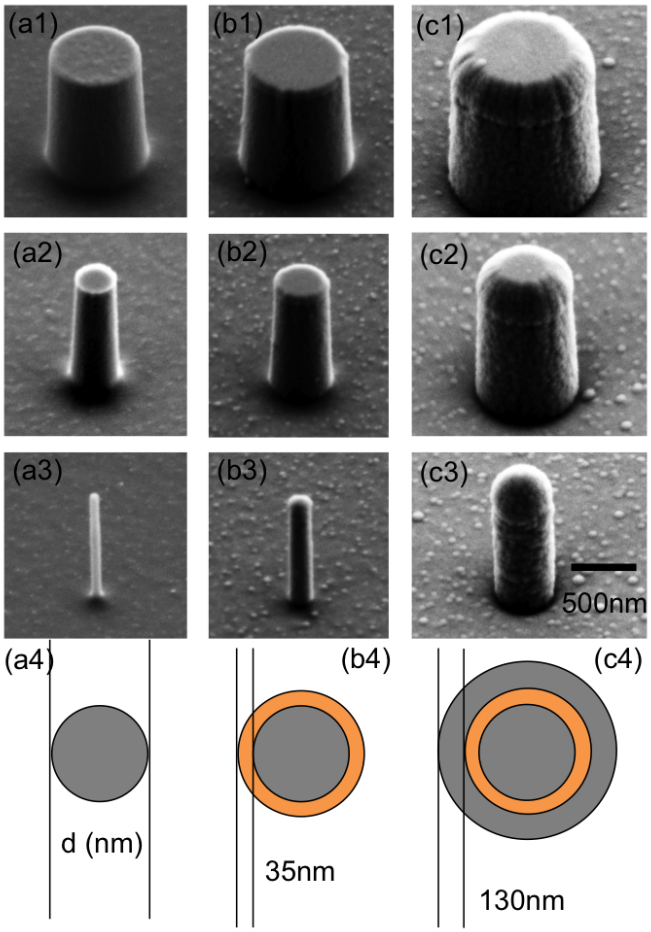

Figure 4·12: (a) SEM of an array of CPNs (b-e) SEM of single CPN after each step of processing, (b) Si pillar, (c) Si pillar after Ag metallization, (d) Addition of Er:SiN dielectric layer, (e) Addition of final metal layer.

is plotted in arbitrary units and spectra are offset for clarity. The scattering for the largest pillar diameter, 492nm, shown in red. A dip in signal around 1050nm and a peak around 1300nm are observed. As the pillar size decreases, both of these features blue shift and a second scattering dip becomes apparent. When we compare these data to the measured scattering spectra in Figure 4·12 (b) we see that the measured data show some similar looking features. However, the features of the measured data do not shift as much with changing pillar size as those in the theoretical study. The differences in measured and simulated scattering could be due to scattering from the ends of the

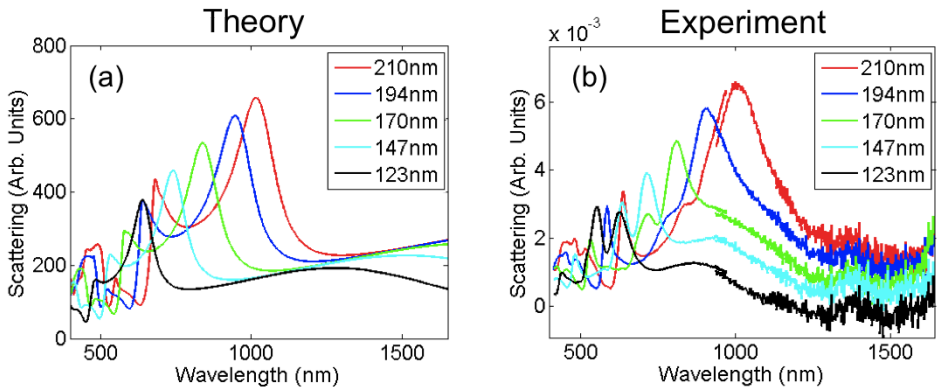

Figure 4·13: (a) In plane scattering of single Si pillar using 2D Mie theory with an unpolarized excitation. (b) Dark-field scattering of Si pillars. Legend denotes diameter of pillar.

wires that is not captured by the simulation. Some of the pillar devices studied here are also quite wide and it is possible that their aspect ratio is too low to be approximated by a 2D simulation. Using this data it is hard to show conclusively that a particular mode of the structure is being excited.

The fabrication of multilayered pillars structures by etching of high aspect ratio structures and coating with conformal sputtering has been demonstrated for both MIM and dielectric devices. This process can be modified to incorporate a large variety of materials due to the versatility of RF sputtering. Dark field scattering measurements of bare Si pillar are performed and shown to be in excellent agreement with analytical 2D calculations. Scattering measurements of multilayered dielectric pillar systems are also carried out and while some similarities are seen with calculations, the correspondence does not conclusively show the formation of highly confined modes. Discrepancies could be caused by finite length effects in the pillars or by roughness at the material interfaces. Taller pillars could be made to reduce finite size effects and modifications to the sputtering process could be made to reduce roughness. This is currently an ongoing work.

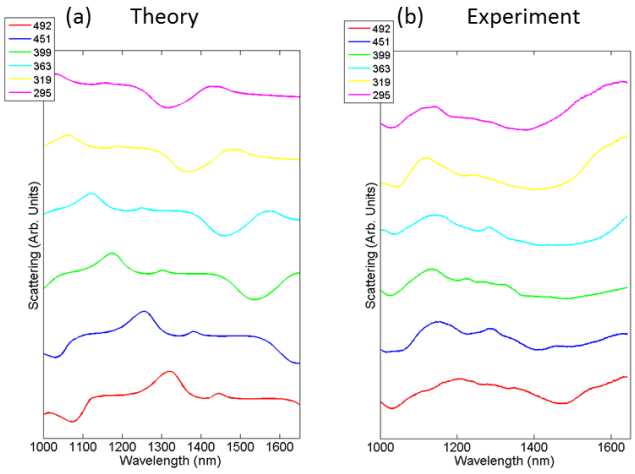

Figure 4·14: (a) In plane scattering of single multilayered dielectric pillar using 2D Mie theory with an unpolarized excitation. (b) Dark-field scattering of multilayered dielectric pillars. Legend denotes diameter of the inner Si pillar. Pillar coatings are those shown in Figure 4·12

4.7 Conclusions

In conclusion, theoretical studies of infinite multilayered cylinders have been presented in this chapter using the computational method presented in Chapter 3. Deep subwavelength plasmon modes in CPNs have been investigated by studying the near-field enhancement, scattering/absorption spectra, energy flow and PDOS. Multiple resonances in CPNs are found to strongly increase the local electromagnetic field and PDOS across wide wavelength bands. A systematic study of the resonant behavior with changes in geometrical device parameters is presented, showing how CPNs can be engineered for different applications and giving insight into the physical mechanism leading to plasmon mode formation. Multilayered cylinders composed of purely dielectric materials are studied and field confinement is shown in deep subwavelength low index gap regions. The localized modes found in dielectric devices could be used for light confinement, as an alternative to plasmon formation, but with low loss. A fabrication method for multilayered pillars is presented which uses top-down lithography to make high aspect

ratio Si pillars followed by conformal sputtering to make multilayered structures. Scattering measurement of both bare and multicoated pillars are performed and compared to analytical theory. While the scattering of bare Si pillars is in excellent agreement with calculations, the scattering of multilayered dielectric pillars is not as well captured by 2D simulations. Measurements have not conclusively shown the formation of highly confined modes in multilayered dielectric pillars. Work in this area is ongoing.

Chapter 5

Radiation Rate Enhancement in Subwavelength Plasmonic Ring Nanocavities

5.1 Introduction

The development of efficient light sources (lasers and LEDs) with subwavelength size is an ongoing challenge in the fields of plasmonics and nano-optics(Vahala, 2003; Ma et al., 2013). Nanoscale light sources can potentially find many applications in integrated optical data processing, sensing and cavity quantum electrodynamics due to the confinement of light into subwavelength volumes. In particular, the engineering of plasmon excitations in light-emitting metal-dielectric nanostructures could provide solutions for the high-density integration of digital logic platforms operating with optical bandwidths at the nanoscale(Shalaev and Kawata, 2006; Zia et al., 2006; Miller, 2009). In the last several years, the manipulation of light-matter interaction using plasmonic resonances in nanoscale devices has been demonstrated in a wide range of geometries and active materials (Khajavikhan et al., 2012; Oulton et al., 2009; Altug et al., 2006). However, in order to achieve scalable and cost-effective integration of optical data with nanoscale microchip technology, the compatibility with complementary metal oxide semiconductor

(CMOS) processing is crucial.

As discussed previously in this thesis, Er-doped dielectrics, such as SiO_2 or Si_3N_4, are well established CMOS-compatible materials for the efficient generation of light at telecom wavelengths. Er doped fiber lasers have been widely utilized for long-distance optical transmission(Desurvine, 1994). However, the very small emission cross-section ($\sigma = 4 \times 10^{-21}\text{cm}^2$) of Er ions combined with the onset of clustering phenomena precluding doping levels in excess of $10^{21}/\text{cm}^3$, have limited the maximum material gain in Er-based dielectrics to about 7dB/cm (Kippenberg et al., 2006). As a result, quality factors (Q) larger than 10^5 are necessary in order to achieve Er lasing on a Si-based chip, as demonstrated using micro-disks and micro-toroids(Kippenberg et al., 2006; Polman et al., 2004) resonator structures. Q factors of this magnitude are typically not attainable in photonic nanostructures due to large radiative losses, nor in plasmonic structures where Q factor is limited by energy loss in metal layers. On the other hand, optical cavities can significantly increase the spontaneous emission rate of active materials due to modifications in the local density of photonic states (PDOS) (Purcell, 1946; Vahala, 2003). As a result, the engineering of nanocavities with large Purcell enhancement can provide lasing at reduced Q factors due to increases in the stimulated emission rate.

In the previous chapter, light confinement in gap plasmon modes within circular metal-insulator-metal cylinders (CPNs) was discussed and it was shown that these nanostructures can lead to the strong increases of radiative processes in highly tunable subwavelength modes. A method for the fabrication of high aspect ratio multicoated pillars was presented which was ultimately unsuccessful for realizing multilayered plasmonic active devices. Though the fabrication of multicoated high aspect ratio structures is very challenging previous studies have shown similar plasmon modes exist in nanostructures with lower aspect ratio that consist of a thin dielectric ring of material, embedded in metal, referred to here as plasmonic ring nanocavities(Vesseur et al., 2010;

Lawrence and Dal Negro, 2013).

In this chapter plasmonic ring nanocavities are designed, fabricated and characterized which consist of deep subwavelength active annular regions of Er:SiO_2 embedded in Ag. Gap plasmon modes provide confinement of light to volumes as small as $0.01\left(\frac{\lambda}{n}\right)^3$ while the cavity geometry provides tunability of the resonance energy over a wide range. The increase in the radiative emission rate in such metallic nanocavities is hard to quantify using time-resolved emission measurements alone, since large modifications in the non-radiative rate, pumping efficiency and collection efficiency can simultaneously be present. Therefore in this chapter photoluminescence lifetime, intensity, reflection spectroscopy and device modeling based on three-dimensional (3D) full-vector Finite Difference Time Domain (FDTD) simulations are combined in order to rigorously quantify the Purcell-induced modifications of the total decay rate, radiative decay rate and quantum efficiency of Er ions. Ultimately, a 25 times increase in the radiative decay rate, 25 times increase in the PL intensity, and 2 times increase in the quantum efficiency are demonstrated. Finally, the prospects for achieving Purcell-enhanced lasing using Er-doped nanoring cavities are examined and this work is discussed with respect to similar theoretical and experimental work in the field.

5.2 Device Geometry and Fabrication

Plasmonic ring nanocavities consist of a thin cylindrical ring of Erbium doped silicon dioxide, Er:SiO_2, embedded in a thick layer of silver forming a small dielectric gap between two metallic interfaces. A schematic of the ring nanocavities is shown in Figure 5·1 (a). The ring nanocavities are defined by their inner diameter, d (nm), the thickness of the dielectric gap region, t (nm), and the height, h (nm). The thickness and the diameter will be varied in this study, while the height will be kept fixed at 180nm.

Ring nanocavities are fabricated using radio frequency sputtering, electron beam

lithography, metal evaporation and reactive ion etching, all CMOS-compatible processes. Square SiO_2 chips of 1.5cm side length are cut from a circular wafer using a dicing saw and then cleaned in Piranha acid solution (3 H_2SO_4 : 1 H_2O_2) for 2 minutes and rinsed in deionized water. Next, 180nm of Er:SiO_2 is deposited on the chips by magnetron co-sputtering in an Ar/O_2 environment. A layer of Poly(methyl methacrylate) (PMMA) is then spin coated on the sample at 2000rpm and baked at 180C for 75 sec to remove any remaining solvent. The 180nm thick layer of PMMA acts as a positive tone electron beam resist when exposed to the proper dosage of charge at 30kV in a scanning electron microscope. A dosage check is performed where the same pattern is written at several dosages. The patterns are then examined under SEM to determine which dosage produces the proper size pattern. To define the nanorings a pattern of annular rings is produced in a CAD editor with varying diameter (d) and thickness (t) which are repeated in a hexagonal array with $1.5\mu m$ pitch. This spacing of nanoring devices is chosen such that nanocavities will be optically isolated on the chip. Next, exposed areas are developed in methyl isobutyl ketone (MIBK) diluted in isopropyl alcohol (IPA) (1 MIBK : 3 IPA). A thin layer of Cr (15nm) is then deposited on the sample using electron beam evaporation and lift-off in acetone is used to remove the remaining PMMA and excess Cr. The remaining Cr ring pattern is transferred to the Er:SiO_2 by reactive ion etching using a CF_4/H_2 chemistry. The relative gas flow rates, pressure and power during the etch are chosen (based on previous characterization of the tool) to achieve vertical sidewalls during the etch process. Next, the rings are thinned by isotropic wet etching in dilute buffered oxide etch (BOE) (1 BOE : 20 H_2O) to remove approximately 35nm of Er:SiO_2 making the rings slightly taller and significantly thinner. Such a dilute etch solution is used as the slow etch rate (25nm/min) allows for greater control of the total etch depth. Next any remaining Cr is removed in commercially available Cr etchant and the sample is annealed at 900C for 1 hour. Finally, a thick layer of Ag (300nm)

is deposited on the sample by electron beam evaporation to bury the annular rings in metal. This deposition step simultaneously creates the outer and inner metallic surfaces which form the ring nanocavity. Figure 5·1 (b-d) shows scanning electron micrographs (SEMs) of the nano-rings before metallization with d = 400nm and t = 50nm, 75nm and 105nm respectively. A thin layer of gold is visible in the SEM which is used to prevent charging of the sample and removed after imaging.

This fabrication process has several distinct advantages over the high aspect ratio design of the previous chapter and other designs of planar plasmonic structures. The first advantage is that all the active material is inside the nanocavity and should experience a strong change in the PDOS. In devices where planar arrays of particle are deposited on active materials, typically only a small amount of the active volume will be in a region with high field confinement, causing, on average, a smaller increase in light-matter coupling. Another advantage of this fabrication method comes from the isotropic thinning on the nanocavity before the Ag layer is deposited. In this geometry the primary limiting factor of the electric field confinement (and overall device performance) is the thickness of the dielectric gap region. A thinner gap region will lead to significantly stronger field confinement and radiative rate enhancement. Using electron beam lithography the smallest dielectric gap region that can be reliably fabricated is about 100nm, however when an isotropic wet etch is used to thin the sample further the gap thickness can reliably be reduced to about 50nm. In contrast to the fabrication method presented in the previous chapter, the lack of high aspect ratio structures makes this process more reliable. Finally, the roughness of metal layers deposited by evaporation can limit the quality of plasmons which form on the surface. Typically the top surface of an evaporated film will be rough but the bottom surface (in contact with the substrate) will have a roughness that is determined by the roughness of the substrate. In this case the dielectric surface is fairly smooth so the metal surface which

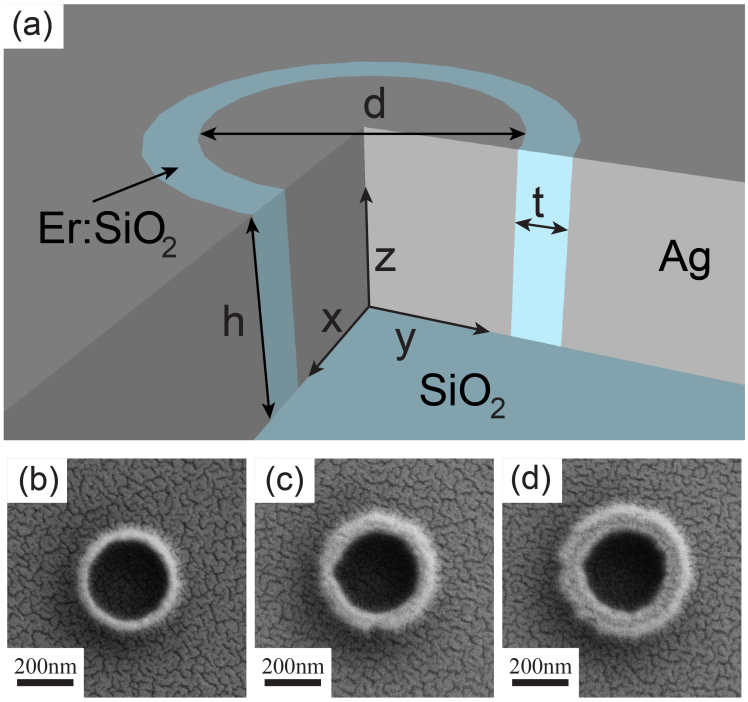

Figure 5·1: (a) Schematic of the ring nanocavity with cutout taken for demonstration purposes which consists of a Er:SiO_2 cylindrical ring buried in Ag. The rings have a height, h = 180nm, an inner diameter of d (nm) and a thickness t (nm). (b-d) SEMs of the rings before metallization with d = 390nm and t = 50nm, 75nm and 105nm respectively.

forms the nanocavity will be quite smooth as well, leading to device performance which more closely matches the ideal case(Nagpal et al., 2009).

5.3 Gap Plasmons and PDOS Enhancement

In this section, a theoretical study of 3D plasmonic ring nanocavities is presented using the FDTD method in order to properly design nanocavities for operation at 1.5μm and quantitatively examine experimental data. In such geometries, the strong confinement of the electric field vector in the subwavelength dielectric regions is caused by the coupling of plasmon modes supported on the outer and inner metallic interfaces, resulting in a large modification of the PDOS(Lawrence and Dal Negro, 2010). In

Figure 5·2 (a) the calculated PDOS (blue) (normalized to the free space value, called relative PDOS) for a dipole source positioned at the center of the dielectric region $(x, y, z = 220\text{nm}, 0\text{nm}, 90\text{nm})$ averaged over dipole orientation (see schematics in Figure 5·1 (a)). Multiple peaks of enhanced PDOS appear at wavelengths of $\lambda_1 = 1120\text{nm}$, $\lambda_2 = 1525\text{nm}$ and $\lambda_3 = 2020\text{nm}$, consistently with previous analytical predictions for two-dimensional structures. The PDOS modifications are obtained by sampling the power emitted by a dipole source positioned inside the nanocavity and by dividing it to the power emitted in free space(Novotny and Hecht, 2006). By integrating the flux of the Poynting vector over a surface enclosing the entire device we the rate of energy flow away from the structure (radiated power) is calculated and plotted in Figure 5·2 (a) (red) normalized to that of an equivalent source in free space. Due to energy conservation, the difference between the total emitted power and the radiated power gives the absorption rate within the device, which is plotted in Figure 5·2 (a) (green) once again normalized to the emitted power of a source in free space. These results demonstrate that even in close proximity to a metallic surface, most of the power is still radiated away from the ring nanocavity device.

Within the nanocavity the emitted radiation couples to deep subwavelength localized gap plasmon modes. The spatial distribution of this radiation is provided by the calculations of the normalized electric field amplitude at the wavelengths λ_1-λ_3, shown in Figure 5·2 (c-e) in the XY horizontal plane 20nm above the Ag/SiO_2 interface, excited by an X oriented dipole source in the same location as Figure 5·2 (a). In Figure 5·2 (c-e) field minima and maxima show the excitation of the m=2,1,0 azimuthal orders, respectively, where the optical energy is strongly confined within the nanoscale dielectric gap region. To engineer the radiation enhancement in plasmonic ring nanocavities the PDOS for devices with different active region thickness over a wide spectral range is calculated and shown in Figure 5·2 (b). For gap sizes ranging from 100nm to 50nm

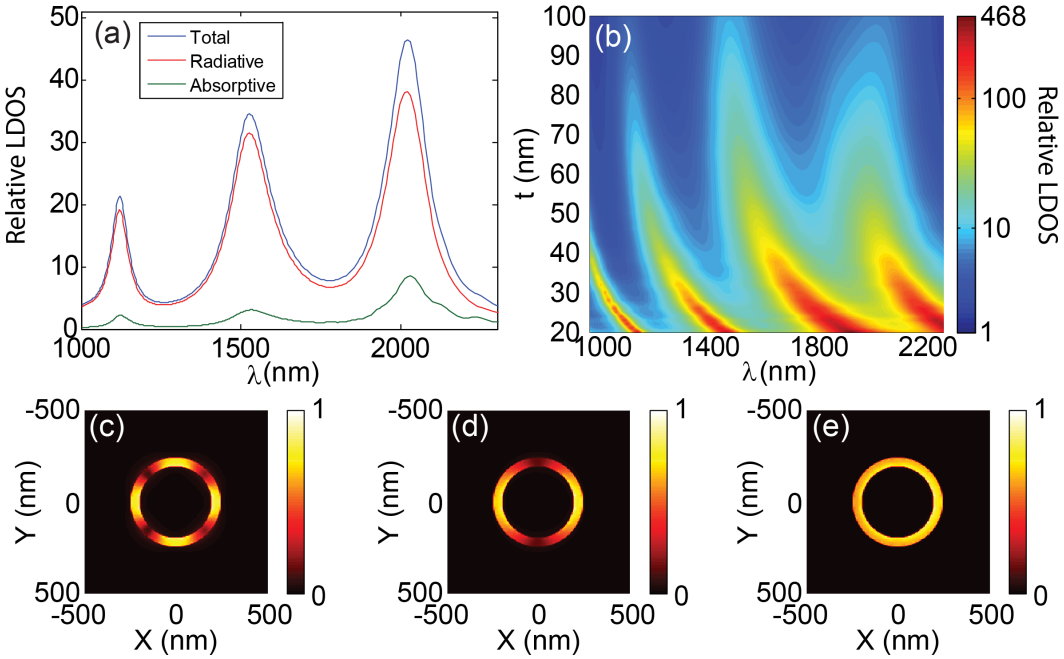

Figure 5·2: (a) Relative PDOS, calculated using FDTD method, in the center of the dielectric gap of a ring nanocavity, $(x, y, z = 220\text{nm}, 0\text{nm}, 90\text{nm})$, with d = 390nm and t = 50nm, averaged over dipole orientations. The total rate enhancement (ie. Relative LDOS) is plotted in blue, the radiative rate enhancement is plotted in red and the absorption rate enhancement is plotted in green. (b) Relative PDOS in the center of the dielectric gap for ring nanocavities as a function of wavelength and gap thickness, t (nm). (c-e) Normalized electric field amplitude from an X-oriented dipole source located in the center of the dielectric gap at $(x, y, z = 220\text{nm}, 0\text{nm}, 90\text{nm})$, plotted in the XY plane 20nm above the Ag/SiO_2 interface at wavelengths of 1120nm, 1525nm and 2020nm respectively, with d = 390nm and t = 50nm.

the energy of the resonance remains roughly the same while its intensity increases due to confinement of field within a smaller region. As the gap shrinks further from 50nm to 20nm the PDOS increases dramatically, reaching a maximum PDOS exceeding 400 times that of free space, while the resonance wavelength begins to red-shift due to the increased coupling strength of the plasmon modes supported by the inner and outer metallic interfaces(Lawrence and Dal Negro, 2010; Hao et al., 2009).

5.4 Optical Characterization

5.4.1 Reflection and Local Field Enhancement

In order to experimentally investigate the tunability of the plasmonic resonances of the fabricated ring nanocavities over a large spectral range passive reflection measurements of devices with varying diameter (d) and dielectric gap thickness (t) are performed. Reflection spectra are compared with FDTD calculated spectra of the resonant electric field intensity in the dielectric gap regions of the nanocavities. All the reflection spectra are measured using normally incident white light focused with a 50X (NA=.75) objective. The collected light is focused into a fiber-coupled spectrometer and the reflection spectra are normalized by the the measured response of a homogeneous silver surface used as a reference. Figure 5·3 (a) (top) shows the measured reflection from ring nanocavities of increasing diameter (blue - 230nm, red - 310nm, green - 390nm and yellow - 470nm) all with a dielectric gap thickness of t = 50nm. Figure 5·3 (b) (top) shows the averaged near-field intensity within the dielectric gap region for nanocavities of increasing diameter, d, matching those in Figure 5·3 (a), where evanescent fields in the metal lead to absorption in the cavity causing dips in the reflection. Consistently with previous studies(Lawrence and Dal Negro, 2010; Hao et al., 2009), as the ring diameter increases the peak enhancement of the near-field and minimum of reflection red-shift. Figure 5·3 (a) (middle, bottom) shows the reflection and Figure 5·3 (b) (middle, bottom) the near-field enhancement spectra of nanocavities with a dielectric gap thicknesses of 75nm and 105nm, respectively. Similar trends with varying nanocavity diameter are observed irrespective of the dielectric gap thickness. Moreover, a blue-shift of all the peaks is observed as the thickness of the dielectric gap region increases, due to a reduction in the coupling strength of gap plasmon modes between the outer and inner metallic surface(Lawrence and Dal Negro, 2010; Hao et al., 2009). The maximum intensity inside the cavities is strongly dependent on the size of the gap, increasing with

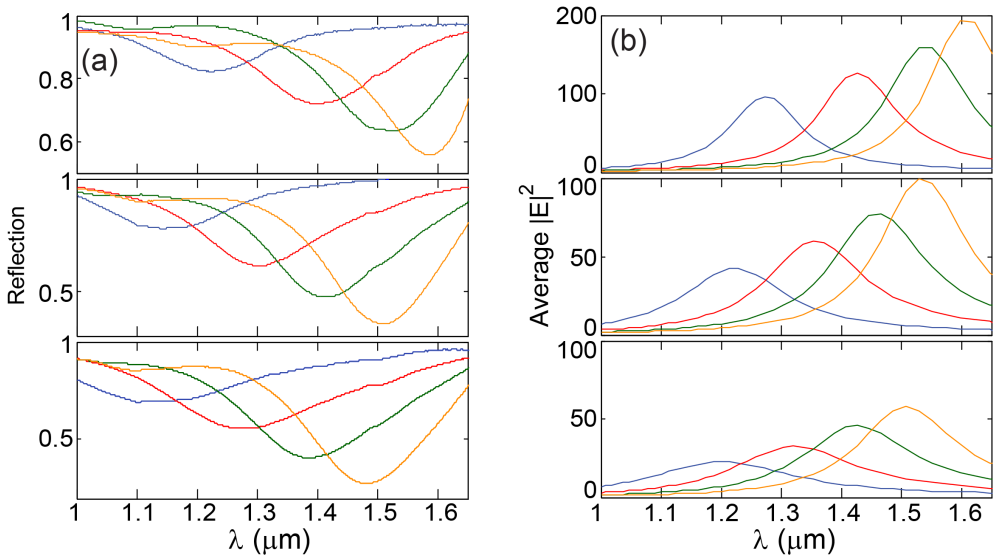

Figure 5·3: (a) Measured reflection for ring nanocavities of varying diameter and dielectric gap thickness. (b) Average electric field intensity in the dielectric gap region, calculated with FDTD method, for ring nanocavities excited by a plane wave with unity intensity. In both (a,b) ring nanocavity gap thickness t is 50nm (top), 75nm (middle) and 105nm (bottom). The colors correspond to inner diameters, d, of 230nm (blue), 310nm (red), 390nm (green) and 470nm (yellow).

smaller gap sizes and reaching a maximum of almost 200 times for the 50nm gap thickness, 100 times for 75nm gap thickness and 60 times for the 105nm gap thickness. The controllable intensity of the electric fields deeply localized within the nanocavities are also very appealing for optical sensing, absorption enhancement, or the enhancement of non-linear optical properties of dielectric materials placed inside the nano-gap regions.

5.4.2 Photoluminescence Intensity

Next, the active optical properties of plasmonic ring nanocavities are investigated. Steady state photoluminescence measurements are made for the reference and nanocavity samples where Er ions are resonantly excited using quasi steady-state pumping at 980nm using a Ti:Sapphire laser with 150fs pulses at 80MHz. Since the excitation life-

time of Er ions is in the ms regime there will not be time for a significant amount of the excited electron population to decay between optical pulses and a steady state population should build up in the atomic system as if a constant excitation photon flux was used. Pumping at 980nm causes electrons to move from the $^4I_{15/2}$ to the $^4I_{11/2}$ atomic energy levels. The $^4I_{11/2}$ state is short lived and electrons quickly decay non-radiatively to the $^4I_{13/2}$ state where they can finally return to the $^4I_{15/2}$ energy state through the production of photons at $1.54\mu m$ (or decay non-radiatively). The excitation laser is focused weakly on the sample to a spot size of about $50\mu m$ and the light produced at $1.54\mu m$ is collected with a 50X (NA = 0.75) objective and detected using a monochromator and InP/InGaAs photomultiplier tube (Hamamatsu R5509-73). By comparing the steady state PL signal for the reference sample and nanocavities under identical excitation and collection conditions the enhancement of the PL can be measured. Since the volume of emitting material, and hence number of emitters, is significantly different for the reference and nanocavity samples a correction factor must be introduced to compensate. In Figure 5·4 the normalized intensity enhancement is plotted for ring nanocavities of varying cavity thickness, t, and diameter, d and a maximum emission enhancement of 24 times is achieved. For each cavity thickness there is an optimal cavity diameter for emission enhancement, which corresponds to the cavity diameter causing spectral overlap of the plasmon mode with the emission wavelength of Er ions. As the cavity thickness decreases from 105nm to 75nm the emission enhancement increases, consistent with the expectation of stronger field confinement in smaller gap thickness cavities. As the thickness decreases further from 75nm to 50nm the maximum emission enhancement value stays roughly the same. Though stronger radiation rate enhancement is expected at smaller gap sizes, stronger increases to the non-radiative rate is also expected because of the increased proximity of Er ions to the metal surfaces in the cavity. These two changes can offset each other. Further intensity enhancement could

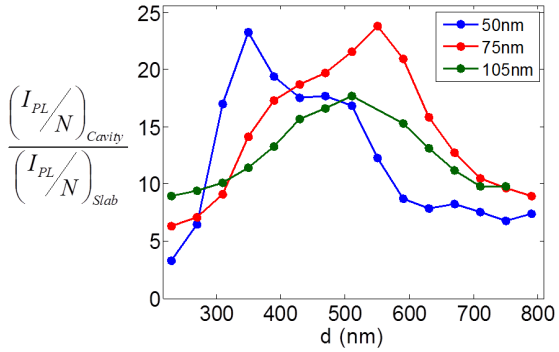

Figure 5·4: Photoluminescence intensity enhancement for ring nanocavities of varying thickness and diameter. The measured intensity is normalized by the measured PL intensity from a homogeneous slab of Er:SiO_2 and the number of Er ions for the cavities and reference material. Blue lines are for ring nanocavities with t = 50nm, red lines are for ring nanocavities with t = 75nm and green lines are for ring nanocavities with t = 105nm.

be realized by taking advantage of increased pumping efficiency due to increased local field intensity of the pump. Due to the radial polarization of plasmon modes, pumping with a radially polarized beam could be particularly effective at exciting plasmon modes. In the next section of this chapter, a thorough look at the PL decay dynamics will be provided using time resolved PL measurements.

5.4.3 Photoluminescence Decay Measurements

Time-resolved photoluminescence (PL) spectroscopy is used to investigate changes in the radiative decay rate caused by plasmon formation in ring nanocavities. The same optical setup is for time resolved and steady-state measurements with the excitation laser now switched at 11Hz by an electro-optic modulator (Conoptics 350-160). For the reference sample a single exponential Er^{3+} emission lifetime of $\tau_0 = 8.8ms$ is measured.

In order to quantitatively compare emission lifetimes of the reference sample and nanocavities, it is important to realize that the Er decay time in plasmonic cavities cannot be described by a single exponential relaxation process, because Er ions located

at different positions in the nanocavity experience different decay rates due to the spatial variations in both the PDOS and the non-radiative processes. The Er decay in non-homogeneous photonic-plasmonic environments can accurately be modeled by a stretched exponential function, which is the Laplace transform of a distribution of decay rates(Munechika et al., 2010; Kalkman et al., 2006). Following this approach, the measured photoluminescence decay data for the nanocavities are fit to a decay function with single and stretched exponential decay components, $I_{PL}(t) = A_1 e^{(\frac{t}{\tau_1})^\beta} + A_2 e^{\frac{t}{\tau_2}}$. For all measurements the stretched exponential decay term is the predominant component of the decay ($A_1 > A_2$). The lower intensity single exponential term has a lifetime τ_2 roughly equal to that of the unpatterned sample. The PL decay of the nanocavity samples is most accurately captured using the combination of a stretched and single exponential which describe the decay of Er ions coupled to and uncoupled from the nanocavity respectively. Based on the well-established stretched exponential theory(Lindsey and Patterson, 1980), an average Er decay time, $\langle\tau\rangle$, can be defined according to the formula:

$$\langle\tau\rangle = \frac{\tau}{\beta}\Gamma(\beta^{-1}) \tag{5.1}$$

where τ is the lifetime and β is the stretching parameter of the decay.

In the remainder of this chapter, the average decay time of Er ions will be used to compare the decay dynamics of different samples according to $\langle\Gamma\rangle \approx \frac{1}{\langle\tau\rangle}$.(Kalkman et al., 2006; Lindsey and Patterson, 1980) In Figure 5·5 (a) the PL decay data for the reference (black) and ring nanocavities of different thickness (colored) are plotted (points) along with the corresponding fits (lines). All the ring nanocavity devices feature a strongly decreased lifetime compared to the reference (black - $\tau_0 = 8.8ms$), with minimum average lifetimes of $\langle\tau_{50nm}\rangle = 0.44$ms, $\langle\tau_{75nm}\rangle = 0.81$ms and $\langle\tau_{105nm}\rangle = 1.19$ms corresponding to different thicknesses of the cavity. In the inset of Figure 5·5 (a) shows the measured Er emission spectrum from a nanocavity with a 50nm gap thickness and

390nm diameter, the same device corresponding to the blue-colored PL decay data. The decay fit constants for the nanocavity data in Figure 5·5 (a) are shown in Table 5.4.3.

Cavity Thickness	Inner Diameter	τ_1	β	$\langle\tau\rangle$
50nm	390nm	0.41ms	0.85	0.44ms
75nm	510nm	0.76ms	0.89	0.81ms
105nm	510nm	1.15ms	0.92	1.19ms

Table 5.1: Decay Parameters for Figure 5·5a

In Figure 5·5 (b) the experimentally measured (total) decay rate enhancement values (defined with respect to the decay rate of the reference sample) for a number of devices with different cavity thickness (t) and diameter (d) are shown (filled circles). The measured enhancement of the decay rate is stronger in nanocavities with small dielectric gap thickness consistent with the stronger confinement of the electric field in gap plasmon modes. Is is clear by comparing the decay rate enhancement data, the experimental reflection spectra, and the PDOS calculations that the maximum decay rate enhancement occurs when the gap plasmon resonance overlaps the peak of the Er emission spectrum. A detailed discussion of the quantification of the radiative and non-radiative contributions to the enhancement of the total decay rate is provided with detailed data analysis.

The modified total decay rate in the ring nanocavity can be expressed as $\Gamma_{t-cav} = \Gamma_{r-cav} + \Gamma_{ab-cav} + \Gamma_{nr-metal}$(Novotny and Hecht, 2006), where Γ_{r-cav} is the rate at which photons radiate to the far-field from from the nanocavity, Γ_{ab-cav} is the rate at which photons are absorbed by the metal in the cavity and $\Gamma_{nr-metal}$ is the non-radiative transition rate of Er ions that can be modified by the coupling with the plasmonic nanocavity. According to the Fermi golden rule, the rate of photon emission/absorption processes is proportional to the PDOS, which is modified by the nanocavity(Novotny and Hecht, 2006). Using FDTD simulations we can rigorously calculate the PDOS of

the devices by integrating over the spontaneous emission bandwidth of the material.

In order to compare the calculated and the experimentally measured cavity-induced modifications of the total spontaneous emission lifetime both radiative and non-radiative contributions of the decay must be included. The change in the radiative processes is calculated with FDTD simulations accounting for both photons propagating to the far-field and photons absorbed in the metal of the cavity and defined as η_{t-cav}. All other non-radiative decay processes, some of which are intrinsic to the material and some which may have been introduced during processing, are taken into account by a term defined as $\eta_{nr-metal}$. The total expected decay rate is given by $\eta_{t-cav}\Gamma_{r0} + \eta_{nr-metal}\Gamma_{nr0}$ where $\eta_{nr-metal}$ is used as single fitting parameter for all the data, causing only a vertical shift. Combining the well-known radiative lifetime of Er:SiO_2 of $\tau_{r0} = 20ms$(Creatore et al., 2009; Becker et al., 1999) with the measured total decay time, $\tau_0 = 8.8ms$, provides the non-radiative lifetime $\tau_{nr0} = 15.9ms$ and the quantum efficiency, $q_0 = .44$. This value of quantum efficiency should only be treated as an upper bound as some variation of τ_{r0} exists in the literature. Figure 5·5 (b) (dotted lines) shows the calculated decay rate enhancement with best fit values of $\eta_{nr-metal} = 6.34, 7.32$ and 9.84 for structures with 105nm, 75nm and 50nm gap thicknesses respectively, corresponding well to the experimental data. This data fitting only effects the open circle points plotted in Figure 5·5 (b) and the calculated change in the quantum efficiency in Figure 5·6 (d).

5.4.4 Quantification of Radiative Rate and Quantum Efficiency Enhancement

The enhancement of the radiative decay rate of Er ions in the nanocavity can be quantified in the weak excitation regime, which well corresponds to the experimental conditions (as independently verified by the linearity of the Er emission intensity with respect to the pumping photon flux). In this regime, the following relation holds $\sigma\phi << \Gamma_t$, where ϕ is the pumping photon flux, σ is the absorption cross section of Er, and the PL intensity,

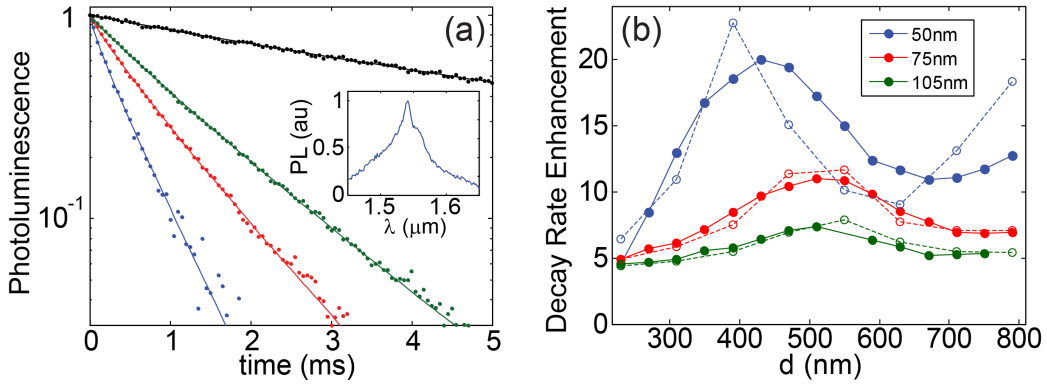

Figure 5·5: (a) Photoluminescence decay measurements for ring nanocavities (colored) and reference material (black). (b) Measured (filled circles) and calculated (open circles, including fit of non-radiative decay) total spontaneous emission rate enhancement of ring nanocavities of increasing diameter, d (nm). (a,b) Blue lines are for ring nanocavities with t = 50nm, red lines are for ring nanocavities with t = 75nm and green lines are for ring nanocavities with t = 105nm. In (a) the diameter of nanocavities is 390nm (blue) and 510nm (red, green) respectively. The inset in (a) is the PL spectrum of a ring nanocavity of thickness 50nm and diameter 390nm.

I_{PL}, can be expressed as:

$$I_{PL} \propto \eta_{ext} N \sigma \phi \frac{\Gamma_r}{\Gamma_t}. \tag{5.2}$$

By considering the ratio of the PL intensity measured for the ring nanocavities and for the reference material, under identical excitation conditions, the change in the radiative decay rate of Er induced by the cavities is measured.(Biteen et al., 2005; Munechika et al., 2010; Matsuda et al., 2008) The enhancement of the radiative decay rate is given by:

$$\frac{\Gamma_{r-cav}}{\Gamma_{r-ref}} = \frac{I_{PL-cav}}{I_{PL-ref}} \frac{\eta_{ext-ref}}{\eta_{ext-cav}} \frac{N_{ref}}{N_{cav}} \frac{\sigma_{ref}}{\sigma_{cav}} \frac{\Gamma_{t-cav}}{\Gamma_{t-ref}} \tag{5.3}$$

where $\eta_{ext-ref,cav}$ is the light extraction efficiency, $\sigma_{ref,cav}$ is the absorption cross-section and $N_{ref,cav}$ are the numbers of active Er atoms in the reference sample and in the ring nanocavities, respectively. The factor $\frac{N_{ref}}{N_{cav}}$ is accurately estimated from the volume ratio of the ring nanocavities to that of the reference material. In addition to the measured

PL intensity the collection efficiency of light must be considered in Equation 5.3 as it varies significantly between the reference sample and the nanocavities.

The extraction efficiency of the reference sample is calculated using geometric optics and considering emission from an isotropic point source in a slab of SiO_2. The extraction efficiency, η_{ext}, is given by,

$$\eta_{ext} = \frac{\int_0^{2\pi} \int_0^{\theta_{NA}} sin(\theta) d\theta d\phi}{4\pi} \tag{5.4}$$

Where θ_{NA} is the maximum collection angle, which is determined by the numerical aperture of the objective (NA = .75). Using $\theta_{NA} = sin^{-1}(\frac{NA}{n_{SiO_2}})$ we find η_{ext} is given by,

$$\eta_{ext} = \frac{1}{2}\left(1 - \frac{\sqrt{n_{SiO_2}^2 - NA^2}}{n_{SiO_2}}\right) \tag{5.5}$$

which for this experiment is equal to 7.2%.

While a simple geometric optics calculation is sufficient to estimate the light extraction efficiency for the reference sample of Er ions embedded in an SiO_2 film, numerical FDTD calculations must be utilized for the ring nanocavities. The estimation of the light extraction efficiency from ring nanocavities can be performed by calculating the flux of the Poynting vector considering a solid angle determined by the NA of the experimental collection optics and by comparing it with the calculated flux of the Poynting vector across a surface enclosing the device. By following this procedure, the percentage of light collected at 1.54μm is found to vary between 39% and 76% depending on the cavity size, and features a maximum when the cavity resonance overlaps with the emission wavelength of Er. The pumping efficiency factor $\frac{\sigma_{ref}}{\sigma_{cav}}$, is also different for the nanocavities and the reference sample, and can be calculated using FDTD simulations by exciting the ring nanocavity with a plane wave source at 0.98 μm and measuring the average electric field intensity inside the cavity. Experimentally, similar trends can be

achieved by comparing the reflectivity data of devices and the reference sample at the pumping wavelength.

Figure 5·6 (a) shows the radiative emission rate for ring nanocavities of different diameter (d), and thickness (t), evaluated according to Equation 5.3. The maximum radiative rate enhancement increases with decreasing cavity thickness and is maximized when the cavity resonance overlaps with the peak of the Er emission spectrum, similarly to the total emission rate. FDTD calculations of the radiative rate enhancement are plotted in Figure 5·6 (c). By comparing the results of Figure 5·6 (a) and Figure 5·6 (c) similar trends are found of decay rate enhancement with nanocavity diameter for all cavity thicknesses. Additionally, both calculations and experiments show an increase in the radiative decay rate with decreasing gap thickness, demonstrating a 25-times increase of the radiative emission rate of Er in the optimal nanocavity geometry. There is some discrepancy between the measured and calculated radiation rate enhancement, especially at larger cavity diameters for the smallest cavity thickness. In these nanocavities, FDTD simulations suggest that a quadrupolar mode (as shown in Figure 5·2 (c)) should spectrally overlap with the Er emission and cause a change in the radiative rate. This change in radiative rate is not observed experimentally most likely due to fabrication imperfections that affect the formation of higher order modes more strongly.

Using Equation 5.3 the change in the Er quantum efficiency induced by the ring nanocavity can be determined, which is given by:

$$\frac{q_{cav}}{q_{ref}} = \frac{I_{PL-cav}}{I_{PL-ref}} \frac{\eta_{ext-ref}}{\eta_{ext-cav}} \frac{N_{ref}}{N_{cav}} \frac{\sigma_{ref}}{\sigma_{cav}}. \tag{5.6}$$

Figure 5·6 (b) shows the quantum efficiency enhancement caused by the nanocavities according to Equation 5.6. By using the quantum efficiency of the reference material, the FDTD calculated radiative decay rate and the non-radiative decay rate (obtained from experimental data fitting of the total spontaneous decay rate) the expected quantum

efficiency enhancement is calculated and plotted in Figure 5·6 (d). By comparing the quantum efficiency enhancement in Figure 5·6 (b) with the calculated enhancement, consistent trends are seen for a given cavity thickness as the cavity diameter is increased. Moreover, when comparing the results of Figure 5·6 (a,c) to Figure 5·6 (b,d) for a single cavity thickness, an increase in the quantum efficiency corresponds to an increase in the radiation rate. Finally, while the smallest cavity thickness provides the largest increase in the radiation rate it does not show the largest quantum efficiency, most likely due to increased non-radiative losses originating from the closer proximity of Er ions to the metallic surface.

5.5 Purcell Enhanced Lasing

This section provides a quantitative perspective on the potential to achieve laser action using Er-doped SiO_2 as an active material inside Si-compatible plasmonic ring nanocavities. The engineering of Si-based nanoscale optical emitters and lasers could potentially enable inexpensive on-chip optical components for high-density information processing and sensing applications (i.e., lab-on-a-chip) that are fully compatible with Si microelectronics technology.

In general, the gain threshold for lasing is reached in an optical cavity when the cavity gain, γ_c, exceeds the cavity loss, $\alpha_c = \frac{2\pi n}{\lambda Q}$. The optical gain in a material, γ_m, is typically limited by the maximum achievable population inversion of the light emitting atoms. When the radiation is confined within deep-subwavelength volumes, the significant Purcell enhancement of the spontaneous emission rate increases the stimulated emission rate, leading to the possibility of a large cavity gain, given by $\gamma_c = F_p\gamma_m$.(Ma et al., 2013; Vahala, 2003) The gain threshold is met when $\frac{\gamma_c}{\alpha_c} > 1$, in large cavity lasers where $F_p = 1$, $\frac{\gamma_c}{\alpha_c} \propto Q$ since γ_c is independent of Q. On the other hand, in small cavity volume resonators, when the spontaneous emission bandwidth of a material $\delta\lambda_m$ is less than the

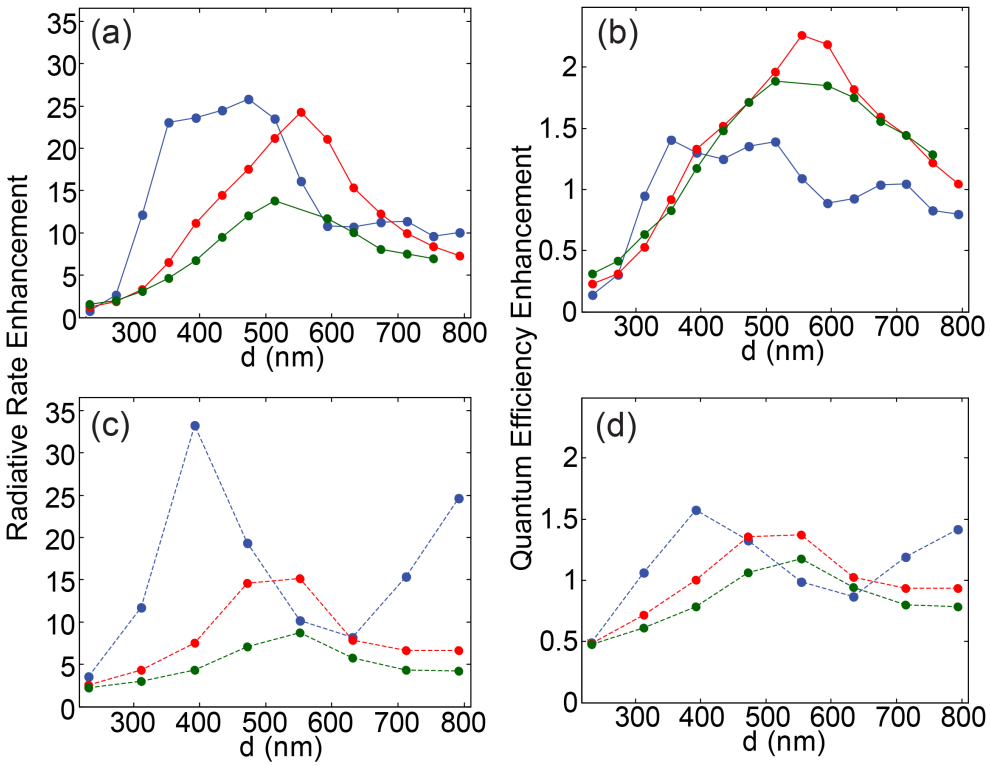

Figure 5·6: (a) Radiative rate enhancement for ring nanocavities of increasing diameter, d (nm), calculated according to Equation 5.3. (b) Quantum efficiency enhancement for ring nanocavities of increasing diameter, d (nm), calculated according to Equation 5.6. (c) Calculated radiative rate enhancement for ring nanocavities of increasing diameter, d (nm). (d) Calculated quantum efficiency enhancement for ring nanocavities of increasing diameter, d (nm). (a-d) Blue lines are for ring nanocavities with t = 50nm, red lines are for ring nanocavities with t = 75nm and green lines are for ring nanocavities with t = 105nm.

cavity linewidth $\delta\lambda_{cav}$, the Purcell enhancement factor can be expressed(Purcell, 1946) by $F_p = \frac{3}{4\pi^2}\left(\frac{\lambda_c}{n}\right)^3\left(\frac{Q}{V}\right)$ and the gain threshold scales according to $\frac{\gamma_c}{\alpha_c} \propto \frac{Q^2}{V}$. However, as Q is increased the condition $\delta\lambda_m < \delta\lambda_{cav}$ will be violated for most materials and a more rigorous definition of the Purcell factor is therefore necessary.

More generally, the Purcell factor is given by the ratio of the spontaneous emission rate, R_{sp}, in the cavity to that of free space. The rate of spontaneous emission can be expressed as:(Suhr et al., 2010; Coldren and Corzine, 1995)

$$R_{sp} = \int\int A_{21}\rho_{el}(E)\rho_{op}(h\nu)L(E-h\nu)dh\nu dE \tag{5.7}$$

where $\rho_{el}(E)$ is the electronic density of states, A_{21} is the Einstein spontaneous emission coefficient, $\rho_{op}(h\nu)$ is the photonic density of states and $L(E-h\nu)$ is the lineshape function due to homogeneous broadening of the emitter. When $\rho_{op}(h\nu)$ does not strongly depend on frequency (i.e., free space) the spontaneous emission lineshape is proportional to $\rho_{el}(E)\times L(E-h\nu)$. In the limit of $\rho_{el}(E)\times L(E-h\nu) \rightarrow \delta(E-h\nu_c)$, where $h\nu_c$ is the resonance frequency of the cavity Equation 5.7 will be proportional to $\rho_{op}(h\nu)$ at the cavity central frequency and the Purcell factor can simply be expressed as the ratio of the density of states at resonance to that of free space, resulting in the normal definition of Purcell Factor, $F_p = \frac{3}{4\pi^2}\left(\frac{\lambda_c}{n}\right)^3\left(\frac{Q}{V}\right)$. However, when the bandwidth of the spontaneous emission becomes appreciable, F_p must be obtained by integrating the photonic density of states over the spontaneous emission lineshape, as in Equation 5.7. Using the experimentally measured spontaneous emission spectrum of the Er:SiO_2 material, the free-space photonic density of states $\rho_{fs}(h\nu) = \frac{8\pi n^3\nu^2}{c^3}$ and a Lorentzian cavity density of states, the Purcell factor can be rigorously calculated as a function of the cavity Q factor and volume. We find numerically that when the Q factor is increased beyond ≈ 50 such that $\delta\lambda_m > \delta\lambda_{cav}$ the Purcell factor saturates and the scaling of the gain threshold becomes $\frac{\gamma_c}{\alpha_c} \propto \frac{Q}{V}$.

Using the more rigorous definition spontaneous emission rate enhancement, the role of the Purcell effect on the gain threshold of plasmonic ring nanocavities with Er-doped SiO_2 as an active medium can be studied. Figure 5·7 (a) shows the effect of Purcell-enhanced stimulated emission rate on the gain threshold $\frac{\gamma_c}{\alpha_c}$ for resonators of different volumes. The calculations use a constant material gain of $\gamma_m \approx 2cm^{-1}$, consistent with studies of optical gain in Er:SiO_2(Kippenberg et al., 2006). The black line shows the evolution of the cavity gain threshold when the Purcell effect is absent ($F_p = 1$), for which a cavity quality factor $Q = 3 \times 10^4$ would be needed in order to achieve lasing. The colored lines show the effect of Purcell enhanced stimulated emission for different cavity volumes, blue - V = $0.01\left(\frac{\lambda}{n}\right)^3$ and red - V = $0.1\left(\frac{\lambda}{n}\right)^3$. It is very interesting to note that the scaling of the threshold with Q depends markedly on the cavity volume. In fact, while for $F_p = 1$ we have $\frac{\gamma_c}{\alpha_c} \propto Q$, in the case of small cavity sizes and at low Q factors we see that $\frac{\gamma_c}{\alpha_c} \propto \frac{Q^2}{V}$. When the Q factor increases in nanocavities the scaling changes to $\frac{\gamma_c}{\alpha_c} \propto \frac{Q}{V}$ due to the saturation of F_p. The dotted lines show the behavior of $\frac{\gamma_c}{\alpha_c}$ without the saturation of F_p, which leads to dramatic overestimation of $\frac{\gamma_c}{\alpha_c}$ values in the high Q regime.

This analysis has demonstrated that for materials with broadband emission, high Purcell factors cannot be achieved simply by increasing the resonator Q factor and shrinking the cavity volume becomes essential. In the case of Er, it is shown that the Q factor needed to achieve lasing in plasmonic ring nanocavities is strongly dependent on the volume of the ring. For a volume of V = $0.1\left(\frac{\lambda}{n}\right)^3$ a Q factor of 880 is needed to achieve lasing while for a volume of V = $0.01\left(\frac{\lambda}{n}\right)^3$ a Q factor of 123 would suffice. Though this analysis has been performed specifically targeting the Er emission, it is generally applicable to alternative material systems for the engineering of plasmonic nanolasers.

Figure 5·7 (b) shows $\frac{\gamma_c}{\alpha_c}$ as a function of both Q and the cavity volume for the Pur-

cell enhanced stimulated emission of Er. The vertical black line in the figure indicates the gain threshold region in the Q-V calculated parameter space. Devices with Q-V parameters falling in the area to the right of this line have overcome the gain threshold condition for lasing. The horizontal black line indicates the Q-V region where Purcell enhancement is no longer a factor, devices above this line have $F_p = 1$. The numbers placed on the phase plot indicate various plasmonic and photonic optical cavities which have been explored. Table 5.5 contains a description of each device, indicates if the work is theoretical or experimental and whether it has been demonstrated with an active or passive medium. Number 1 on the plot shows the work on plasmonic ring nanocavities in this thesis. Numbers 2-5 reference similar cylindrical plasmonic nanocavities studied both theoretically and experimentally with both passive and active materials. Of these numbers 3 and 5 come closest to the lasing threshold with number 3 surpassing the laser threshold, however this work is purely theoretical. Number 5 uses focused ion beam lithography to make extremely small volume nanocavities, however these devices are passive and filling the small cavity region with active material is very challenging. Numbers 6-8 demonstrate lasing in the IR in various nanocavity designs using III-V semiconductor materials. Number 6 employs a cylindrical MIM cavity similar to this work, number 7 uses an optical cavity coated with metal to increase field confinement and 8 uses an MIM waveguide. None of these three approaches have sufficiently small cavity size or high enough Q factor for Er based nanolasers. Numbers 9 and 10 demonstrate lasing in the visible, where 9 relies on plasmon polariton formation on a metal nanoparticle and 10 in an on chip micro-resonator with light confinement by total internal reflection. Number 9 is very close to the volume and Q factor needed for Er based lasing however this work uses solution based nanoparticles with are not suitable for on-chip integration. Numbers 11-13 are examples of active photonic nanocavities which incorporate Er. In number 11 lasing is demonstrated in a high Q micro-disk

cavity on a Si substrate, however coupling light to and from this type of resonator is challenging. Electrical injection is also not possible in suspended micro-disk cavities. In number 12 a photonic crystal cavity is used which has reduced mode size compared to the micro-disk structure, however insufficient Q factor to exhibit lasing. Number 13 employs a nano-beam resonator and should have sufficient Q factor and mode volume to achieve lasing use Er, with ideal material gain. In this work, Er:SiN_x is used to make the nanocavity and transparency is observed but not laser action.

Number	Description	λ	Citation
1	This Work	$1.55\mu m$	(Lawrence and Dal Negro, 2013)
2	Cylindrical plasmonic nanocavity	$1.5\mu m$	(Kroekenstoel et al., 2009)
3	Cylindrical plasmonic nanocavity	Various	(Vesseur et al., 2010)
4	Cylindrical plasmonic nanocavity	$700nm$	(Vesseur and Polman, 2011)
5	Cylindrical plasmonic nanocavity	$710nm$	(Melli et al., 2013)
6	Thresholdless Coaxial Nanolaser	$1.55\mu m$	(Khajavikhan et al., 2012)
7	Laser with metallic coating	$1.4\mu m$	(Hill et al., 2007)
8	MIM Plasmonic Waveguide Laser	$1.5\mu m$	(Hill et al., 2009)
9	SPASER	$525nm$	(Noginov et al., 2009)
10	CdS Plasmon Laser	$500nm$	(Ma et al., 2010)
11	Microdisk Resonator Laser	$1.55\mu m$	(Kippenberg et al., 2006)
12	ErSiN photonic crystal cavity	$1.55\mu m$	(Gong et al., 2010b)
13	Nanobeam resonator	$1.55\mu m$	(Gong et al., 2010a)

Table 5.2: Resonant Cavities in Figure 5·7 (b)

5.6 Conclusions

In conclusion, this chapter contains the design, fabrication and characterization of plasmonic ring nanocavities composed of Er:SiO_2 and silver. The excitation of gap plasmons creates deep subwavelength light confinement in cavities with volumes as small as $0.01\left(\frac{\lambda}{n}\right)^3$. The geometry of the cavity is varied to maximize the overlap of the cavity resonance with the spontaneous emission of Er and the total decay rate of Er atoms is

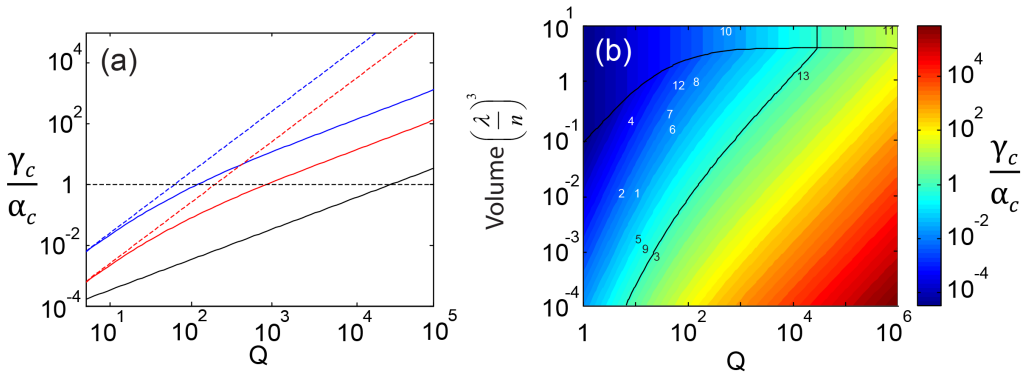

Figure 5·7: (a) Cavity gain/loss as a function of cavity Q factor with (colored) and without (black) Purcell enhanced stimulated emission using Er as a gain material, $\gamma_m = 2cm^{-1}$. The colored solid lines correctly account for the spontaneous emission bandwidth of Er in the calculation of the Purcell enhancement while the dotted lines show the result when saturation of the Purcell effect is ignored. Blue corresponds to a normalized cavity volume of 0.01 $\left(\frac{\lambda}{n}\right)^3$ and the Red corresponds to 0.1 $\left(\frac{\lambda}{n}\right)^3$. (b) Cavity gain/loss as a function of Q factor and volume accounting for stimulated emission enhancement in Er. The area to the left of the solid black vertical line indicates that the gain threshold has been surpassed. The area above the horizontal black line is the region where Purcell enhancement is no longer a factor ($F_p = 1$)

increased 20 times at room temperature. Through measurements of photoluminescence intensity, PL time-dynamics and full-vector FDTD modeling of the fabricated device structures the enhancement of the radiative decay rate is quantified in a number of nanocavity devices which demonstrate up to 25-times radiative rate enhancement and a doubling of the quantum efficiency. Finally, the possibility of achieving Purcell-enhanced lasing is studied and it is shown that plasmonic ring nanocavities are a promising platform for Er based subwavelength sources.

Chapter 6

Aperiodic Arrays of Active Nanopillars for Radiation Engineering

Reprinted (adapted) with permission from Lawrence, N., Trevino, J. and Dal Negro, L. *Aperiodic arrays of active nanopillars for radiation engineering*, Journal of Applied Physics, **111**, 113101 (2012), Copyright 2012 American Institute of Physics

6.1 Introduction

Semiconductor light emitting diodes (LEDs) have found numerous applications in display and general lighting technologies.(Steigerwald et al., 2002; Soref, 1993) However, one limitation to the overall efficiency of solid state LEDs is the low extraction efficiency associated to the trapping of radiation in the active device region by total internal reflection. For this reason, LEDs are often roughened or patterned in ways to increase the light extraction efficiency, such as with periodic diffraction gratings or photonic crystal structures.(Wierer et al., 2009; Fujii et al., 2004; Fan et al., 1997) However, since light is emitted isotropically from LEDs, structures for extraction should preferably be capable of interacting with light traveling in all azimuthal directions (omnidirectional structures).(Benisty et al., 2008; David et al., 2006; David et al., 2005) Though surface roughening fulfills this criterion, its random nature makes it difficult to be engineered. Moreover, random structures do not provide the opportunity to engineer emission patterns for directionality control.(Lai et al., 2009; Rattier et al., 2003) The issue of omnidirectional extraction in periodic photonic structures has been previously addressed

through the use of Archimedean lattices owing to their higher degree of local rotational symmetry as compared to traditional hexagonal patterns.(David et al., 2006; McGroddy et al., 2008; David et al., 2001)

In this chapter, novel nanostructures for omnidirectional extraction enhancement and the generation of isotropic emission profiles are proposed. This is achieved by engineering aperiodic structures that approach continuous rotational symmetry in reciprocal space.(Trevino et al., 2011) In particular, the light emitting behavior of active nanopillar arrays based on the periodic, Archimedean lattice (i.e., A7), Pinwheel tiling(Radin, 1994), and golden angle Vogel spiral (GA spiral)(Vogel, 1979; Mitchison, 1977) geometries are investigated. These deterministic array structures feature increasing degree of rotational symmetry in k-space, ranging from discrete spectra with pure rotational axes, such as for periodic and quasiperiodic crystals, to more diffuse spectra with continuous components as for amorphous systems. Moreover, differently from periodic and quasiperiodic arrays, Pinwheel and GA spiral arrays support circularly symmetric scattering rings in Fourier space entirely controlled by deterministic generation rules(Dal Negro and Boriskina, 2012). The use of aperiodic arrays provides the possibility of shaping the angular emission profile in ways that cannot presently be achieved using periodic or quasi-periodic photonic structures with discrete rotational symmetry. In particular, GA spirals give rise to azimuthally isotropic radiation patterns, which can be utilized for uniform illumination(Wu et al., 2009).

In order to demonstrate omnidirectional extraction and emission profile shaping of Er radiation with planar dielectric structures, a number of Er:SiN_x nanopillar arrays are fabricated using electron beam lithography and reactive ion etching. The design of the arrays is performed by a combination of Finite Difference Time Domain (FDTD) simulations and Bragg scattering theory(Wiesmann et al., 2009). FDTD simulations are used to optimize the individual nanopillar height for light extraction, while Bragg scattering

calculations are utilized to design the array parameters, including the nanopillar spacing and filling factor. Optical characterization is performed by photoluminescence (PL) spectroscopy that demonstrates a more than 10 times increase in extraction efficiency for optimized GA spiral arrays, in agreement with calculations. Moreover, angularly resolved PL measurements performed by directly imaging Er emission in the Fourier space demonstrate that Pinwheel and GA spiral arrays create diffuse and azimuthally isotropic emission patterns controlled by the array geometry. These results offer unique opportunities for the engineering of novel Si-based light emitting nanostructures with isotropic radiation on a Si platform.

6.2 Aperiodic Arrays for Light Extraction

In this section, design of periodic, Archimedean, Pinwheel and GA spiral arrays for light extraction enhancement at 1.55 μm is performed using FDTD simulations and Bragg scattering calculations. Though the focus of this section is designing aperiodic arrays of nanopillars a periodic array is included as a reference sample. The periodic array is a hexagonally closed packed array with direct space shown in Figure 6·1 (a) and Fourier space shown in Figure 6·1 (e). The Fourier space of a hexagonal lattice consists of a 6-fold symmetric pattern of discrete Bragg peaks. The Archimedean lattices investigated are A7 structures, which consist of hexagonal arrays of unit cells containing seven particles, also arranged in a hexagonal lattice(David et al., 2001). Archimedean structures are therefore periodic systems featuring well-defined Bragg peaks in their diffraction spectra (i.e., pure-point measure). Figure 6·1 (b,f) show the direct and reciprocal (i.e., diffraction) space for a representative A7 array of particles. Discrete Bragg peaks with hexagonal rotational symmetry can clearly be distinguished in the reciprocal Fourier space of the A7 structure. However, Figure 6·1 (f) also shows the presence of additional peaks in the Brillouin zone, resulting in a higher degree of local

rotational symmetry (i.e., not a global symmetry of the crystal) compared to standard hexagonal crystals.(David et al., 2001; Senechal, 1996) Due to the increased density of Bragg peaks in the first Brillouin, A7 structures have been studied in relation to the engineering of light extraction.(David et al., 2006; Wiesmann et al., 2009)

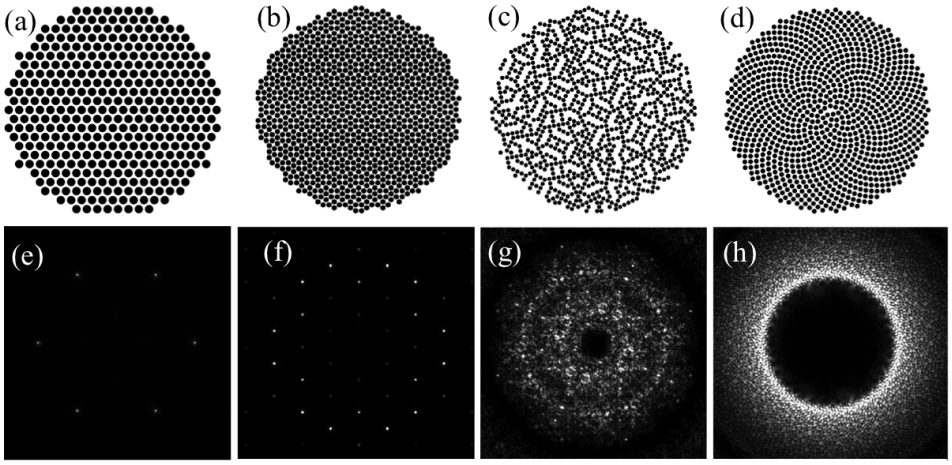

Figure 6·1: (a-d) Periodic, Archimedean (A7) lattice, Pinwheel tiling and GA spiral, respectively. (e-h) Discrete Fourier transforms (DFT) of Periodic, A7, Pinwheel, GA spiral arrays, respectively showing increasing degree of circular symmetry. The DC component arising in the DFT of the arrays has been eliminated.

In contrast, deterministic aperiodic structures, which support non-crystallographic point symmetries with rotational axes of arbitrary order(Senechal, 1996), have recently been studied for applications in photonics(Dal Negro and Boriskina, 2012). In particular, Pinwheel arrays have been discussed in the mathematical literature as examples of point patterns approaching, in the infinite-size limit, "infinity-fold" rotational symmetry, or k-space isotropy. These arrays are generated by performing decomposition and inflation operations on a prototile cell, which is a right triangle with sides of relative length 1,2 and $\sqrt{5}$. In the first step, the prototile is divided into five congruent copies and then new triangles are expanded to the size of the original triangle. Each of the

new triangles is decomposed in the same fashion and inflated again, leading to a complete tiling of the plane when these operations are repeated *ad-infinitum*(Radin, 1994). The resulting aperiodic tiling contains triangular elements, which appear in infinitely many orientations. By positioning particles at the vertices of the triangles, Pinwheel particle arrays are obtained with a high degree of rotational symmetry in the diffraction pattern. Isotropic plasmonic resonant surfaces were recently demonstrated by arranging metallic nanoparticles according to the Pinwheel geometry(Lee et al., 2011). Figure 6·1 (c,g) shows the direct and reciprocal space of a representative Pinwheel particle array. A diffuse background component in reciprocal space with higher rotational symmetry compared to A7 structures can be directly appreciated, along with fewer well defined diffraction peaks that originate from the finite-size of the array. In the limit of infinite-size arrays, Radin has in fact shown that there is no discrete component in the Pinwheel diffraction spectrum.(Radin, 1994)

On the other hand, an almost isotropic Fourier space, approaching continuous circular symmetry, can be obtained using finite-size arrays with deterministic aperiodic GA spiral order.(Trevino et al., 2011) GA spirals are a particular type of Vogel spirals. GA spiral arrays are obtained by a simple generation rule, expressed in polar coordinates r and θ, first proposed by Vogel in order to approximate the complex arrangements of florets in the sunflower head(Vogel, 1979; Mitchison, 1977; Adam, 2009):

$$r_n = a_0\sqrt{n} \tag{6.1}$$

$$\theta_n = n\alpha \tag{6.2}$$

where $n = 0, 1, 2, ...$ is an integer, α is a constant scaling factor, $\alpha \approx 137.508^o$ is an irrational number known as the golden angle that can be expressed as $\alpha = 360(1 - frac(\phi))$, where $frac$ denotes the fractional portion and $\phi = \frac{1+\sqrt{5}}{2} \approx 1.618$ is the golden number. The angle α gives the constant angular aperture between adjacent position vectors r_n

and r_{n+1} of particles in the array. The structure of a GA spiral can be decomposed into clockwise and counterclockwise families of out-spiraling lines of particles, known as *parastichies*, which stretch out from the center of the structure. Interestingly, the number of spiral arms in each family of parastichies is given by consecutive Fibonacci numbers.(Vogel, 1979) Moreover, since the golden angle is an irrational number, the GA spiral lacks both translational and rotational symmetry. Accordingly, its spatial Fourier spectrum does not exhibit well-defined Bragg peaks, as for standard photonic crystals and quasicrystals, but rather features a diffuse circular ring whose spectral position is determined by the particle's geometry. Figure 6·1 (d,h) shows the direct and reciprocal space structure of the GA spiral. Recently, GA spiral arrays of metallic nanoparticles were fabricated and polarization-insensitive planar light diffraction was demonstrated in the visible spectral range.(Trevino et al., 2011) Moreover, distinctive structural resonances carrying OAM were recently discovered in these plasmonic structures and analyzed using multiple scattering theory(Liew et al., 2011; Trevino et al., 2012). However, the light emitting properties of dielectric nanopillar arrays with Pinwheel and GA spiral geometries still remain to be investigated. In this section, a systematic study of the light extraction and emission properties of these novel types of active arrays is presented by focusing on Er:SiN_x nanopillars, which emit 1.55 μm radiation and can be reliably fabricated with a high degree of accuracy using well-established Si compatible processing.(Yerci et al., 2009; Yerci et al., 2010).

6.3 Design of Nanopillar Arrays for Light Extraction

6.3.1 Pillar Height Optimization

In order to optimize active pillar arrays for light extraction, the pillar height and the geometrical parameters of the arrays have been independently designed. Two-dimensional FDTD simulations are utilized to optimize the height of the nanopillars, while extrac-

tion calculations based on Bragg scattering theory(Wiesmann et al., 2009) are employed to optimize the pillar spacing for a given array geometry. While FDTD simulation are the most accurate, they are impractical to carry out on aperiodic patterns as the computational power required is too large. A schematic of the FDTD simulated structures is shown in the inset of Figure 6·2 (a), consisting of a thin waveguiding layer of Si-rich SiN_x (n = 2.1) on an SiO_2 substrate (n = 1.5) with a periodic grating of SiN_x pillars placed atop in order to extract the guided radiation. A mode source is injected into the SiN_x waveguiding layer and the radiation extracted from this mode, both into air and into the substrate, is quantified by calculating the optical power transmitted through planes positioned 10 μm above and below the device. The extracted power from the guided mode at 1.55 μm is plotted in Figure 6·2 (a) (red is power into substrate and blue is power into air) as a function of the pillar height. The results show a maximum in the power diffracted into air for a pillar height of 350 nm, exceeding the amount of power diffracted into the substrate by a factor of 2.

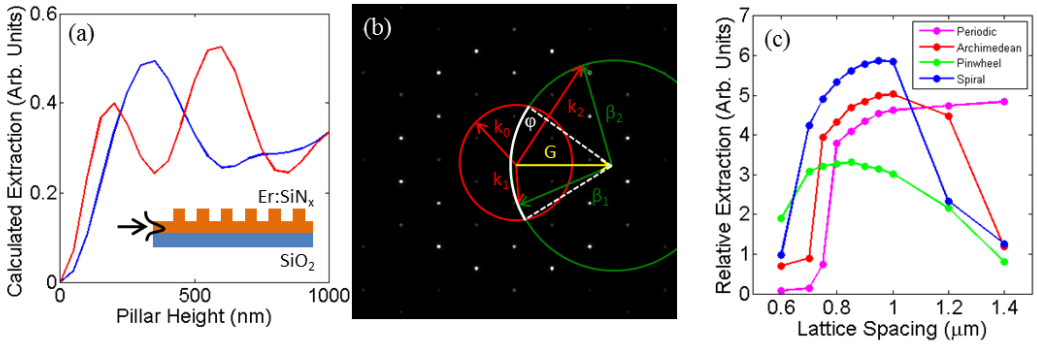

Figure 6·2: (a) Extraction of a guided mode by SiN_x pillars to air and the substrate with an inset of the device showing a mode injected into the SiN_x layer. (b) Fourier transform of an A7 lattice with vectors relevant to the Bragg scattering calculation. (c) Calculated extraction for periodic (magenta), Archimedean (red), Pinwheel (green), and GA spiral (blue) arrays versus spacing.

6.3.2 Array Optimization

Ideally, full vector 3D FDTD simulations of aperiodic arrays could be used to optimize the array geometry for light extraction however, the large size of the investigated aperiodic arrays prevents direct numerical calculations. Therefore, the optimal pillar spacing for any given array geometry is identified by resorting to analytical Bragg scattering theory(Wiesmann et al., 2009), which is a powerful method utilized for the design of LED extraction when strong photonic coupling effects can be neglected. Calculation of extracted light using the Bragg scattering method enables the exploration of a large parameter space at relatively low computational cost and provides the opportunity to optimize the lattice spacing and filling fraction of different arrays. In the case of weak scattering, the extraction of light is described by Bragg's law of diffraction, $\vec{\beta}_d = \vec{\beta}_i + \vec{G}$, where $\vec{\beta}_i$ is the input waveguide k-vector, $\vec{\beta}_d$ is the extracted (i.e., final) k-vector, and $\vec{G}$ is a reciprocal space vector obtained by computing the Fourier transform of the corresponding array. Based on Bragg's law of diffraction, we notice that if the input waveguide k-vector with amplitude $|\vec{\beta}_i| > |k_0|$ ($k_0 = \frac{2\pi}{\lambda}$ is the free space wavevector at wavelength λ) interacts with a suitable reciprocal space vector $\vec{G}$ giving rise to a final k-vector $\vec{\beta}_d$ with amplitude $|\vec{\beta}_d| < |k_0|$, then the input waveguide mode is folded back into the light cone and can be extracted from the device. Therefore, knowing the input waveguide k-vector, $\vec{\beta}_i$, and the reciprocal vectors, $\vec{G}$, of the structure, the overall extraction efficiency of a given array can be designed based exclusively on geometrical arguments. Figure 6·2 (b) illustrates an example of such Bragg scattering calculations, where the points along the green circle correspond to possible k-vectors resulting from the interaction $\vec{\beta}_i + \vec{G}$. As an example, Figure 6·2 (b) shows two vectors, named $\vec{k}_1 = \vec{\beta}_1 + \vec{G}$ and $\vec{k}_2 = \vec{\beta}_2 + \vec{G}$, of which $\vec{k}_1$ is extracted to the light cone while $\vec{k}_2$ is not. Based on this geometrical construction, we can define the extracted power, κ for the waveguide mode $\vec{\beta}_i$ as(Wiesmann et al.,

2009)

$$\kappa(\vec{\beta}_i, \vec{G}) \propto \begin{cases} |\epsilon_G|^2 & \text{if } |\vec{\beta}_i - \vec{G}| < |k_0| \\ 0 & \text{else} \end{cases} \tag{6.3}$$

where ϵ_G is the complex amplitude of the array Fourier transform at $\vec{G}$. The arc length $\ell = \phi\beta_i$, shown in Figure 6·2(b) in white, determines the in-plane directions for $\vec{\beta}_i$ that can be extracted by a given $\vec{G}$. Maximum efficiency is achieved for $|\vec{G}| \approx |\vec{\beta}_i|$, which determines the optimal vector amplitude, $\vec{G}$, for extracting a randomly oriented inplane input. The total extraction efficiency κ_{tot} of a given array geometry is therefore calculated by the integration over all the reciprocal space vectors, giving,

$$\kappa_{tot} \propto \beta_i \sum_G \phi(\vec{\beta}_i, \vec{G}) |\epsilon_G|^2. \tag{6.4}$$

This analysis makes us clearly appreciate that the optimal Fourier space for light extraction should consist in a circle of radius β_i. This condition guarantees the highest Bragg extraction efficiency for a randomly oriented set of input wavevectors, and it can be met by engineering isotropic Fourier space. For this reason A7 lattices, which possess a higher degree of local rotational symmetry compared to standard photonic crystals, have been proposed and utilized to efficiently extract radiation from LED devices(David et al., 2006; Rattier et al., 2003). It is therefore extremely interesting to investigate arrays with even higher rotational symmetry in Fourier space, such as the Pinwheel(Radin, 1994) and GA spirals(Vogel, 1979; Mitchison, 1977), displaying spectral features that are not present in structures with translational symmetry or in quasi-crystals. A summary of the Bragg scattering calculation results for the various investigated arrays is shown in Figure 6·2 (c). In all calculations, a modal effective index $n_{eff} = 1.7$ is considered, which is obtained following the procedure detailed in (Schonbrun et al., 2005), using the slab waveguide thickness and refractive index parameters measured by ellipsometry on the fabricated active material. In Figure 6·2 (c) κ_{tot}, calculated using

Equation 6.4, is plotted for the investigated geometries and for different values of pillar spacing. These results demonstrate clearly the importance of the arrays' geometry for light extraction. In particular, we can appreciate from this optimization that the best extraction is achieved by the GA spiral (blue curve). Interestingly, the A7 lattice (red curve) follows a similar trend compared to the GA spiral. The light extraction from the periodic array (magenta curve) also follows a similar trend with spacing yet with reduced efficiency. The Pinwheel array (green curve) shows the lowest value of peak extraction and a reduced sensitivity to pillar spacing. This is attributed to the diffuse nature of its Fourier spectrum (see Figure 6·1(e)), as compared to both A7 and GA spiral structures.

6.4 Experimental Characterization of Extraction Enhancement

6.4.1 Fabrication of Active Nanopillar Arrays

Aperiodic pillar arrays were fabricated from Si-rich Er:SiN_x using RF magnetron sputtering, electron beam lithography and reactive ion etching (RIE). First a 650nm layer of Er:SiN_x is deposited by RF reactive cosputtering by simultaneously sputtering Si and Er in an Argon/Nitrogen environment. By changing the relative power of the Si and Er targets the concentration of Er in the sample can be controlled, which must be kept at a low enough concentration that clustering of Er ions does not take place. Sputtered ions of Si bond with N in the sputter chamber to form SiN_x. By changing the relative concentration of argon and nitrogen in the chamber, the amount of excess silicon in the film can be controlled. After deposition the film must be annealed to activate the Er ions, this is done at 1100C for 200sec. Light emission at $1.55\mu m$ takes place from electron transitions in Er^{3+} ions. Er ions can be non resonantly excited by energy transfer from the SiN_x(Yerci et al., 2009). Electrical excitation is also possible(Yerci et al., 2010).

After material deposition and annealing a thin (180nm) layer of Poly(methyl methacry-

late) (PMMA) is deposited on the sample by spin coating at 2000rpm and then baked on a hot plate at 180C for 90sec. Electron beam lithography is then used to define the nanopillar arrays where selective areas are exposed in a Zeiss Supra 40VP scanning electron microscope. Nanopatterning software is used to control the beam (NPGS). The exposed areas of the sample are then removed by development in methyl-isobutyl ketone (MIBK) diluted in isopropyl alcohol at a ratio of 1:3. Next the sample is cleaned in a plasma asher to remove small amounts of PMMA that may remain after development. A thin (20nm) layer of Cr is then deposited on the sample by electron beam evaporation. The remaining PMMA and excess Cr are removed with a liftoff process in acetone. The pattern of Cr is transfer to the underlying Er:SiN_x by reactive ion etching using a CHF_3/O_2 chemistry. The plasma etching process leaves the surface of the Er:SiN_x very rough which is smoothed by a wet etching process in heated phosphoric acid (180C) to remove a small amount of Er:SiN_x. Scanning electron micrographs (SEMs) of fabricated periodic, Archimedean, pinwheel and GA spiral devices are shown in Figure 6·3 (a-h). All the fabricated arrays have been truncated using circular masks of identical size in order to ensure that pumping conditions are consistent during optical characterization.

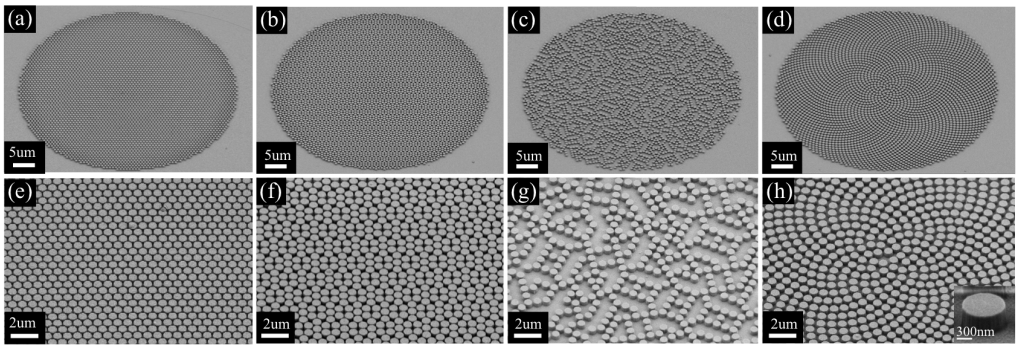

Figure 6·3: SEMs of (a) periodic, (b) Archimedean (A7), (c) pinwheel tiling, and (d) GA spiral nanopillar arrays fabricated in Er:SiN_x. (e-h) show close ups of each array to highlight the geometry. An inset of a single pillar is shown in the lower right corner of (h) with a height of 350nm. The arrays are 50 μm in diameter.

6.4.2 Optical Characterization of Active Nanopillar Arrays

The optical characterization of the fabricated structures is performed using PL spectroscopy (set-up shown in Figure 6·4 (a)) to quantify the extraction enhancement of nanopillar arrays with increasing degrees of Fourier space rotational symmetry. A diode laser, operating at 405nm, is used to excite the sample, which is weakly focused to a spot slightly smaller than the array size. A microscope with 50X (NA=.7) objective and CCD camera are used to align the pump with the sample. The sample is oriented so that the nanopillar arrays are facing the microscope and the pump beam is aligned in transmission. A flip mirror directs the light to either the CCD camera or monochromator attached to PMT for spectral measurements. A chopper and lock-in amplifier are used to reduce the noise.

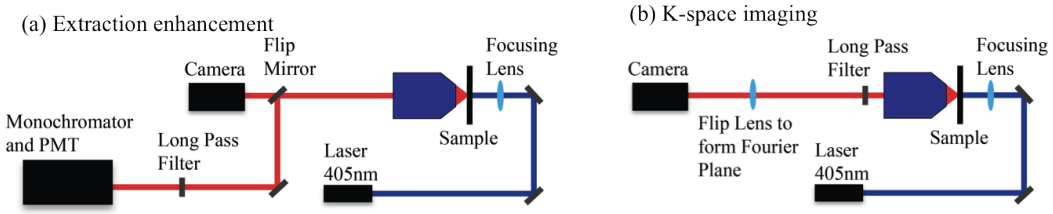

Figure 6·4: (a) Optical setup used for extraction enhancement measurements. (b) Optical setup used for K-space imaging.

The Er emission spectra corresponding to the optimized array structures are displayed in Figure 6·5 (a), together with the emission of the reference unpatterned device. All pillar arrays show a large increase in the emission signal. Moreover, no appreciable modification in the emission lineshape of Er is observed, indicating broadband enhancement.

In order to experimentally quantify the light extraction enhancement for the different arrays, the PL intensity is normalized to the emission collected from the unpatterned area (not masked during etch) of the device, when pumped under identical conditions. In Figure 6·5 (d) the experimentally measured extraction enhancement at 1.54 μm are

plotted for arrays with average first neighbor pillar spacing varying between 0.6-1.4 μm. To ensure that the arrays are optimized for light extraction at 1.54μm, pillar spacing has been varied while fill factor is kept constant. This is accomplished by choosing a constant pillar radius-to-pillar spacing ratio (R/A) equal to 0.4. This value was selected from Bragg scattering calculations for arrays with different values of R/A. Figure 6·5 (d) demonstrates a significant increase in extraction efficiency with an observed maximum enhancement factor of 10 times. This analysis demonstrates that the light extraction from GA spiral arrays exceeds that of Archimedean and pinwheel arrays. Interestingly, it is found that the periodic array gives the largest extraction enhancement when it is properly optimized. Previous studies have shown the Archimedean to outperform periodic photonic crystals(Wierer et al., 2009), though the structure of the device beyond the array geometry is also quite important(David et al., 2007). The performance of the periodic array is also not in agreement with the Bragg scattering calculations performed earlier in this chapter.

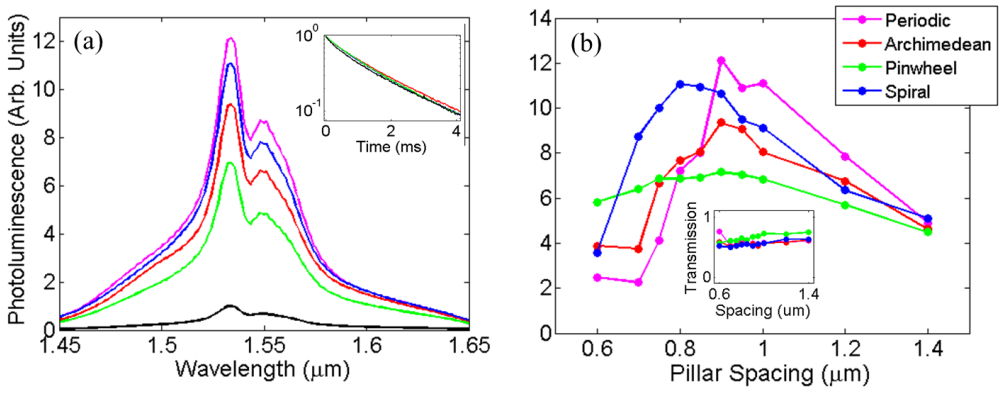

Figure 6·5: (a) Photoluminescence spectra from a periodic array (magenta), Archimedean (red), Pinwheel (green), and GA spiral (blue). The black curve is for an unpatterned area. The inset in (a) shows the PL lifetime of the same devices. (b) Extraction enhancement for nanopillar arrays versus average first neighbor spacing. The inset shows transmission of the pump through the same devices.

One limitation of the Bragg scattering calculations is that they do not take into

account the probability that a guided mode will interact with a photonic array but only account for where photons may go after interacting. The photonic arrays in this experiment are quite small compared to typical LED active areas, some of the emitted light does not have a chance to interact with the finite sized array. Since the Bragg peaks (lattice momentum) for the periodic array have significantly higher intensity than the lattice momentum provided by the GA spiral, the extraction length for a periodic array should be shorter. When the device size becomes much larger than the extraction length however, this effect will not change the total extracted light (however the ratio of extraction to absorption length will still be important). Thus, it is expected that for larger arrays the performance of the spiral array will increase relative to the periodic array, though without more rigorous calculations (such as 3D FDTD simulations) it is difficult to say how much.

As discussed earlier in this thesis (Chapter 2) a change in PL intensity in a photonic or plasmonic device can be caused by a change in the pumping efficiency, quantum efficiency or extraction efficiency. To rule out increased pumping efficiency as the cause of the observed PL increase, the transmission at the pump wavelength has been measured for each array. The pump transmission, shown in the inset of Figure 6·5 (b), displays little change among different array types and spacings. Some variation is detected ($\approx 10\%$) but it does not match the trend of PL and the change observed is too small to explain the large increase in PL intensity. Additionally, it is possible that confinement of light in the nanopillar arrays causes a change in the quantum efficiency of the sample, which could be detected as a change in the spontaneous emission lifetime. Measurements of the emission decay time are shown in the inset of Figure 6·5 (a) demonstrate no appreciable variations between the arrays. Therefore, the trends in Figure 6·5 (b) must result directly from the optimization of the array geometry for extraction efficiency. The trends are also in agreement with the theoretical calculations based on the Bragg

scattering analysis (Figure 6·2(c)).

6.5 Control of Angular Emission Patterns

In this section, by imaging the Fourier plane of the emitted radiation(Le Thomas et al., 2009), it is shown that deterministic aperiodic structures with azimuthally isotropic k-space provide not only increased light extraction efficiency but also opportunities for the generation of isotropic emission patterns controlled by the array geometry.

The experimental set up used for measuring the radiation profiles of nanopillar samples is shown in Figure 6·4 (b). The excitation of the sample is the same as for the measurements of the extraction enhancement, with a 405nm laser focused to the size of the arrays through the back of the sample. In this case however the remaining pump light is filtered out immediately after the microscope and the PL is imaged using an IR camera. To image the radiation profile (equivalent to the Fourier transform of the emitted light) a single lens is added to the optical set up so that the Fourier space is formed on the CCD camera instead of an image of the sample. This k-space imaging technique is significantly less complex and faster than using a moving detector on a rotational arm, a technique often used for angularly resolved measurements. Moreover, this technique gives angular resolution in 2 dimensions instead of just one. One limitation is that the maximum angle that can be observed is determined by the numerical aperture of the optical system.(Lai et al., 2009)

Figure 6·6 shows the measured k-space of Er emission collected from periodic (Figure 6·6 (a1-4)), Archimedean (Figure 6·6 (b1-4)), pinwheel (Figure 6·6(c1-4)), and GA spiral arrays (Figure 6·6 (d1-4)) with four increasing values (from left to right) of pillar spacing. The characteristic six-fold symmetry in the emission k-space of periodic and A7 lattices is noted, a feature that directly follows from their discrete rotational symmetry, as shown in Figure 6·1 (a,b,e,f). Moreover, when the pillar spacing increases the

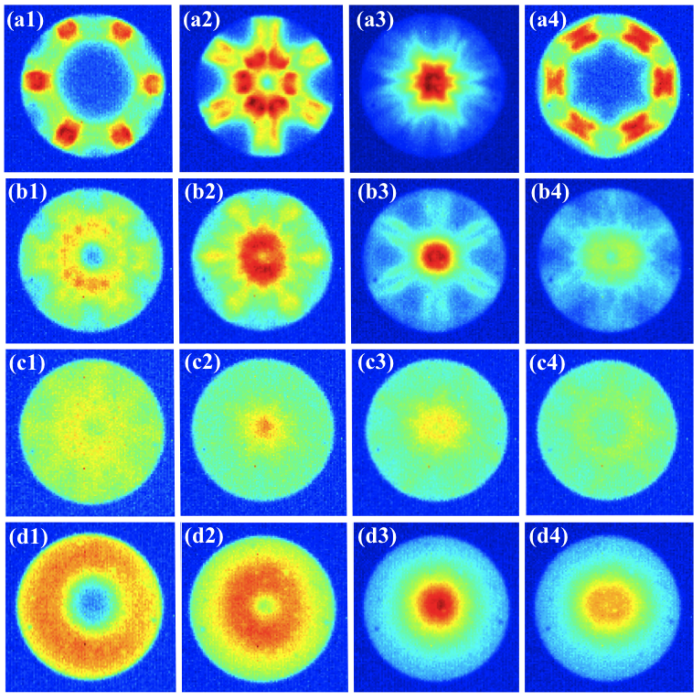

Figure 6·6: k-space images of IR emission from arrays of Er:SiN_x pillars. (a1-4) periodic arrays with lattice spacing of 850nm, 900nm, 950nm and 1000nm respectively. (b1-4) Archimedean arrays with lattice spacing of 850nm, 900nm, 950nm and 1000nm respectively. (c1-4) Pinwheel arrays with lattice spacing of 800nm, 850nm, 900nm and 950nm respectively. (d1-4) GA spiral arrays with lattice spacing of 700nm, 750nm, 800nm and 850nm respectively.

emission becomes more strongly localized at the center of the k-space image, indicating that more radiation is extracted normal to the chip. However, when the lattice spacing is further increased, the radiation spreads to a larger spot in k-space, and becomes less directional. We observe a similar trend also for the pinwheel arrays (Figure 6·6 (c1-b4)), even though they give rise to significantly more diffuse emission k-space patterns for all the pillar spacing compared to the periodic and Archimedean arrays. Interestingly, due to their higher degree of rotational symmetry in the k-space, pinwheel arrays produce emission patterns that are rather azimuthally isotropic, mostly evident in Figure 6·6 (c1,c4).

However, in sharp contrast to periodic and Archimedean arrays, the GA spirals show a remarkable degree of azimuthal isotropy in their emission k-space (Figure 6·6 (d1-d4)), observed at all pillar spacings. This is consistent with the more uniform distribution of the array lattie momentum, shown in Figure 6·1 (h). Moreover, the emission patterns of GA spirals can be designed to exhibit radiation components prevalently at large angles (Figure 6·6 (d1-d2)) or perpendicular to the array plane (Figure 6·6(d3-d4)), uniquely depending on the pillar spacing. These results therefore demonstrate that sufficiently intense and uniformly distributed k-vector components exist in the Fourier spectrum of the GA spirals to encode full circular symmetry onto the Er radiation patterns extracted around 1.55 μm.

6.6 Conclusions

In conclusion, this chapter presents the engineering of aperiodic active devices with a high degree of rotational symmetry in Fourier space for omnidirectional extraction and emission profile shaping. Aperiodic pillar arrays of Er:SiN_x are fabricated using silicon based planar processing for efficient light extraction at 1.55 μm. Structural optimization of pillar height and array geometry is performed using FDTD simulations and Bragg scattering calculations. Devices of different array geometry and pillar spacing are optically characterized with PL spectroscopy and extraction enhancement of over 10 times is demonstrated for GA spiral arrays, outperforming both Archimedean and Pinwheel arrays. The angular emission profiles are measured, demonstrating azimuthally isotropic emission in GA spiral structures. These findings offer unique opportunities for the engineering light extraction while maintaining azimuthally isotropic emission patterns.

Chapter 7

Analytical Light Scattering and Orbital Angular Momentum in Vogel Spirals

7.1 Introduction

First introduced to this thesis in Chapter 6, Vogel spirals have been the topic of much research recently as a novel platform for nanophotonics(Trevino, 2013; Dal Negro and Boriskina, 2012). Moreover, Vogel spiral arrays support distinctive scattering resonances carrying orbital angular momentum (OAM)(Trevino et al., 2011; Liew et al., 2011). GA spirals in particular have been shown to generate sequences of OAM with azimuthal values corresponding to the Fibonacci sequence, which has recently been investigated as a novel secure communication protocol(Simon et al., 2013). The controlled generation and manipulation of well-defined OAM sequences carrying large values of azimuthal numbers using planar Vogel arrays could lead to novel nanophotonic active and passive structures. However, a general analytical model capable of providing insights into the fundamental optical behavior and design principles for the manipulation of scattered radiation by general aperiodic Vogel spirals is still missing, confining their engineering analysis to the often unattainable numerical simulation of large-scale aperiodic systems.

In this chapter, an analytical model for light scattering by arbitrary arrays of circular apertures illuminated at normal incidence is derived. In particular, the closed form solution for Fraunhofer diffraction is shown using scalar diffraction theory. The method developed is used to investigate the far field scattering from Vogel spiral arrays. By performing analytical Fourier-Hankel decomposition (FHD) of far field patterns, the encoding of specific numerical sequences in the OAM values of diffracted optical beams is demonstrated. These results unveil the fundamental mathematical structure of the complex diffraction patterns of Vogel spirals and their connection with the OAM values coded in the far fields. Specifically, it is demonstrated mathematically that generated OAM azimuthal values are directly related to distinctive number-theoretic properties of the Vogel spiral geometry. Finally, field propagation to arbitrary distances is derived analytically which gives insight into the formation of far-field patterns.

7.2 Scattering from Arbitrary Arrays of Nanoparticles

Using scalar diffraction theory, an analytical solution for the far-field diffraction pattern from an arbitrary array of apertures is presented. A point pattern consisting of N particles is defined by the following density function,

$$\rho(r,\theta) = \sum_{n=1}^{N} \frac{1}{r}\delta(r - r_n)\delta(\theta - \theta_n) \tag{7.1}$$

where (r_n, θ_n) is the location of the n_{th} particle and the $\frac{1}{r}$ factor comes from the definition of the Delta function in cylindrical coordinates. If a plane wave is normally incident on the array, the field at the plane of the array ($z = 0$) is given by,

$$E_{z=0}(r,\theta) = \frac{E_0}{r}\sum_{n=1}^{N} \delta(r - r_n)\delta(\theta - \theta_n). \tag{7.2}$$

Within the validity limits of scalar diffraction theory, the Fraunhofer far field of a general point pattern density function is obtained by the evaluation of its Fourier transform, carried out here in cylindrical coordinates,

$$E_\infty(\nu_r, \nu_\theta) = \sum_{m=-\infty}^{\infty} (j)^m e^{jm\nu_\theta} 2\pi \int_0^\infty r\rho_m(r) J_m(2\pi\nu_r r) dr \tag{7.3}$$

where,

$$\rho_m(r) = \frac{1}{2\pi} \int_{-\pi}^{\pi} E_{z=0}(r, \theta) e^{-jm\theta} d\theta \tag{7.4}$$

and $J_m(2\pi\nu_r r)$ is the m_{th} order Bessel function of the first kind. The variables (ν_r, ν_θ) are the Fourier conjugates of the direct-space variables (r, θ), used to represent the array density. The integral in Equation 7.4 can be analytically evaluated using the sampling property of the Dirac delta function to obtain,

$$\rho_m(r) = \frac{E_0}{2\pi r} \sum_{n=1}^{N} \delta(r - r_n) e^{-jm\theta_n} \tag{7.5}$$

Now, Equation 7.3 can be evaluated by inserting Equation 7.5, yielding,

$$E_\infty(\nu_r, \nu_\theta) = \sum_{m=-\infty}^{\infty} j^m e^{jm\nu_\theta} \int_0^\infty E_0 \sum_{n=1}^{N} \delta(r - r_n) e^{-jm\theta_n} J_m(2\pi\nu_r r) dr. \tag{7.6}$$

Exchanging the order of the summation and integral in Equation 7.6 and using again the sampling property of the delta function gives,

$$E_\infty(\nu_r, \nu_\theta) = E_0 \sum_{n=1}^{N} \sum_{m=-\infty}^{\infty} j^m J_m(2\pi r_n \nu_r) e^{jm(\nu_\theta - \theta_n)}. \tag{7.7}$$

Using the well-known cylindrical wave expansion of a plane wave,

$$e^{jzcos\phi} = \sum_{m=-\infty}^{\infty} j^m J_m(z) e^{jm\phi} \tag{7.8}$$

finally gives the closed form analytical solution for the Fraunhofer far-field pattern of an arbitrary point pattern array,

$$E_\infty(\nu_r, \nu_\theta) = E_0 \sum_{n=1}^{N} e^{j2\pi r_n \nu_r cos(\nu_\theta - \theta_n)}. \tag{7.9}$$

7.2.1 Finite Particle Sizes

The analytical diffraction solution for an arbitrary array of identical circular apertures of finite radius is obtained using the general convolution property of the Fourier transform. This is accomplished by multiplying the point pattern solution in Equation 7.9 by the Fourier transform of the individual particle shape. While the Fourier transform of an arbitrary aperture cannot be calculated analytically some simple cases can. One example is a circular aperture, given in direct space by

$$\rho(r, \theta) = circ(\frac{r}{a}) \tag{7.10}$$

where circ is the circular step function with radius a and Fourier transform,

$$F(\rho(r, \theta)) = \frac{a}{\nu_r} J_1(2\pi\nu_r a). \tag{7.11}$$

The diffraction of a normally incident plane wave through an arbitrary array of circular apertures is then given by

$$E_\infty(\nu_r, \nu_\theta) = E_0((\frac{a}{\nu_r}) J_1(2\pi\nu_r a)) \sum_{n=1}^{N} e^{j2\pi r_n \nu_r cos(\nu_\theta - \theta_n)}. \tag{7.12}$$

Using Equation 7.12, the far-field scattering patterns of several well known arrays are calculated. Figure 7·1 (a,b) shows the direct space of square periodic and Penrose arrays of circular apertures, respectively. The analytically calculated far-field radiation patterns, according to Equation 7.9, are shown in Figure 7·1 (c,d). The square periodic array has 4-fold symmetry in direct space. The far-field radiation pattern also exhibits

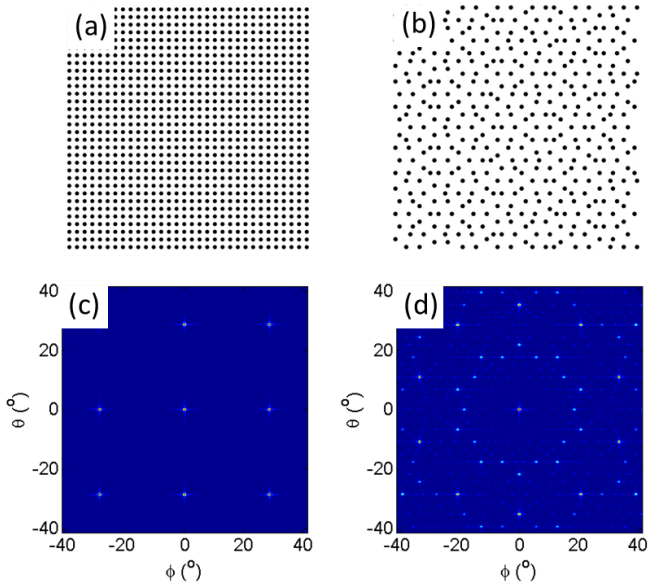

Figure 7·1: (a,b) Square Periodic and Penrose arrays of circular apertures. (c,d) Far-field radiation pattern (according to Equation 7.12) of corresponding arrays in (a,b) illuminated with a normally incident planewave.

the same rotational symmetry and is composed of discrete Bragg peaks along the edges of the first Brillouin Zone. The Penrose array is quasi-periodic with 5-fold rotational symmetry. The lattice does not have translational symmetry but the Fourier space still consists of discrete Bragg peaks with 5-fold rotational symmetry.

7.2.2 Scattering from Vogel Spirals

While the derivation presented here can be used to calculate the far-field scattering from an arbitrary point pattern, the remainder of this chapter will focus on Vogel spirals. Vogel spirals are deterministic aperiodic point patterns generated from the simple rules,

$$r_n = \sqrt{n} a_0 \tag{7.13}$$

$$\theta_n = n\alpha \tag{7.14}$$

Irrational Number	Equation	Aperture Angle (α)
ϕ	$\frac{1+\sqrt{5}}{2}$	137.51...
τ	$\frac{2+\sqrt{8}}{2}$	210.88...
μ	$\frac{5+\sqrt{29}}{2}$	290.67...
π	3.14159...	309.03...

Table 7.1: Irrational numbers and corresponding spiral aperture angles.

giving the locations of the n_{th} particle. The pattern is defined by a_0, the scaling factor, and α, the divergence angle. When an irrational number is chosen for α a pattern is generated which lacks rotational and translational symmetry.

Using Equation 7.9, the analytically calculated scattering from four different Vogel's spirals is shown in Figure 7·2. Figure 7·2 (a) shows the direct space of a Golden Angle (GA) spiral which is generated using the golden angle, an angular corollary to the golden ratio, $\phi = \frac{1+\sqrt{5}}{2}$. The divergence angle can be calculated for the golden ratio according to $\alpha = 2\pi(1 - frac(\phi))$ Figure 7·2 (e) shows the far-field diffraction pattern (proportional to the analytic fourier transform) of a GA spiral point pattern. Figure 7·2 (b,f) shows the direct space and far-field radiation pattern of a τ spiral generated using an irrational number, $\tau = \frac{2+\sqrt{8}}{2}$. Figure 7·2 (c,g) shows the direct space and far-field radiation pattern of a μ spiral generated using an irrational number, $\mu = \frac{5+\sqrt{29}}{2}$. Finally, Figure 7·2 (d,h) shows the direct space and far-field radiation pattern of a π spiral generated using an irrational number $\pi = 3.14159\ldots$. The Vogel spiral names, irrational numbers used for generation and calculated divergence angles are shown in Table 7.2.2. The unique property of Vogel spiral scattering is the presence of a ring of scattered intensity, which comes from the lack of rotational symmetry and can be seen for all Vogel spirals.

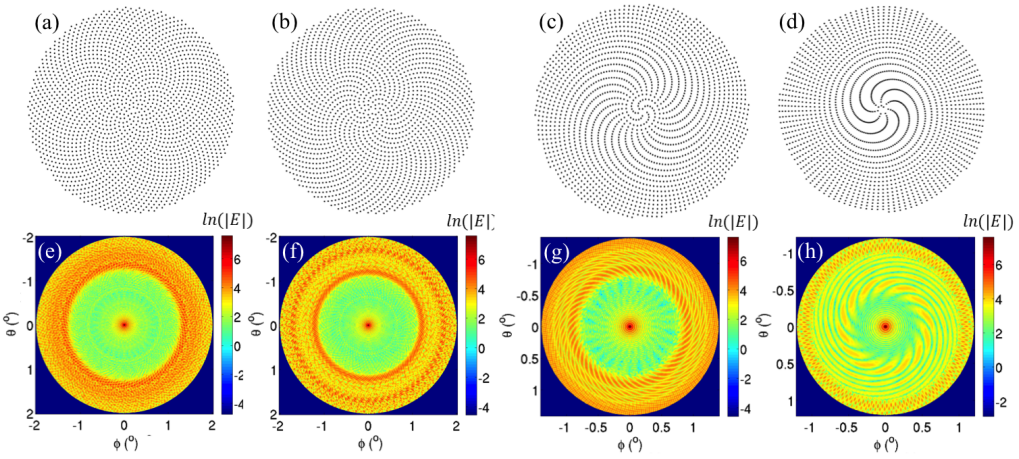

Figure 7·2: (a-d) ϕ, τ, μ, π Vogel spirals, respectively, with 2000 particles each. (e-h) Analytically calculated far field radiation pattern of arrays in (a-d) respectively at a wavelength of 633nm for a structure with $a_0 = 14.5\mu m$. The far field radiation pattern has been truncated with an angular aperture of 4°.

7.3 Derivation of Fourier-Hankel Decomposition

To find the OAM carried by the complex patterns of scattered field generated by Vogel spirals, the electric field must be decomposed into a basis set of functions carrying OAM. This is done using the Fourier-Hankel transform (FHT), defined as,

$$f(m, k_r) = \frac{1}{2\pi} \int_0^{\infty} \int_0^{2\pi} r dr d\theta E(r, \theta) J_m(k_r r) e^{im\theta} \tag{7.15}$$

where, $k_r = 2\pi\nu_r$ and $E(r, \theta)$ is the complex electric field. Using Equation 7.12, the far-field diffraction of a normally incident plane wave through a Vogel spiral array of circular apertures is given by,

$$E_{\infty}(\nu_r, \nu_\theta) = E_0(\frac{a}{\nu_r}) J_1(2\pi\nu_r a) \sum_{n=1}^{N} e^{j2\pi\sqrt{n}a_0\nu_r cos(\nu_\theta - n\alpha)}. \tag{7.16}$$

The FHT of the complex far field in Equation 7.16 is given by

$$f(m,k_r) = \frac{E_0 a}{2\pi}\int_0^{\infty}\int_0 2\pi d\nu_r d\nu_\theta \sum_{n=1}^{N} e^{j2\pi\sqrt{n}a_0\nu_r cos(\nu_\theta - n\alpha)} J_m(2\pi r\nu_r) J_1(2\pi\nu_r a) e^{im\nu_\theta}, \tag{7.17}$$

which can be rewritten as,

$$f(m,k_r) = \frac{E_0 a}{2\pi}\sum_{n=1}^{N}\int_0^{\infty}\int_0 2\pi d\nu_r d\nu_\theta e^{j2\pi\sqrt{n}a_0\nu_r cos(\nu_\theta - n\alpha)} J_m(2\pi r\nu_r) J_1(2\pi\nu_r a) e^{im\nu\theta}. \tag{7.18}$$

The integral over ν_θ can be eliminated by using the following representation for the Bessel function

$$J_{-m}(k_\rho\rho)e^{-im\phi} = \frac{1}{2\pi}\int_0^{2\pi} d\beta e^{ik_\rho\rho cos(\beta-\phi)+im\beta+im\frac{\pi}{2}} \tag{7.19}$$

after the substitutions, $\beta \to \nu_\theta$, $\phi \to n\alpha$, $\rho \to \nu_r$, $k_\rho \to 2\pi\sqrt{n}a_0$. Equation 7.18 now reduces after few simple steps to:

$$f(m,k_r) = \frac{E_0 a}{2\pi}(-i)^m \sum_{n=1}^{N} e^{-inm\alpha}\int_0^{\infty} d\nu_r J_m(2\pi r\nu_r) J_{-m}(2\pi\sqrt{n}a_0\nu_r) J_1(2\pi\nu_r a) \tag{7.20}$$

Though this expression is complicated, it has the general mathematical structure,

$$f(m,k_r) \propto \sum_{n=1}^{N} A_{m,k_r} e^{inm\alpha}. \tag{7.21}$$

This is a central result in the analytical study. By focusing on the component of Equation 7.21 which is dependent on m, the azimuthal values of OAM produced by a Vogel spiral pattern will become apparent. The k_r dependent portion of Equation 7.21 will only have an effect on the relative intensity of the OAM production at different m values.

7.3.1 Generation of OAM with Vogel Spirals

By focusing on the $e^{inm\alpha}$ component of Equation 7.21, the azimuthal values of OAM generated by a particular Vogel spiral can be understood. Since Equation 7.21 contains a sum of numerous complex waves, which will have phase dependent of n, this sum should tend to zero unless $m\alpha$ is an integer multiple of 2π. Remembering that $\alpha = 2\pi\psi$ where ψ is the irrational generation number, it seems this condition should never be satisfied. However, this condition will be approximately satisfied for any m value such that $m\psi \approx \mathbb{Z}$. Values of m that satisfy this condition can be found by approximating ψ with a fraction.

Fractions which approximate an irrational number are called rational approximants. The Golden ratio, for example, is approximated with increasing accuracy by ratios of successive Fibonacci numbers, $\phi \approx \frac{F_{n+1}}{F_n}$, where F_n is the n_{th} Fibonacci number. Therefore, for m values equal to Fibonacci numbers, the sum over particle number in Equation 7.21 will produce complex exponentials which are *in phase*. This will create a peak in the Fourier-Hankel transform, indicating the production of OAM at that azimuthal number. For the golden angle spiral the result is that OAM is produced with azimuthal numbers equal to Fibonacci numbers.

This analysis can be extended to an arbitrary divergence angle α which is determined by an arbitrary irrational number ψ. Any irrational number can be represented by a unique continued fraction as:

$$\psi = [a_0; a_1, a_2, a_3, ...] = a_0 + \cfrac{1}{a_1 + \cfrac{1}{a_2 + \cfrac{1}{a_3 + ...}}}. \tag{7.22}$$

An infinite continued fraction representation of an irrational number is very useful because its initial segments provide excellent rational approximations to that number. The rational approximations are also called the convergents of the continued fraction, and it

can be shown that even-numbered convergents are smaller than the original number ψ while odd-numbered ones are bigger(Hardy and Wright, 2008; Schroeder, 1985). Once the continued fraction expansion of ψ has been obtained, well-defined recursion rules exist to quickly generate the successive convergents. In fact, each convergent can be expressed explicitly in terms of the continued fraction as the ratio of certain multivariate polynomials called continuants(Hardy and Wright, 2008; Schroeder, 1985).

If two convergents are found, with numerators p_1, p_2 and denominators q_1, q_2 then the successive convergents are given by the formula,

$$\frac{p_n}{q_n} = \frac{a_n p_{n-1} + p_{n-2}}{a_n q_{n-1} + q_{n-2}} \tag{7.23}$$

Thus to generate new terms into a rational approximation only the two previous convergents are necessary. The initial or seed values required for the evaluation of the first two terms are $(0, 1)$ and $(1, 0)$ for (p_{-2}, p_{-1}) and (q_{-2}, q_{-1}), respectively.

It is clear from the discussion above that for spirals generated using an arbitrary irrational number ψ, azimuthal peaks of order m will appear in its FHT due to the denominator q_n of the rational approximations (i.e., the convergents) of $\psi \approx \frac{p_n}{q_n}$. In fact, for all integer Bessel orders $m = q_n$ the exponential sum in Equation 7.21 gives *in phase* contributions to the FHT creating strong peaks. Therefore, once the rational approximations of ψ have been identified based on continued fractions, a Vogel spiral geometry can be designed that encodes in its FHT peaks, the numeric sequence associated to the rational approximant denominators, q_n.

In order to better illustrate these important aspects of this analysis, the scattering properties of four different Vogel spirals generated by the irrational numbers $\phi = \frac{1+\sqrt{5}}{2}$, $\tau = \frac{2+\sqrt{8}}{2}$, $\mu = \frac{5+\sqrt{29}}{2}$, the mathematical constant π will be discussed. The rational approximants of these numbers are shown in Table 7.3.1 along with the parameter $\frac{E}{M}$.

This parameter, which ranges from 0 to 1, is a measure of the difficulty of approxi-

Irrational Number	Rational Approximations $\frac{p}{q}$	$\frac{E}{M}(q)$
ϕ	$\frac{1}{1}, \frac{2}{1}, \frac{3}{2}, \frac{5}{3}, \frac{8}{5}, \frac{13}{8}, \frac{21}{13}, \frac{34}{21}, \frac{55}{34}, \frac{89}{55}, \frac{144}{89}, \frac{233}{144}$	0.99999 (144)
τ	$\frac{1}{1}, \frac{5}{2}, \frac{12}{5}, \frac{29}{12}, \frac{70}{29}, \frac{169}{70}, \frac{408}{169}$	.79057 (169)
μ	$\frac{5}{1}, \frac{26}{5}, \frac{135}{26}, \frac{701}{135}$	0.41523 (135)
π	$\frac{3}{1}, \frac{22}{7}, \frac{355}{113}$	0.00762 (113)

Table 7.2: Irrational numbers and their rational approximants.

mating irrational numbers using rationales. The parameter $\frac{E}{M}$ is defined as the ratio of the approximation error, E, to the Hurwitz bound $M = \frac{1}{\sqrt{5}q^2}$. This definition follows from the Hurwitz theorem(Havil, 2012), which states that every number has infinitely many rational approximations of the form $\frac{p}{q}$ with an approximation error less than M. Table 7.3.1 shows that, in this precise sense, the golden number, $\phi = \frac{1+\sqrt{5}}{2}$, is the most irrational number because its approximation error is as large as possible compatible to the Hurwitz bound. This slow convergence is contrasted with π, whose rational approximation error is much better than the Hurwitz theoretical bound. The values of the two other irrational numbers in Table 7.3.1 are chosen at intermediate $\frac{E}{M}$ values in order to study Vogel spirals obtained by irrational numbers sampled across the $[0, 1]$ interval.

To investigate the generation of OAM with Vogel spirals, Equation 7.9 is used to calculate the far-field radiation patterns of Vogel Spiral point patterns generated using the different irrational numbers investigated in Table 7.3.1. The far-field patterns are then decomposed numerically using the Fourier-Hankel transform and summed over different values of k_r to find the azimuthal numbers of OAM which are produced by a Vogel spiral pattern. Figure 7.3.1 (a-d) shows the azimuthal numbers of OAM produced by Vogel spirals generated with ϕ, τ, μ and π respectively. The peaks in the FHT correspond to the denominators of the rational approximants of the irrational numbers used to generate the spirals.

Figure 7.3.1 also shows a decreasing number of peaks, associated to reduced struc-

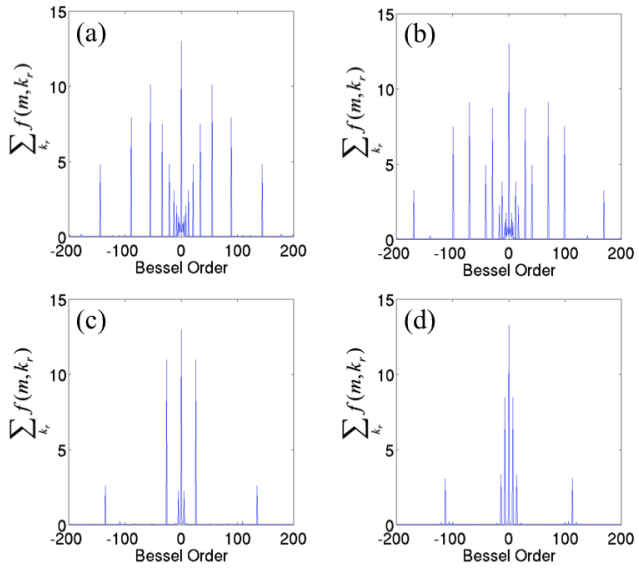

Figure 7·3: Fourier-Hankel transforms of far field scattered radiation from ϕ, τ, μ and π (Figure 7·2(a-d)) Vogel spirals summed over the radial wavenumber k_r.

tural complexity, for structures generated by divergence angles that are less irrational (i.e., that are better approximated in rationales in the Hurwitz sense explained above). Therefore, Vogel spiral structures with large $\frac{E}{M}$ values are ideal to transmit very rich spectra of OAM values in the far field.

In order to understand the role played by the particle number in the far-field OAM spectra, Figure 7.3.1 shows the calculated far fields and the corresponding OAM spectra (i.e., FHT of the far fields) for GA spirals of increasing particle numbers, ranging from N = 500 to 4000. It is seen in Figure 7.3.1 that azimuthal peaks at larger Bessel orders start to appear as the size of the spirals increase and the azimuthal structure of the scattered far-field becomes richer. However, the effect is not dramatic and the OAM spectra are quite stable with respect to the particle number in the arrays, as long as they are sufficiently large (i.e., few hundreds in this case).

On the other hand, a much more dramatic effect occurs when sampling the far-field

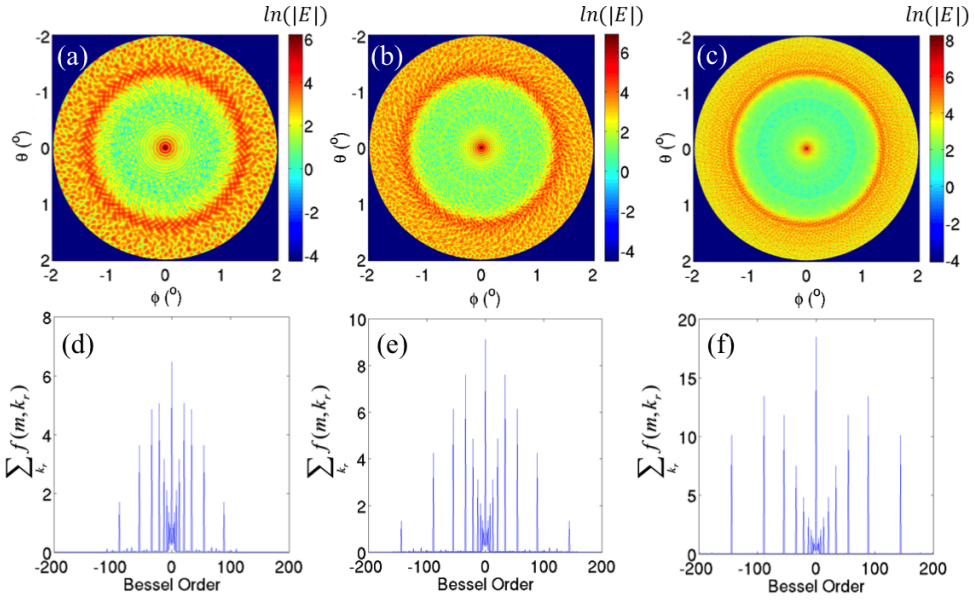

Figure 7·4: (a-c) Far-field radiation pattern of GA spirals with 500, 1000 and 4000 particles respectively. (d-f) Fourier-Hankel transform of (a-c), respectively, summed over the radial wavenumber k_r at a wavelength of 633nm for a structure with $a_0 = 14.5\mu m$. The far field radiation pattern has been truncated with an angular aperture of 4°.

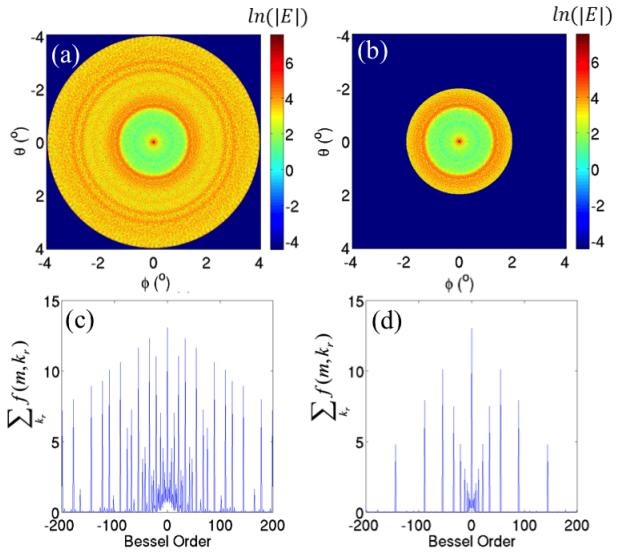

Figure 7·5: (a,b) Far field radiation pattern of GA spirals truncated with different apertures, (a) 8°, (b) 4°. (c,d) Fourier-Hankel transform of (a,b), respectively, summed over the radial wavenumber k_r at a wavelength of 633nm for a structure with $a_0 = 14.5\mu m$ and 2000 particles.

spectra over larger angular windows, corresponding to larger cross sections of scattered beams in the far-field. This is demonstrated, in the case of the GA spiral, by Figure 7.3.1. For larger apertures, the spectra in Figure 7.3.1 (c,d) become much more densely populated by peaks at azimuthal orders corresponding to larger Fibonacci and Lucas numbers, which are found among the denominators of the rational approximations of the golden number. The angular size on the diffracted beam in the far-field is therefore very important and directly affects the range of discrete OAM values that can be obtained in the far-field zone.

The positions of all the peaks in the OAM spectra of the structures analyzed in Figure 7.3.1 and Figure 7.3.1 are summarized in Table 7.3.1. As predicted by the analytical model, Table 7.3.1 demonstrates that all the OAM peak positions correspond to azimuthal orders that coincide with the denominators of the rational approximations of the irrational numbers used to generate the different spirals. These results there-

Spiral	Fourier-Hankel Transform Peaks
GA	2, 3, 5, 8, 13, 21, 34, 55, 89, 144
τ	2, 5, 7, 12, 17, 29, 41, 70, 99, 169
μ	5, 26, 135
π	7, 14, 113
GA Large Aperture	2, 3, 5, 8, 13, 21, 26, 29, 34, 42, 47, 55, 68, 76, 89, 110, 123, 144, 178, 199
GA Small Aperture	2, 3, 5, 8, 13, 21, 34, 55, 89, 144

Table 7.3: Azimuthal numbers of FHT peaks.

fore demonstrate the general ability of Vogel spirals to encode pre-defined numerical sequences in the OAM spectra of far-field scattered radiation.

7.4 Field Propagation to Arbitrary Distances

In this last section, an analytical derivation is shown of the field scattered by a general Vogel spiral at a finite observation plane in the near and intermediate field zones, using the general angular spectrum representation approach. In a Cartesian coordinate system, the transverse field sampled at an arbitrary plane $z = d$ can be written as:

$$E(x, y; d) = F^{-1}(H(2\pi\nu_x, 2\pi\nu_y; d)E(2\pi\nu_x, 2\pi\nu_y; 0)) \tag{7.24}$$

where $H(2\pi\nu_x, 2\pi\nu_y; d) = e^{j2\pi d\sqrt{\frac{1}{\lambda^2}-\nu_x^2-\nu_y^2}}$ is the free-space propagator in reciprocal space, $E(2\pi\nu_x, 2\pi\nu_y; 0)$ is the Fourier transform of the field at the object plane, and F^{-1} denotes the inverse Fourier transform operation. Equation 7.24 can be evaluated in cylindrical coordinates, using the free-space propagator,

$$H(\nu_r; d) = e^{j2\pi d\sqrt{\frac{1}{\lambda^2}-\nu_r^2}} \tag{7.25}$$

and the previously derived Fourier transform of the spiral,

$$E_{\infty}(\nu_r, \nu_\theta) = E_0 \sum_{n=1}^{N} e^{j2\pi\sqrt{n}a_0\nu_r cos(\nu_\theta - n\alpha)}. \tag{7.26}$$

Therefore, Equation 7.24 can be written as,

$$E(r, \theta; d) = F^{-1}(E_0 \sum_{n=1}^{N} e^{j2\pi\sqrt{n}a_0\nu_r cos(\nu_\theta - n\alpha)} e^{j2\pi d\sqrt{\frac{1}{\lambda^2} - \nu_r^2}}) = F^{-1}(G(\nu_r, \nu_\theta)). \tag{7.27}$$

Using the cylindrical representation of the inverse Fourier transform, Equation 7.26 is rewritten as,

$$E(r, \theta; d) = \sum_{-\infty}^{\infty} (j)^m e^{jm\theta} 2\pi \int_0^{\infty} \nu_r G_m(\nu_r) J_m(2\pi\nu_r r) d\nu_r \tag{7.28}$$

where,

$$G_m(\nu_r) = \frac{1}{2\pi} \int_{-\pi}^{\pi} G(\nu_r, \nu_\theta) e^{-jm\nu_\theta} d\nu_\theta \tag{7.29}$$

Substituting the definition of $G(\nu_r, \nu_\theta)$ into Equation 7.29 gives,

$$G_m(\nu_r) = \frac{E_0}{2\pi} \int_{-\pi}^{\pi} d\nu_\theta \sum_n e^{j(2\pi a_0\sqrt{n}\nu_r cos(\nu_\theta - n\alpha) + 2\pi d\sqrt{\frac{1}{\lambda^2} - \nu_r^2} - m\nu_\theta)} \tag{7.30}$$

which can be expressed as

$$G_m(\nu_r) = \frac{E_0}{2\pi} e^{2\pi d\sqrt{\frac{1}{\lambda^2} - \nu_r^2}} \sum_{n=1}^{N} \int_{-\pi}^{\pi} d\nu_\theta e^{j(2\pi a_0\sqrt{n}\nu_r cos(\nu_\theta - n\alpha) - m\nu_\theta)}. \tag{7.31}$$

The definite integral in Equation 7.31 can be evaluated by recalling the following representation of the m_{th} order Bessel function,

$$J_m(k_\rho\rho) e^{jm\phi} = \frac{1}{2\pi} \int_0^{2\pi} d\alpha e^{jk_\rho\rho cos(\alpha - \phi) - jm\alpha - jm\frac{\pi}{2}} \tag{7.32}$$

where $(k_\rho\rho, \omega, \phi)$ are replaced with $(2\pi a_0\sqrt{n}\nu_r, \nu_\theta, n\alpha)$. Therefore the scattered field at a given plane $z = d$ can be expressed from Equation 7.28 as:

$$E(r,\theta;d)$$
$$= E_0 \sum_{m=-\infty}^{\infty} (j)^m e^{jm\theta} \int_0^{\infty} \nu_r e^{j2\pi d\sqrt{\frac{1}{\lambda^2}-\nu_r^2}} \sum_{n=1}^{N} \int_{-\pi}^{\pi} d\nu_\theta e^{j(2\pi a_0\sqrt{n}\nu_r cos(\nu_\theta - n\alpha) - m\nu_\theta} J_m(2\pi\nu_r r) d\nu_r \tag{7.33}$$

Using Equation 7.32, Equation 7.33 can be reduced to:

$$E(r,\theta;d)$$
$$= 2\pi E_0 \sum_{m=-\infty}^{\infty} (j)^m e^{jm\theta} e^{jm\frac{\pi}{2}} \sum_{n=1}^{N} e^{-jmn\alpha} \int_0^{\infty} \nu_r e^{j2\pi d\sqrt{\frac{1}{\lambda^2}-\nu_r^2}} J_m(2\pi a_0\sqrt{n}\nu_r) J_m(2\pi\nu_r r) d\nu_r. \tag{7.34}$$

The integral in Equation 7.33 can be further simplified by using the Gegenbauer theorem for cylindrical functions,

$$J_0(k_r R) = \sum_{m=-\infty}^{\infty} J_m(k_r r_1) J_m(k_r r_2) e^{im\theta}. \tag{7.35}$$

In fact, continuing from Equation 7.34 we have,

$$E(r,\theta;d) = 2\pi E_0 \sum_{n=1}^{N} \int_0^{\infty} \nu_r e^{j2\pi d\sqrt{\frac{1}{\lambda^2}-\nu_r^2}} \sum_{m=-\infty}^{\infty} e^{jm(\theta+\pi-n\alpha)} J_m(2\pi a_0\sqrt{n}\nu_r) J_m(2\pi\nu_r r) d\nu_r \tag{7.36}$$

$$E(r,\theta;d) = 2\pi E_0 \sum_{n=1}^{N} \int_0^{\infty} \nu_r e^{j2\pi d\sqrt{\frac{1}{\lambda^2}-\nu_r^2}} J_0(k_r R) d\nu_r \tag{7.37}$$

which is the main closed form expression for the scattered field obtained after the following identifications have been made,

$$r_1 = a_0\sqrt{n},\ r_2 = r,\ k_r = 2\pi\nu_r,\ R = \sqrt{r_1^2 + r_2^2 - 2r_1 r_2 cos(\beta)},\ \beta = \theta + \pi - n\alpha. \tag{7.38}$$

Equation 7.37 and Equation 7.38 are the analytical solutions for the transverse field probed at $z = d$ scattered by an arbitrary Vogel spiral of point scatterers. If a spiral

pattern of circular apertures of radius a is considered instead, the general solution can be easily modified to obtain:

$$E(r,\theta;d) = 2\pi E_0 a \sum_{n=1}^{N} \int_0^{\infty} e^{j2\pi d\sqrt{\frac{1}{\lambda^2}-\nu_r^2}} J_0(k_r R) J_1(2\pi\nu_r a) d\nu_r \tag{7.39}$$

Equation 7.39 explicitly contains the multiplicative Airy factor ($\frac{a}{\nu_r} J_1(2\pi\nu_r a)$) that accounts for the finite size of the apertures.

The analytical result of Equation 7.39 is validated by calculating the transverse electric field patterns at increasing distances from a 100 particle GA spiral array (Figure 7.4). Figure 7.4 (a) corresponds to a sub-wavelength distance from the array and correctly reproduces the GA spiral geometry in the near field zone, since no Fresnel approximation was introduced in our general diffraction model. As generally expected, Figure 7.4 shows that when the scattered fields propagate away from the array plane, the spatial resolution of the fields is gradually lost and the field profiles approach the analytically calculated far field solution shown in Figure 7.4 (d). This result completes the analytical model for light scattering by arbitrary Vogel spiral arrays. In the next section, a brief discussion is presented on an alternative analytical formulation that improves the efficiency in the numerical implementation of the proposed model.

7.4.1 Notes on Numerical Implementation

It is worth noticing that the computational complexity of Equation 7.39 can be further reduced by expressing the Bessel function J_0 in terms of the generalized hypergeometric series:

$$J_\alpha(x) = \frac{(\frac{x}{2})^\alpha}{\Gamma(\alpha+1)} {}_0F_1(\alpha+1; \frac{-x^2}{4}) \tag{7.40}$$

with,

$${}_pF_q(a_1,...,a_p;b_1,...,b_q;z) = \sum_{n=0}^{\infty} \frac{(a_1)_n ... (a_p)_n}{(b_1)_n ... (b_q)_n} \frac{z^n}{n!} \tag{7.41}$$

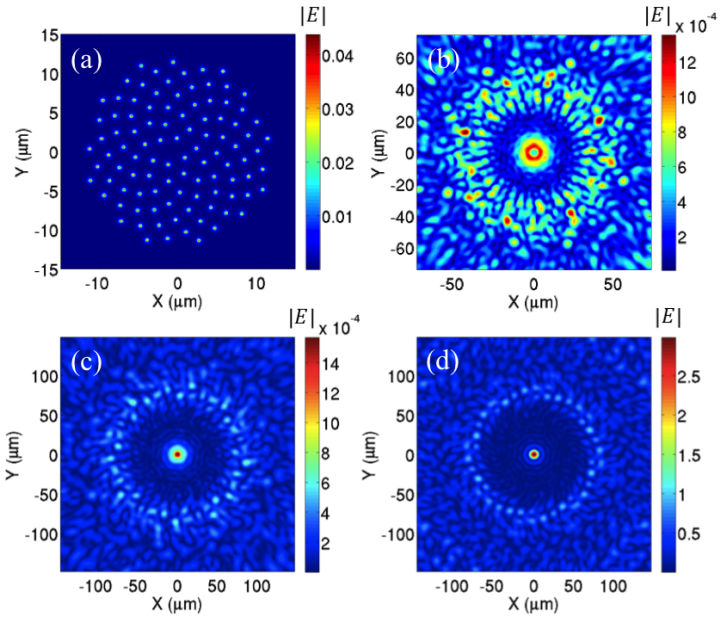

Figure 7·6: (a,b,c) Electric field pattern of radiation at 633nm from a GA spiral array (100 particles, $a_0 = 1.2\mu m$) of circular apertures of radius 100nm at propagation distances of 0.2 λ, 100 λ and 400 λ, respectively. (d) Far field radiation pattern of the same GA spiral array shown in (a,b,c) for comparison.

Where the Pochhammer symbol has been used,

$$(a)_n = a(a+1)(a+2)...(a+n-1),\ (a_0) = 1 \tag{7.42}$$

for the rising factorial. Using the hypergeometric representation, the expression for the scattered field becomes,

$$E(r,\theta;d) = 2\pi a E_0 \sum_{n=1}^{N}\sum_{m=1}^{\infty} \frac{R^{2m}}{(m!)^2} \int_0^{\infty} e^{j2\pi d\sqrt{\frac{1}{\lambda^2}-\nu_r^2}} (-1)^m (\frac{(2\pi\nu_r)^2}{4})^m J_1(a2\pi\nu_r) d\nu_r. \tag{7.43}$$

The integrand in Equation 7.43 depends now only on ν_r. This fact significantly speeds up the evaluation of the transverse field profile with respect to the expression in Equation 7.39, since the integrand factor in Equation 7.39 is also dependent on the spatial (r,θ) grid values through the dependence on the parameter R.

7.5 Conclusions

In conclusion, a general analytical diffraction model for light scattering by arbitrary arrays of circular apertures is developed. This method has been used to study the light scattering of Vogel spirals illuminated at normal incidence by a plane wave. To study the generation of OAM by Vogel spirals an analytic expression for the Fourier-Hankel transform of the scattered field is explicitly derived. The form of this expression is studied to determine how particular azimuthal values of generated OAM are linked to the irrational number used for spiral generation. It is shown that by expressing the irrational generation number with a continued fraction expansion, the azimuthal numbers of generated OAM are given by the denominators of the rational approximants of the generation number. This provides a method for the generation of complex sequences of OAM, including OAM with large azimuthal values, using aperiodic Vogel spiral arrays by the changing of a single geometrical parameter. Additionally, the analytic formulation

is used to explore how the particle number and far-field aperture affect the transmitted OAM spectrum. Finally, the method is extended to include the complex scattered field at an arbitrary distance away from the array and the evolution of far-field radiation patterns is studied. These findings open novel opportunities for the manipulation of complex OAM spectra by exploiting light scattering by aperiodic spiral arrays.

Chapter 8

Measurement of Orbital Angular Momentum

8.1 Introduction

While the fact that light carries linear momentum and spin has been long established, the possibility for optical fields to carry orbital angular momentum (OAM) has more recently been realized(Allen et al., 1992; Allen et al., 2003; Padgett et al., 2004). OAM arises through an azimuthal phase dependence of the complex field. Optical OAM has already found multiple uses including rotating optical traps (O'Neil et al., 2002; Grier, 2003), secure optical communication (Gibson et al., 2004; Simon et al., 2013; Mair et al., 2001) and increasing data transfer rates through OAM multiplexing (Wang et al., 2012; Bozinovic et al., 2013). Moreover, recent advances in the detection of light waves carrying multiple OAM values have been achieved (Berkhout et al., 2010). However, the generation of optical waves simultaneously carrying many values of OAM still remains challenging.

The generation of OAM can be achieved by converting Gaussian laser modes to Laguerre-Gaussian (LG) modes which have explicit azimuthal phase dependence. This can be accomplished using a system of cylindrical lenses (Padgett et al., 2004) or spatial

light modulators (SLMs) (Heckenberg et al., 1992). A shematic of light with helical phase fronts is shown in Figure 8·1. Here a phase plate (which could be generated with a SLM) is used to alter the phase fronts of a laser beam and impart OAM. Generation of OAM from planar plasmonic devices has also been demonstrated (Yu et al., 2011; Trevino et al., 2011). SLMs are expensive and the pixel size limits the complexity of patterns that can be created. Additionally, all of the aforementioned methods are limited to creating states of light with only a few OAM values. Here we demonstrate a method for the simultaneous generation of a large number of superimposed OAM states by light scattering from Vogel spirals of metallic nanoparticles on a planar substrate.

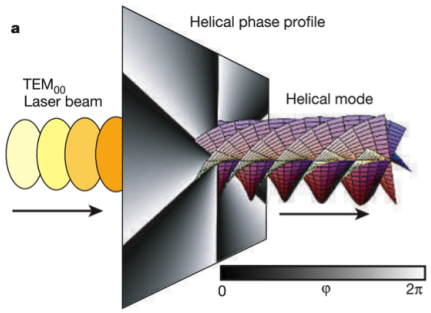

Figure 8·1: Schematic of light with a helical phase front generated with an optical phase plate. (Grier, 2003).

In the pervious chapter, it was shown analytically that the far-field scattering from Vogel spirals encodes OAM with a sequence of azimuthal numbers determined by the spiral divergence angle (Dal Negro et al., 2012). It has also been shown that the eigenmodes of Vogel spiral dielectric pillar arrays carry OAM (Liew et al., 2011). In this chapter, the generation of OAM sequences from Vogel spirals is experimentally demonstrated using phase stepped interferometric measurements to recover the complex optical field of scattered radiation, (Yamaguchi et al., 2002; Barsi et al., 2009) and modal decomposition to explore its OAM content(Chavez-Cerda et al., 2002). The controlled generation of OAM from planar devices has potential for applications in secure optical communication(Simon et al., 2013).

8.2 Phase Shifting Interferometry

Interference measurements are commonly used to detect OAM of Laguerre-Gauss modes due to the formation of distinctive fringe dislocations, or spirals patterns. However, for more complex field patterns, containing simultaneously OAM with many azimuthal values, numerical decomposition of the field into modes carrying OAM is required. The analysis of OAM in the scattered light from Vogel spirals presented in Chapter 7 relies on use of the Fourier-Hankel decomposition (FHD) to analyze the complex scattering pattern generated by the arrays. This technique can be applied to experimental data as well, however it requires knowledge of the complex electric field value not just the intensity. A single interference measurement is not sufficient to determine phase, however by taking multiple interferograms, while varying the phase offset of a reference beam, the phase of a signal can be determined. This technique, referred to as phase shifting interferometry (PSI) (Malacara, 1992), is explained in detail in this section.

Consider two wavefronts, called the signal and reference, with complex field given by,

$$E_{sig}(\vec{r}) = A_{sig}(\vec{r})e^{j\phi_{sig}(\vec{r})} \tag{8.1}$$

$$E_{ref}(\vec{r},V) = A_{ref}(\vec{r})e^{j(\phi_{ref}(\vec{r})-\phi_{off}(V))} \tag{8.2}$$

respectively, where $A(\vec{r})$ is the amplitude of the field, $\phi(\vec{r})$ is the phase and $\phi_{off}(V)$ is a phase offset dependent on the arbitrary input V, who's name choice will become apparent. The measured intensity of the resulting interference pattern, $I(\vec{r},V) = |E_{sig}(\vec{r}) + E_{ref}(\vec{r},V)|^2$, can be expressed as

$$I(\vec{r},V) = I_1(\vec{r}) + I_2(\vec{r})cos(\phi(\vec{r}) + \phi_{off}(V)) \tag{8.3}$$

where, $I_1(\vec{r}) = A_{sig}(\vec{r})^2 + A_{ref}(\vec{r})^2$, $I_2(\vec{r}) = 2A_{sig}(\vec{r})A_{ref}(\vec{r})$, and $\phi(\vec{r}) = \phi_{sig}(\vec{r}) - \phi_{ref}(\vec{r})$.

A schematic of $I(\vec{r}, V)$ is shown in Figure 8·2. As ϕ_{off} varies a sinusoidal intensity signal is seen, from which the relative phase between the reference and signal beams, $\phi(\vec{r})$, can be determined.

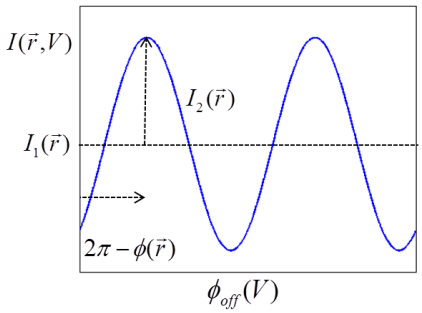

Figure 8·2: Schematic of interference signal from a CCD pixel taken with varying phase of the reference beam.

The experimental set up used is shown in Figure 8·3. A HeNe laser (632nm) is first sent through a beam splitter to create a signal and reference arm. The signal beam is focused onto the sample in transmission and the scattered light is collected using a 50X (NA=.75) microscope objective. The collected light is then imaged on a CCD camera. In this configuration the signal beam is a direct space image of the laser incident on the array, but with the addition of one more lens in the beam path after the objective, the Fourier transform of the scattered light can formed on the CCD, showing the far-field radiation pattern form the array. The reference beam is reflected off of two mirrors mounted on a piezo controlled stage and then passed through a beam expander. It is then reflected onto the CCD along with the signal beam, using a beam splitter. By varying the voltage of the piezo stage, V, the phase offset of the reference beam, $\phi_{off}(V)$, can be controlled.

To collect data, multiple images are taken with the CCD camera as the voltage of the piezo stage is linearly increased, providing interference images at many different phase offsets, $\phi_{off}(V)$. The hypothetical signal shown in Figure 8·2 corresponds then to the

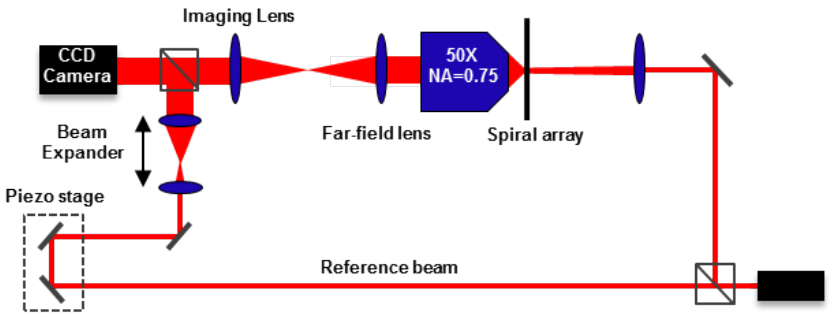

Figure 8·3: Schematic of the experimental setup used for phase shifted interfermetry.

intensity at one point on the CCD camera over multiple images. By fitting this signal to a sinusoid, the relative phase, $\phi(\vec{r})$, can be recovered. In practice, taking the Fourier transform of the data for a single pixel is much faster than fitting with a sinusoid and achieves the same result. In this case, $\phi(\vec{r})$ is determined using the shift property of the Fourier transform, $f(t+t_0) \Leftrightarrow F(\omega)e^{j\omega t_0}$. Which, when written explicitly for $I(\phi_{off})$ gives,

$$F[I(\phi_{off}+\phi(\vec{r}))] = \mathcal{I}(\Phi_{off})e^{i\Phi_{off}\phi(\vec{r})} \tag{8.4}$$

where $(\mathcal{I}, \Phi_{off})$ are the transform variables of (I, ϕ_{off}). $\phi(\vec{r})$ is then calculated from $Arg(\mathcal{I}(\Phi_{off,max}))$, the argument of the complex Fourier transform at the point of maximum intensity, assuming the sinusoidal modulation from phase variation dominates other spectral noise.

One limitation to this measurement method, not yet discussed is that only the phase of the signal beam relative to the reference beam can be recovered. Ideally then, a reference beam of constant phase would be used. Since this is not possible, the reference beam has been expanded to reduce its phase fluctuations as much as possible. To test what limitations this may have on the measurement of OAM generated in Vogel spirals, simulated experimental results have been analyzed in the next section to explore serval possible types of experimental error.

8.2.1 Robustness of OAM Sequences to Experimental Errors

To show that the generation of OAM with Vogel spirals, and measurement with PSI, is a robust process, the effect of three different types of experimental errors are investigated here. First, the issue of phase distortions in the measured field is explored, arising from the use of a non-uniform reference beam in the PSI measurements. Second, the effect of random fluctuations in the phase is studied, that could result from or experimental noise. Finally, the effect of random variation in the particle positions is considered which could arise from fabrication errors. This analysis will show that the generation and measurement of OAM sequences is a very stable feature of a diffracted optical beam.

The first type of error that is addressed can be caused by the use of a non-uniform reference beam in the recovery of the phase information. Experimentally, the phase of the scattered light is recovered relative to the phase of the reference beam. Since it is practically impossible to create a beam of constant phase over the large area of the detector, which would allow to phase recovery to an arbitrary constant offset, a Gaussian beam is used. The Gaussian beam introduces a circularly symmetric phase variation to the data. Figure 8·4 (a) shows the phase of the calculated far-field radiation from an ideal golden angle (GA) spiral and the corresponding Fourier-Hankel decomposition (FHD) of this field demonstrating peaks in the OAM at azimuthal numbers corresponding to the Fibonacci sequence, Figure 8·4 (e). Figure 8·4 (b) shows the phase of a reference Gaussian beam with propagation axis parallel to the axis of the scattered light from the GA spiral. The FHD of the measured field using this reference beam is shown in Figure 8·4 (f) where the azimuthal numbers of the OAM are preserved. This corresponds to the best experimental scenario when using a Gaussian reference beam. On the other hand, Figure 8·4 (c,d) shows the phase of a reference beam with propagation axis tilted at an angles of 0.8° and 2.4° relative to the axis of the scattered light. The FHD of the measured field using the tilted reference beams is shown in Figure 8·4 (g,h), where the

change in phase has caused a spreading of the expected peaks. In conclusion, as long as the propagation axis of the reference Gaussian beam is parallel to the optical axis the azimuthal numbers of the OAM peaks are preserved.

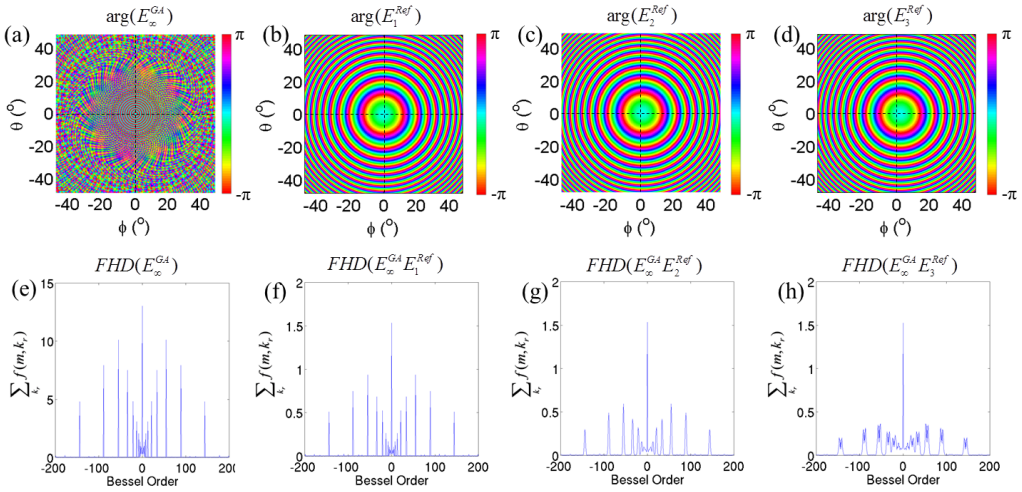

Figure 8·4: (a) Phase of the far-field radiation from a golden angle (GA) spiral. (b,c,d) Phase of a gaussian reference beam with propagation axis tilted by 0°, 0.8° and 2.4°, with respect to the origin, respectively. (d) Fourier-Hankel decomposition (FHD), summed over radial wavevector k_{r}, for the far-field radiation from a GA spiral. (e,f,g) FHD of the recovered phase of a GA spiral far-field using respective reference beams.

The second type of error simulated is random fluctuations in phase which could arise from experimental noise. To test this, random noise has been added to the phase of the calculated far field radiation. Figure 8·5 (a,e) shows, respectively, the phase of the far field radiation produced by a GA spiral and the corresponding FHD of the field with peaks in the OAM at azimuthal numbers corresponding to the Fibonacci sequence. In Figure 8·5 (b-d) random noise has been added to the phase of each pixel. A number chosen from a uniform random distribution over the interval $[0, \pi]$, $[0, 1.6\pi]$ and $[0, 1.8\pi]$, respectively for Figure 8·5 (b-d), has been added to the phase of the calculated radiation in Figure 8·5 (a). The FHD of each complex field is shown in Figure 8·5 (f-h). As the amplitude of the random phase modulation increases the noise background increases

relative to the height of the peaks, though the values of the peaks do not shift or broaden. This analysis shows that the OAM content of the far field radiation is robust with respect to random phase variations.

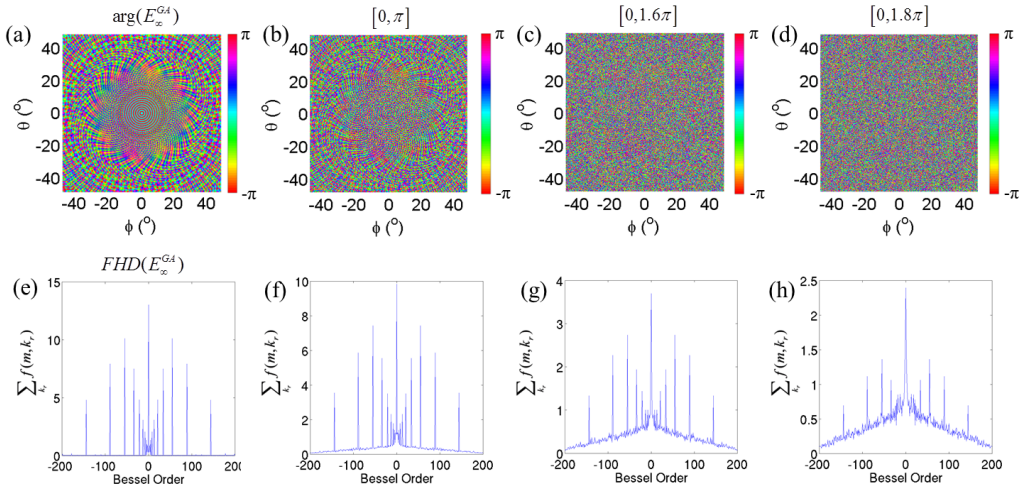

Figure 8·5: (a) Phase of the far-field radiation from a golden angle (GA) spiral. (b,c,d) Phase of the GA spiral far-field radiation modified by a random phase shift. The phase shift for each pixel is chosen with a random uniform distribution to lie on the interval $[0, \pi]$, $[0, 1.6\pi]$ and $[0, 1.8\pi]$ respectively. (d) Fourier-Hankel decomposition (FHD), summed over radial wavevector k_{r}, for the far field radiation from a GA spiral. (e,f,g) FHD of the respective randomized GA spiral far field.

Finally, the effect of random errors in the positions of the particles is studied, which could arise from fabrication errors. Once again, the phase of far field radiation and FHD of complex field for the ideal structure are presented in Figure 8·9 (a,e) for comparison. To introduce random fabrication error, the position of each particle is varied in x and y with displacement uniformly chosen on the interval $[0, .3a_0]$, $[0, .7a_0]$ and $[0, 1.1a_0]$, respectively, where a_0 is the scaling factor of the array. The phase of far-field radiation from these arrays is shown in Figure 8·6 (b-d). The corresponding FHD of the complex field in shown in Figure 8·6 (f-h). As the positional disorder of the particles increases the background in the FHD increases, the amplitude of the peaks decreases and the

peaks broaden in azimuthal number. This analysis shows that a very large fluctuation in the particle positions, with respect to their spacing, would be needed to significantly alter the OAM content of the far field radiation, which is not the case experimentally.

In conclusion, the robustness of the generation of OAM using Vogel spirals, and measurement with PSI is studied, with respect to different types of experimental and fabrication errors. It is shown that while use of a properly aligned Gaussian reference beam will preserve OAM peaks, a tilted Gaussian reference beam can significantly broaden the measured OAM peaks. Uniformly distributed random noise of varying amplitude has been introduced and it is shown that the measurement of OAM is still possible in the presence of large amounts of noise. Finally, the effect of random positional errors of individual nanoparticles is studied and it is shown that large errors would be needed to disrupt the generation of OAM.

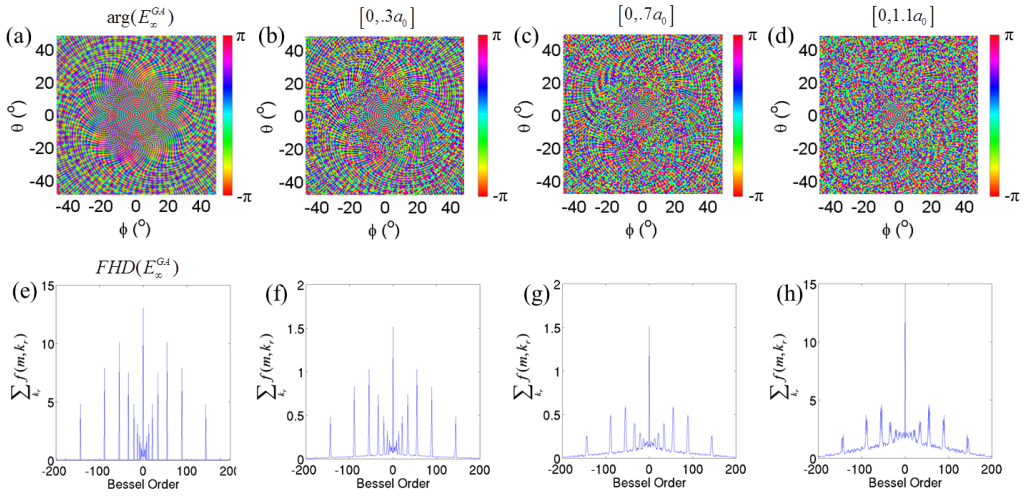

Figure 8·6: (a) Phase of the far-field radiation from a golden angle (GA) spiral. (b,c,d) Phase of the GA spiral far-field radiation when the particles are modified by a random shift in position. The position shift for each particle in x and y is chosen with a random uniform distribution to have an amplitude on the interval $[0, .3a_0]$, $[0, .7a_0]$, $[0, 1.1a_0]$, respectively where a_0 in the scaling factor of the array. (d) Fourier-Hankel decomposition (FHD), summed over radial wavevector k_r, for the far-field radiation from a GA spiral. (e,f,g) FHD of the respective randomized GA spiral far-field.

8.3 OAM in Scattered Light from Vogel Spirals

In this section, the results of experimental measurements of OAM from Vogel spirals are presented. To measure OAM the technique described in Section 8.2 has been used to recover the complex field of far-field radiaton patterns followed by numerical Fourier-Hankel decomposition of the measured field. Vogel spiral arrays consist of N particles with polar positions (r_n, θ_n) given by,

$$r_n = a_0\sqrt{n} \tag{8.5}$$

$$\theta_n = n\alpha \tag{8.6}$$

where a_0 is the scaling factor and α is the divergence angle. Though this formulation can be used to describe any arbitrary Vogel spiral pattern, this section focuses on two arrays, the Golden Angle (GA) or ϕ and μ spirals defined by irrational numbers $\phi = \frac{1+sqrt5}{2}$ and $\mu = \frac{5+\sqrt{29}}{2}$, respectively. The GA spiral is chosen as it is the primary example of a Vogel spiral and it has been largely studied in the literature (Trevino et al., 2011; Liew et al., 2011; Lawrence et al., 2012; Dal Negro and Boriskina, 2012; Trevino et al., 2012; Vogel, 1979; Mitchison, 1977). The μ spiral is chosen to demonstrate that the proposed general method can be applied to other Vogel spirals, providing the opportunity to encode different sequences of OAM values. According to the theory presented in Section 7.3, these spirals should generate significantly different sequences of OAM azimuthal values.

Arrays of gold nanoparticles on fused silica are fabricated using electron beam lithography, metal evaporation and lift-off processing. SEMs of fabricated arrays are shown in Figure 8.3 (a,d). Square samples of fused silica are made by dicing a wafer into 1cm^2

pieces, which are then cleaned in Piranha etchant ($3H_2SO_4 : 1H_2O_2$) for 2 minutes. A thin layer of PMMA is then deposited on the substrate by spin coating to be used as a positive tone electron beam resist. Selective areas of the sample are then exposed to create the Vogel spiral pattern using a scanning electron microscope (Ziess Supra 40VP) and beam blanker. Exposed areas are developed using a mixture of methyl isobutyl ketone and isopropyl alcohol (1 MIBK : 3 IPA) and the sample is cleaned for 30sec to remove small amounts of leftover PMMA in the developed areas, using an O_2 plasma. A thin (30nm) layer of gold is then deposited by electron beam evaporation with a 2nm Cr layer to help adhesion to the substrate. The remaining PMMA and excess gold are removed by liftoff process in acetone.

Using the derivation for the far-field radiation pattern from Vogel spirals, presented in Section 7.2.2, the intensity of far-field radiation scattered from GA and μ spirals is plotted in Figure 8.3 (b,e). Using the optical setup described in Section 8.2 measured far-field radiation intensity patterns for GA and μ spirals are plotted in Figure 8.3 (c,f) respectively. The calculated and measured images show good agreement inside the region between the superimposed white circles. Inside the inner circle, the signal is dominated by transmitted light, not scattered by the array. Outside the outer circle the numerical aperture (NA) of the optical system prevents the collection of light. Therefore, in order to correctly study the propagation of scattered radiation, the analysis is limited to the annular regions bounded by the circles in Figure 8.3 (b,c,e,f). Measurement of the phase of the far-field radiation is accomplished using the method described in Section 8.2, by scanning the phase of a reference beam and measuring the interference patterns on a CCD camera. The analytically calculated phase of the far field radiation from GA and μ spirals is shown in Figure 8.3 (a,b), respectively. The measured phase from a GA spiral is shown in Figure 8.3 (c) and the phase from a μ spiral is shown in Figure 8.3 (d).

Modal decomposition can be used to analyze a superposition of OAM carrying modes

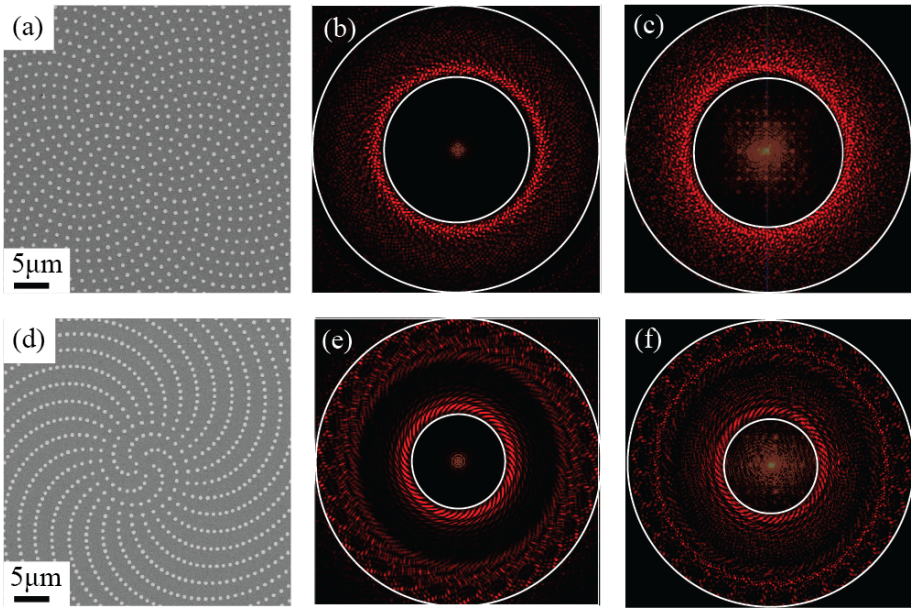

Figure 8·7: (a,d) SEMs of GA and μ spirals respectively composed of 500nm diameter gold nanoparticles on fused silica. (b,e) Analytically calculated far field intensity (a,d) at 633nm. (c,f) Experimentally measured far field radiation pattern from (a,d) respectively at 633nm. White circles denote region where scattered light intensity is dominant.

in the far-field pattern and determine their relative intensities(Chavez-Cerda et al., 2002). Decomposition into a basis set with azimuthal dependence, is accomplished through Fourier-Hankel decomposition (FHD) according to

$$f(m,k_r) = \frac{1}{2\pi}\int_0^{\infty}\int_0^{2\pi} r dr d\theta E_{\infty}(r,\theta) J_m(k_r r) e^{im\theta} \tag{8.7}$$

where J_m is the m_{th} Bessel function. In this decomposition the m_{th} order function carries OAM with azimuthal number m, this can accommodate positive and negative integer values for m. Since the focus here is the azimuthal component of the field, $f(m,k_r)$ can be summed over radial wavevectors k_r. In Figure 8·9 (a,b) the summed FHD of the calculated far field radiation from GA (ϕ) and μ spirals are shown, respectively. Both show peaks at azimuthal numbers corresponding to the denominators of the rational approximations (i.e., convergents) of the irrational numbers used to generate the spirals,

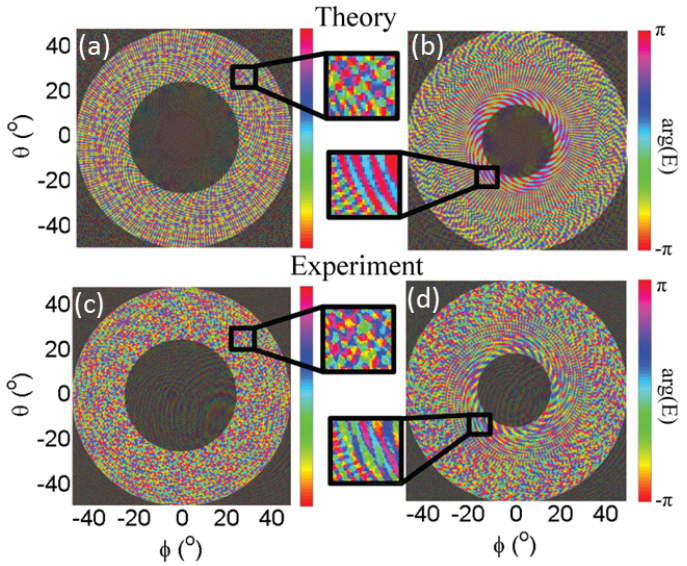

Figure 8·8: (a,b) Analytically calculated phase portrait of far field radiation from GA and μ spirals respectively. (c,d) Experimentally measured phase portrait from GA and μ spirals respectively. Shaded area indicates region where scattered field intensity is too low to measure phase accurately. These regions are ignored during FHD.

as previously discussed in Section 7.3. For the GA spiral this encodes the Fibonacci sequence in the OAM spectrum. The μ spiral has significantly fewer convergents in the region of interest, however some OAM peaks are observed at linear combinations of convergents. These peaks can be reduced with aperturing of the beam, as discussed in Section 7.3.

Now the OAM content of the experimentally measured scattered radiation is examined. The complex field, reconstructed based on the measured far -ield intensity (Figure 8.3 (c,d)) and recovered phase (Figure 8.3 (c,d)), is decomposed according to Equation 8.7. The shaded areas superimposed on Figure 8.3 (a-d) denote the limits where measurement of the scattered light is accurate as discussed with respect to Figure 8.3. In Figure 8·9 (c) the radially summed FHD is plotted for the GA spiral and

Measurement	FHD Peaks
GA spiral Analytic	3,5,8,13,21,34,55,89,144
GA spiral Experimental	5,8,13,21,34,55,89,145
μ spiral Analytic	5,10,21,26,31,52,109,135,161
μ spiral Experimental	5,10,26,52,109,135,161

Table 8.1: Fourier-Hankel decomposition peaks.

peaks in the transform are observed at numbers corresponding to the Fibonacci sequence. In Figure 8·9 (d), peaks are observed that match the theoretically predicted values for the μ spiral. The full list of FHD peak positions for both the analytically calculated and the experimentally measured far fields are listed in Table 8.3 (negative peaks have been ignored as they mirror the positive ones). The experimentally measured peaks are slightly broader than the theoretical peaks, which is attributed to non-ideal centering of the Gaussian reference beam with the axis of the OAM measurements, the effect of which is discussed in detail in Section 8.2.1. To reduce this effect, great care has been taken in aligning the reference and signal beams and the reference beam has been expanded in order to reduce the curvatures of its wavefronts.

8.4 OAM in Photoluminescence

In this section, the direct generation of OAM in the emitted light from Vogel spiral arrays of Er:SiN_x nanopillars is studied. The array investigated here is from the samples previously studied in Chapter 6. By combining fluorescence imaging, 2D finite element method (FEM) eigenmode calculations, and Fourier-Bessel decomposition of optical modes, the azimuthal structure of the Er radiation is explored. The coupling of Er emission to distinctive optical resonances of the GA spirals carrying OAM val-

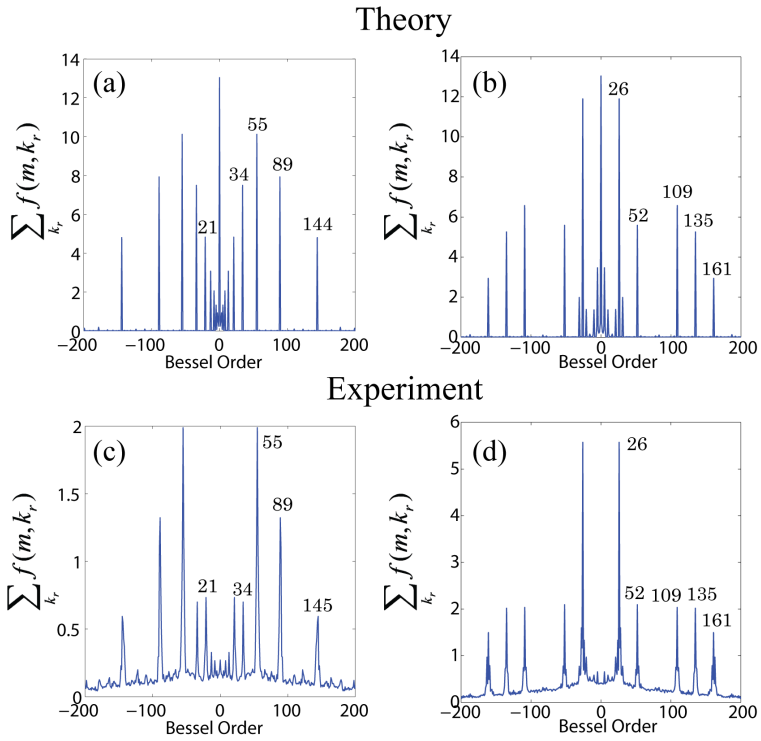

Figure 8·9: Fourier-Hankel decomposition, summed over radial wavevector, for GA spirals (a,c) and μ spirals (b,d). In (a,b) FHD is performed using the analytically calculated far-field, while in (c,d) FHD is performed using the experimentally measured far-field.

ues, discretized in consecutive Fibonacci numbers, is demonstrated. The Er emission patterns were imaged using the setup schematized in Figure 6·5 (a) where the fiber-coupled detector was replaced by an infrared CCD camera. A representative example of experimentally measured Er emission patterns is shown in Figure 8·10 (a) for the case of a GA spiral array with $0.6\mu m$ pillar spacing. This emission pattern is an incoherent mixture of several distinct modes supported by the array geometry within the spectral range of Er emission. In order to identify these modes, a two-dimensional GA spiral array of dielectric cylinders with an effective refractive index (n_{eff}=1.7) is considered. FEM eigenmode analysis is performed on a large-scale structure (5047 cylinders) using COMSOL. The GA spiral eigenmodes are calculated within the spectral range of Er

emission and two of these modes, respectively at wavelengths of 1.510 μm and 1.549 μm, are superimposed in Figure 8·10 (b). The first mode in Figure 8·10 (b) is radially confined near the outer edge of the array while the second mode, which shows two intensity peaks in the radial direction, is confined in the internal array region halfway between the center and outer edge. Localized modes have been predicted at the multifractal bandedge of GA spirals, and several different classes of bandedge modes were recently discovered and classified according to well-defined azimuthal and radial numbers(Trevino et al., 2012). Information on the radial localization of these modes can be obtained by performing a Delaunay triangulation of the GA spiral array, as shown in Figure 8·10 (c). The Delaunay triangulation is a geometrical technique that allows one to picture the spatial distribution of first neighboring particles in the arrays, as recently discussed in (Trevino et al., 2012). In this analysis, neighboring particles are connected with line segments that are color-coded according to their length. Therefore, this analysis provides a spatial map of the local correlation lengths present in the GA spiral array. Figure 8·10 (c) shows distinct circular regions, positioned at different radial locations, on the GA spiral. These regions provide confinement for different series of localized band-edge modes effectively behaving as *circular grating structures* that trap radiation within circular bands of well-defined radial positions.(Liew et al., 2011; Trevino et al., 2012) This can be observed by comparing Figure 8·10 (b,c), which shows that the radial positions of the modes contributing to the Er emission closely correspond to the circular regions in the Delaunay spatial map in Figure 8·10(c). (i.e., first and second green regions in the Delaunay triangulation map, from the outside towards the center).

Similarly to the rest of this chapter, analysis of the OAM content of the emitted light is investigated using Fourier-Hankel decomposition (FHD) according to Equation 8.7. To apply FHD, the phase of the light is required, in addition to the intensity. Since the light emitted by photoluminescence comes from a large number of incoherent sources, it

is not possible to use the interferometric phase retrieval technique as was done previously in this chapter. To investigate the OAM content, FHD is applied to the complex electric field from the eigenmode calculations shown in Figure 8·10 (b). Since this analysis is mostly concerned with the azimuthal components of the fields, Figure 8·10 (d) shows the sum of $f(m, k_r)$ over a range of wavenumbers k_r between $0.5 \times (2\pi/d_0)$ and $1.5 \times (2\pi/d_0)$, where d_0 is the average nearest neighbor spacing. The results of this modal decomposition features several discrete azimuthal components in the optical field at values corresponding to 5 consecutive Fibonacci numbers (i.e., 21, 34, 55, 89 and 144). These results demonstrate that the optical resonances of GA spiral arrays are excited by the Er emission at 1.55 μm and carry geometry-induced OAM values discretized in consecutive Fibonacci numbers.

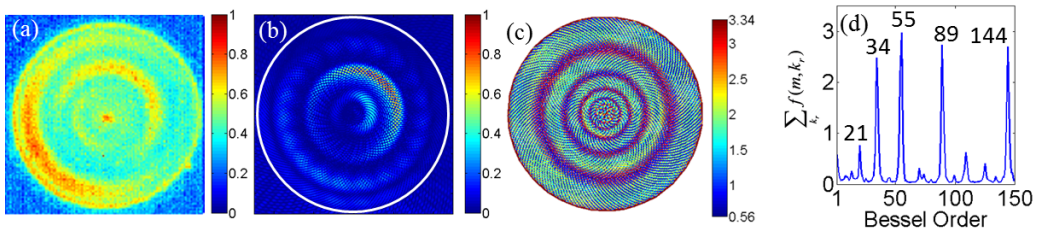

Figure 8·10: (a) Photoluminescence image of GA spiral array with 0.6 μm spacing. (b) 2D FEM mode calculations of identical GA spiral array showing the sum of two modes at wavelengths of 1.510 μm and 1.549 μm. (c) Delaunay triangulation of GA spiral showing spatial correlation of neighboring particles with colorbar units in microns. (d) Fourier-Bessel transform of the mode intensity that is shown in Figure 6b summed over wavevector k_r ranging from, $0.5 \times (2\pi/d_0)$ to $1.5 \times (2\pi/d_0)$, where d_0 is the average nearest neighbor spacing.

8.5 Conclusions

In conclusion, in this chapter an experimental demonstration is provided of the generation of long sequences of azimuthal OAM values using light scattering from Vogel spirals. First, the phase shifting interferometric technique used to recover the complex

far-field radiation is explained in detail. The robustness of OAM measurements using this technique are investigated with respect to possible experimental errors. Vogel spiral arrays of gold nanoparticles are fabricated and the complex field of scattered light is measured experimentally. Fourier-Hankel decomposition is used to examine the OAM content of the scattered far-field radiation and the generation of OAM is shown to be in good agreement to predictions based on analytical theory. Finally, photoluminescence from Vogel spiral arrays of Er:SiN_x nanopillars is investigated experimentally and compared to eigenmode calculations of Vogel spiral structures. Directly excited eigenmodes in Vogel spiral arrays are also shown to carry OAM. The superposition of many OAM modes demonstrated in this work can provide novel exciting opportunities for secure optical communication.

Chapter 9

Conclusions

9.1 Summary of Work

In the first section of this work, plasmonic nanostructures are designed, fabricated and characterized which exhibit radiative rate enhancement at $1.55\mu m$. Beginning in Chapter 3, a detailed derivation of the electromagnetic properties of concentric multilayered cylinders has been shown using a Mie theory type approach in 2D. This method is used to calculate the electromagnetic response of multilayered cylinders to a plane wave excitation and the calculation of scattering cross section is discussed. The same method is then used to calculate the response of a multilayered cylinder to a point source excitation allowing for investigation of changes in the local density of photonic states.

In Chapter 4, theoretical studies of multilayered cylinders have been presented, using the computational method presented in Chapter 3. Deep subwavelength plasmon modes in coaxial plasmonic nanowires (CPNs) are investigated by studying the near-field enhancement, scattering/absorption spectra, energy flow and PDOS. Multiple resonances in CPNs are found to strongly increase the local electromagnetic field and PDOS across wide wavelength bands. A systematic study of the resonant behavior with changes in geometrical device parameters is presented, showing how CPNs can be engineered for different applications and giving insight into the physical mechanism leading to plasmon mode formation. Multilayered cylinders composed of purely dielectric materials are studied and field confinement is shown in deep subwavelength low index gap regions.

The localized modes found in dielectric devices could be used for light confinement, as an alternative to plasmon formation, but with low loss. A fabrication method for multilayered pillars is presented which uses top-down lithography to make high aspect ratio Si pillars followed by conformal sputtering to make multilayered structures. Scattering measurement of both bare and multicoated pillars are performed and compared to analytical theory. While the scattering of bare Si pillars is in excellent agreement with calculations, the scattering of multilayered dielectric pillars is not as well captured by 2D simulations. Measurements have not conclusively shown the formation of highly confined modes in multilayered dielectric pillars. Work in this area is ongoing.

To overcome the difficulties associated with the fabrication and testing of high aspect ratio plasmonic cylinders, novel nanostructures are developed which support similar plasmon modes called plasmonic ring nanocavities. The design, fabrication and characterization of plasmonic ring nanocavities composed of Er:SiO_2 and silver is shown in Chapter 5. Here, the excitation of gap plasmons creates deep subwavelength light confinement in cavities with volumes as small as $0.01\left(\frac{\lambda}{n}\right)^3$. The geometry of the cavity is varied to maximize the overlap of the cavity resonance with the spontaneous emission of Er and the total decay rate of Er atoms is increased 20 times at room temperature. Through measurements of photoluminescence intensity, PL time-dynamics and full-vector FDTD modeling of the fabricated device structures, the enhancement of the radiative decay rate is quantified in a number of nanocavity devices which demonstrate up to 25-times radiative rate enhancement and a doubling of the quantum efficiency. Finally, the possibility of achieving Purcell-enhanced lasing is studied and it is shown that plasmonic ring nanocavities are a promising platform for Er based subwavelength sources.

In the second section of this thesis, photonic devices are designed, fabricated and characterized for the enhancement of extraction efficiency, control of radiation patterns

and generation of OAM. Chapter 6 shows the engineering of aperiodic active devices with a high degree of rotational symmetry in Fourier space for omnidirectional extraction and emission profile shaping. Aperiodic pillar arrays of Er:SiN_x are fabricated using silicon based planar processing for efficient light extraction at 1.55 μm. Structural optimization of pillar height and array geometry is performed using FDTD simulations and Bragg scattering calculations. Devices of different array geometry and pillar spacing are optically characterized with PL spectroscopy and extraction enhancement of over 10 times is demonstrated for GA spiral arrays, outperforming both Archimedean and Pinwheel arrays. The angular emission profiles are measured, demonstrating azimuthally isotropic emission in GA spiral structures. These findings offer unique opportunities for the engineering light extraction while maintaining azimuthally isotropic emission patterns.

In Chapter 7 a general analytical diffraction model for light scattering by arbitrary arrays of circular apertures is developed. This method is used to study the light scattering of Vogel spirals illuminated at normal incidence by a plane wave. To study the generation of OAM by Vogel spirals an analytic expression for the Fourier-Hankel transform of the scattered field is explicitly derived. The form of this expression is studied to determine how particular azimuthal values of generated OAM are linked to the irrational number used for spiral generation. It is shown that by expressing the irrational generation number with a continued fraction expansion, the azimuthal numbers of generated OAM are given by the denominators of the rational approximants of the generation number. This provides a method for the generation of complex sequences of OAM, including OAM with large azimuthal values, using aperiodic Vogel spiral arrays by the changing of a single geometrical parameter. Additionally, the analytic formulation is used to explore how the particle number and far-field aperture affect the transmitted OAM spectrum. Finally, the method is extended to include the complex scattered field

at an arbitrary distance away from the array and the evolution of far-field radiation patterns is studied. These findings open novel opportunities for the manipulation of complex OAM spectra by exploiting light scattering by aperiodic spiral arrays.

In Chapter 8 an experimental demonstration is provided of the generation of long sequences of azimuthal OAM values using light scattering from Vogel spirals. First, the phase shifting interferometric technique used to recover the complex far-field radiation is explained in detail. The robustness of OAM measurements using this technique are investigated with respect to possible experimental errors. Vogel spiral arrays of gold nanoparticles are fabricated and the complex field of scattered light is measured experimentally. Fourier-Hankel decomposition is used to examine the OAM content of the scattered far-field radiation and the generation of OAM is shown to be in good agreement to predictions based on analytical theory. Finally, photoluminescence from Vogel spiral arrays of Er:SiN_x nanopillars is investigated experimentally and compared to eigenmode calculations of Vogel spiral structures. Directly excited eigenmodes in Vogel spiral arrays are also shown to carry OAM. The superposition of many OAM modes demonstrated in this work can provide novel exciting opportunities for secure optical communication.

9.2 Future Work

The primary goal of future work on the plasmonic ring nanocavity project is to achieve lasing leveraging Purcell enhancement of optical gain. The analysis conducted in Chapter 5 shows that this can be achieved by a reduction in nanocavity size, increase in the Q factor or a combination of both. Based on the currently fabricated devices, a reduction in the size by a factor of 3 and an increase in the Q factor by 7 times would be sufficient to pass the gain threshold. Reductions in the size are currently limited by the fabrication processing used, similar devices of significantly smaller size have been demonstrated

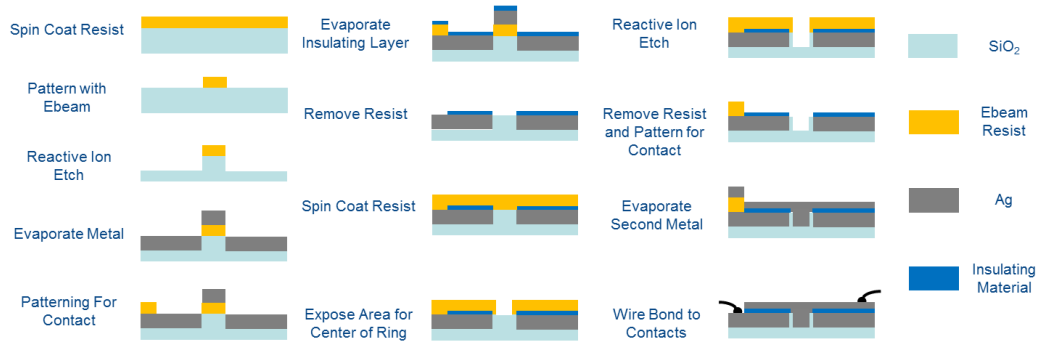

Figure 9·1: Process flow for electrically excited plasmonic ring nanocavities.

using Helium ion lithography(Melli et al., 2013). The resonators demonstrated with this fabrication process however do not incorporate active materials and filling such a small gap with material after fabrication would be quite challenging. It is possible that the addition of focused ion beam techniques could be used along with the current process flow to reduce the size further. Another possible route to achieving lasing is through an increase in the Q factor. Since the Q factor is currently smaller than the spontaneous emission bandwidth, increased Q will not only reduce the cavity loss rate but will increase the Purcell enhancement factor. Once a Q factor of roughly 50 is passed, Purcell enhancement will begin to saturate and further increase in Q factor will only decrease the cavity loss rate. In the nanocavity devices presented in Chapter 5, the Q factor as measured by reflection spectroscopy, is approximately the same as the expected Q factor from FDTD simulations. This indicates that it is intrinsically limited by radiative loss from the cavity or absorption in the metal walls of the cavity and not due limited by imperfection in the fabrication process. To reduce ohmic loss, the metal in the cavity could replaced with a doped transparent conductive material such as Al:ZnO(Naik et al., 2012), having negative permittivity at $1.55\mu m$ with low loss. To reduce radiative loss from the cavity a reflective layer could be placed under the nanocavity such as a thin metal layer or distributed Bragg reflector.

In addition to achieving lasing under optical excitation, it would be desirable to make plasmonic ring nanocavities electrically excited. For any light source to have a technological impact on integrated photonic technology electrical injection of energy is a necessity. Electrically excited Erbium emission has been shown and the plasmonic ring nanocavity has metal sidewalls, readily incorporated to be used as contacts. However, using the current fabrication process the two contacts are shorted. A process flow showing a design for ring nanocavity fabrication that allows for electrical pumping is designed and shown in Figure 9·1. The process starts with the spin coating of electron beam resist on top of a layer of Er active material followed by patterning of a disk shape and transfer of the pattern to the underlying layer using reactive ion etching. This defines the outer side of the ring nanocavity. Next metal is evaporated to form the plasmonic interface on the outside of the cavity and act as one of the electrical contacts. Photoresist is then patterned to protect part of the contact and a layer of insulating material is deposited to isolate the first contact. Next, the remaining resist and unwanted metal are removed by liftoff processing and a second layer of electron beam resist is spin coated on the sample. A second electron beam writing step, aligned to the first, is used to define the inside of the plasmonic cavity and the pattern is again transferred to the underlying layer using reactive ion etching. Another photolithography step is used to protect the first contact and then a second layer of metal is deposited to form the inner plasmonic interface and second electrical contact. The excess metal and remaining photoresist are removed and the two metal contacts can be used to inject current into the ring nanocavity radially. This process is significantly more challenging than the fabrication process used in this thesis, as it requires the alignment of electron beam writing process with high precision. Though this process is challenging, electrically excited nanoscale lasers could have a large impact on future photonics technology.

Appendix A

Code for Multilayer Cylinders

This chapter contains the code developed for calculation of scattering, near-fields and PDOS in multilayered cylinders. The method behind the algorithm is described in Chapter 3.

The algorithm is divided into three functions which has been coded in Matlab. The first algorithm, *Cly2D_ML_coeff.m*, calculates the scattering coefficients, A_n^l and B_n^l, from Equation 3.3. The second, *Cly2D_ML_PW.m*, calculates the scattering cross section, absorption cross section and near-field intensity under planewave excitation, as described in Section 3.2.1. The third algorithm, *Cly2D_ML_PS.m*, calculates the PDOS and local fields under point source excitation, as described in Section 3.2.2.

A.1 Cly2D_ML_coeff.m

```
function [result]=Cly2D_ML_coeff(epsilon,r,nmax,Lambda,source,isPW,SourceDir)
% Nathaniel Lawrence, 2013.
% Written during the completion of my PhD at Boston University

% SourceDir gives the polarization of the source.
% For point source dipole moments 1->x, 2->y, 3->z
% For planewave sources, this should be set by Cly2D_ML_PW.m

%Bessel and Hankel functions are precalculated for speed
global hnk jnk hpnk jpnk hnk1 jnk1 hpnk1 jpnk1 jnk_s hnk_s

%sets polarization for planewaves and point sources
```

```
if not(isPW)
[rsource(2) rsource(1)]=cart2pol(source(1),source(2)); %source location in
    polar
rs=rsource(1);
end
if SourceDir==3
    isEz=1;
else
    isEz=0;
end

M=length(r); %number of layers

index=sqrt(epsilon);
k=index*2*pi/Lambda;

%to change polarization just have to change the boundary conditions being
%satisfied, if e_nmax=epsilon.^(3/2), TM (E-field in z-dir), if
    e_nmax=epsilon.^(-1/2),
%TE (H-field in z-dir)

if isEz==1
    pol=0;
else
    pol=-1;
end

%e_nmax is set to correctly satisfy boundary conditions for different
%polarizations
for nn=1:2*nmax+1
    e_nmax(:,nn)=epsilon.^(pol);
end
e_nmax=squeeze(e_nmax);

%functions which will be used in calculation
if not(isnan(source))
rtemp=[r rs];
```

```
rtemp=sort(rtemp);
slayer=find(rtemp==rs);
end

%now construct the matrix equation which has to be solved
unknowns=zeros(1,2*M,2*nmax+1);
knowns=zeros(1,2*M,2*nmax+1);
matrix=zeros(2*M,2*M,2*nmax+1);

for ii=1:M
    if ii==1 %special case for first layer
        matrix(2*ii-1,2*ii-1,:) = jnk(ii,:);
        matrix(2*ii-1,2*ii,:) = -jnk1(ii,:);
        matrix(2*ii-1,2*ii+1,:) = -hnk1(ii,:);
        matrix(2*ii,2*ii-1,:) = e_nmax(ii,:).*jpnk(ii,:);
        matrix(2*ii,2*ii,:) = -e_nmax(ii+1,:).*jpnk1(ii,:);
        matrix(2*ii,2*ii+1,:) = -e_nmax(ii+1,:).*hpnk1(ii,:);
    elseif ii==M %special case for last layer
        matrix(2*ii-1,2*ii-2,:) = jnk(ii,:);
        matrix(2*ii-1,2*ii-1,:) = hnk(ii,:);
        matrix(2*ii-1,2*ii,:) = -hnk1(ii,:);
        matrix(2*ii,2*ii-2,:) = e_nmax(ii,:).*jpnk(ii,:);
        matrix(2*ii,2*ii-1,:) = e_nmax(ii,:).*hpnk(ii,:);
        matrix(2*ii,2*ii,:) = -e_nmax(ii+1,:).*hpnk1(ii,:);
    else
        matrix(2*ii-1,2*ii-2,:) = jnk(ii,:);
        matrix(2*ii-1,2*ii-1,:) = hnk(ii,:);
        matrix(2*ii-1,2*ii,:) = -jnk1(ii,:);
        matrix(2*ii-1,2*ii+1,:) = -hnk1(ii,:);
        matrix(2*ii,2*ii-2,:) = e_nmax(ii,:).*jpnk(ii,:);
        matrix(2*ii,2*ii-1,:) = e_nmax(ii,:).*hpnk(ii,:);
        matrix(2*ii,2*ii,:) = -e_nmax(ii+1,:).*jpnk1(ii,:);
        matrix(2*ii,2*ii+1,:) = -e_nmax(ii+1,:).*hpnk1(ii,:);
    end
end

%special case of single layer cylinder
```

```
if M==1
    matrix=zeros(2*M,2*M,2*nmax+1);
    matrix(1,1,:) = jnk;
    matrix(1,2,:) = -hnk1;
    matrix(2,1,:) = e_nmax(1,:).*jpnk;
    matrix(2,2,:) = -e_nmax(2,:).*hpnk1;
end

%Sets the source vector
if not(isPW) %for point sources
    n=(-nmax:nmax);
    if SourceDir==3 %z-oriented dipole
        C_in = (hnk_s.*(1/(4*1i))).*exp(-1i.*n.*rsource(2));
        C_out = (jnk_s.*(1/(4*1i))).*exp(-1i.*n.*rsource(2));
    elseif SourceDir==1 %x-oriented dipole
        C_out = ((-1/(8*1i)).*sqrt(epsilon(slayer)).*(jnk_s(1:2*nmax+1).*
            exp(-1i.*(n-1).*rsource(2)) + jnk_s(3:2*nmax+3).*
            exp(-1i.*(n+1).*rsource(2))));
        C_in = ((-1/(8*1i)).*sqrt(epsilon(slayer)).*(hnk_s(1:2*nmax+1).*
            exp(-1i.*(n-1).*rsource(2)) + hnk_s(3:2*nmax+3).*
            exp(-1i.*(n+1).*rsource(2))));
    elseif SourceDir==2 %y-oriented dipole
        C_out = ((1/(8)).*sqrt(epsilon(slayer)).*(jnk_s(1:2*nmax+1).*
            exp(-1i.*(n-1).*rsource(2)) - jnk_s(3:2*nmax+3).*
            exp(-1i.*(n+1).*rsource(2))));
        C_in = ((1/(8)).*sqrt(epsilon(slayer)).*(hnk_s(1:2*nmax+1).*
            exp(-1i.*(n-1).*rsource(2)) - hnk_s(3:2*nmax+3).*
            exp(-1i.*(n+1).*rsource(2))));
    end
    if slayer==1 %source in first layer
        knowns(1,1,:) = -(C_out).*hnk(slayer,:);
        knowns(1,2,:) = -(C_out).*e_nmax(slayer,:).* hpnk(slayer,:);
    elseif slayer==M+1 %source in last layer
        knowns(1,2*M-1,:) = (C_in).*jnk1(slayer-1,:);
        knowns(1,2*M,:) = (C_in).*e_nmax(slayer,:).* jpnk1(slayer-1,:);
    else
        knowns(1,2*slayer-3,:) = (C_in).*jnk1(slayer-1,:);
```

```
        knowns(1,2*slayer-2,:) = (C_in).*e_nmax(slayer,:).* jpnk1(slayer-1,:);
        knowns(1,2*slayer-1,:) = -(C_out).*hnk(slayer,:);
        knowns(1,2*slayer,:) = -(C_out).*e_nmax(slayer,:).* hpnk(slayer,:);
    end
else %plane wave
    knowns=zeros(1,2*M,2*nmax+1);
    for nn=-nmax:nmax
        knowns(1,2*M-1,nn+nmax+1) = 1i^nn.*jnk1(M,nn+nmax+1);
        knowns(1,2*M,nn+nmax+1) = 1i^nn.*e_nmax(M+1,nn+nmax+1).*
            jpnk1(M,nn+nmax+1);
    end
end

%solve the system for the unknown coefficients
for nn=1:2*nmax+1
    unknowns(1,:,nn)=matrix(:,:,nn)\transpose(knowns(1,:,nn));
end

Aln=zeros(M+1,2*nmax+1);
Bln=zeros(M+1,2*nmax+1);

Aln(1,:)=unknowns(1,1,:);
Bln(1,:)=zeros(size(unknowns(1,1,:)));
Aln(M+1,:)=zeros(size(unknowns(1,2*M,:)));
Bln(M+1,:)=unknowns(1,2*M,:);

for mm=2:M
    Aln(mm,:)=unknowns(1,2*mm-2,:);
    Bln(mm,:)=unknowns(1,2*mm-1,:);
end

result=[Aln;Bln];
```

A.2 Cly2D_ML_PW.m

```
function [result Q]=Cyl2D_ML_PW(Lambda,Radius,epsilon,isEz)
```

```
%code will find the fields from a multilayered cylinder in 2D with a plane
%wave excitation at wavelength Lambda
%Radius is vector giving the radius of each layer of the cylinder
%Epsilon gives the electric permittivity of each layer, the last entry is
%the permittivity of the surrounding medium
%isEz gives the polarization of the calculation, isEz=1, means E in z
    direciton
%result is Ez if isEz=1
%result is [Ex Ey] if isEz=2
%Q is the scattering and extinction efficiencies, [Qscat Qext]

% Bessel and Hankel functions will be precalculated for speed
clear global hnk jnk hpnk jpnk hnk1 jnk1 hpnk1 jpnk1
global hnk jnk hpnk jpnk hnk1 jnk1 hpnk1 jpnk1

%Function materials can be used to look up material data from experimental
%data
%epsilon=materials(Lambda,epsilon);
nParticle=sqrt(epsilon);

M=length(Radius); %number of layers
k=2*pi/Lambda.*nParticle;

c=3e8;                    %speed light in m/s
omega=2*pi*c/(Lambda*1e-9);     %angular frequency
e0=8.85e-12;
imp_freespace=376.73;
E0=e0*1e-9*omega*imp_freespace; %constant required to normalize Er,Ephi when
    doing Hz polarization

%number of modes to be plotted
nmax=real(ceil(max(k)*max(Radius)+4*(max(k)*max(Radius))^(1/3)+2));

sz=3; %extents of field plot region, scaled by cylinder radius
npts=250; %Field plots will be npts x npts

%determines x values for field plotting
```

```
numx=npts;
xstart=-sz*max(Radius);
xstop=sz*max(Radius);
x=xstart:(xstop-xstart)/(numx-1):xstop;

%determines y values for field plotting
numy=npts;
ystart=-sz*max(Radius);
ystop=sz*max(Radius);
y=ystart:(ystop-ystart)/(numy-1):ystop;

[X Y Z]=meshgrid(x,y,0); %creates 2-D grid of values where each point
[phi r z]=cart2pol(X,Y,Z); %converts values to cylindrical coordinates

%matrix telling whether source is in each layer, for PW source it is in the
%outermost layer
%k_in will be the k vector of each point for field plotting
r_in=zeros(M,size(r,1),size(r,2));
k_in=zeros(size(r));
eps_in=zeros(size(r));
for kk=1:M
    r_in(kk,:,:)=r<Radius(kk);
end
r_in(M+1,:,:)=ones(size(r,1),size(r,2))-squeeze(r_in(M,:,:));
r_in(2:M,:,:)=r_in(2:M,:,:)-r_in(1:M-1,:,:);
for kk=1:M+1
    k_in=k_in+squeeze(r_in(kk,:,:)).*k(kk);
    eps_in=eps_in+squeeze(r_in(kk,:,:)).*epsilon(kk);
end

%creates matricies that are stacks of original matrix with height nmax
for nn=1:2*nmax+1
    phi_nmax(nn,:,:)=phi;
    r_nmax(nn,:,:)=r;
    n_nmax(nn,:,:)=(nn-nmax-1).*ones(size(r,1),size(r,2));
    eps_in_nmax(nn,:,:)=eps_in;
end
```

```
%calculates necessary Bessel/Hankel function, two sets are needed that
%use different k-vectors
for nn=-nmax-1:nmax+1
    hnk(:,nn+1+nmax+1)=besselh(nn,k(1:(length(k)-1)).*Radius);
    jnk(:,nn+1+nmax+1)=besselj(nn,k(1:(length(k)-1)).*Radius);
    hnk1(:,nn+1+nmax+1)=besselh(nn,k(2:(length(k))).*Radius);
    jnk1(:,nn+1+nmax+1)=besselj(nn,k(2:(length(k))).*Radius);
end
%calculates derivatives of Bessel/Hankel functions based on recursive
%properties of bessel functions
for nn=-nmax:nmax
    hpnk(:,nn+1+nmax)=transpose((k(1:(length(k)-1))./2)).*
        (hnk(:,nn+1+nmax)-hnk(:,nn+1+nmax+2));
    jpnk(:,nn+1+nmax)=transpose((k(1:(length(k)-1))./2)).*
        (jnk(:,nn+1+nmax)-jnk(:,nn+1+nmax+2));
    hpnk1(:,nn+1+nmax)=transpose((k(2:(length(k)))./2)).*
        (hnk1(:,nn+1+nmax)-hnk1(:,nn+1+nmax+2));
    jpnk1(:,nn+1+nmax)=transpose((k(2:(length(k)))./2)).*
        (jnk1(:,nn+1+nmax)-jnk1(:,nn+1+nmax+2));
end
%removes extra elements from Bessel/Hankel functions that were used for
%recursive calculation of derivatives
hnk=hnk(:,2:size(hnk,2)-1);
jnk=jnk(:,2:size(jnk,2)-1);
hnk1=hnk1(:,2:size(hnk1,2)-1);
jnk1=jnk1(:,2:size(jnk1,2)-1);

%sets SourceDir based on isEz, which determines polarization of calculation
if isEz
    SourceDir=3;
else
    SourceDir=1;
end

%Calculates scattering coefficients
ab=Cly2D_ML_coeff(epsilon,Radius,nmax,Lambda,NaN,1,SourceDir);
```

```
Asn=zeros(size(r_nmax));
Bsn=zeros(size(r_nmax));
%makes larger matricies of A/B coefficients to speed multiplication later
for nn=-nmax:nmax
    for mm=1:M+1
        Asn(nn+nmax+1,:,:)=squeeze(Asn(nn+nmax+1,:,:))+
            ab(mm,nn+nmax+1).*ones(size(r)).*squeeze(r_in(mm,:,:));
        Bsn(nn+nmax+1,:,:)=squeeze(Bsn(nn+nmax+1,:,:))+
            ab(mm+M+1,nn+nmax+1).*ones(size(r)).*squeeze(r_in(mm,:,:));
    end
end
Asn=squeeze(Asn);
Bsn=squeeze(Bsn);

%precalculated Bessel/Hankel functions and derivatives for plotting fields
hnk2=zeros([2*nmax+1 size(r)]);
jnk2=zeros([2*nmax+1 size(r)]);
hpnk2=zeros([2*nmax+1 size(r)]);
jpnk2=zeros([2*nmax+1 size(r)]);
for nn=-nmax-1:nmax+1
    hnk2(nn+2+nmax,:,:)=besselh(nn,k_in.*r); %H_n(k_l*r) a set is calculated
        for each layer
    jnk2(nn+2+nmax,:,:)=besselj(nn,k_in.*r);
end
hpnk2=(permute(repmat(k_in/2,[1 1 2*nmax+1]),[3 1 2])).*
    (hnk2(1:size(hnk2,1)-2,:,:)-hnk2(3:size(hnk2,1),:,:)); %H'_n(k_l*r) a set
    is calculated for each layer
jpnk2=(permute(repmat(k_in/2,[1 1 2*nmax+1]),[3 1 2])).*
    (jnk2(1:size(jnk2,1)-2,:,:)-jnk2(3:size(jnk2,1),:,:));

hnk2=hnk2(2:size(hnk2,1)-1,:,:);
jnk2=jnk2(2:size(jnk2,1)-1,:,:);
hnk2=squeeze(hnk2);
jnk2=squeeze(jnk2);

if isEz==1
    %Calculates Ez field
```

```
    Ez_temp=(Asn.*jnk2+Bsn.*hnk2).*exp(-1i.*n_nmax.*phi_nmax);
    Ez_source=exp(1i.*k(length(k)).*X);
    Ez=squeeze(sum(Ez_temp,1));

    Ez=squeeze(Ez)+Ez_source.*squeeze(r_in(M+1,:,:));
    result(:,:,1)=Ez;
    result(:,:,3)=X;
    result(:,:,4)=Y;
elseif isEz==0
    %Calculates Ex and Ey fields
    E_r_temp=(n_nmax./(eps_in_nmax.*E0.*r_nmax)).*
        (Asn.*jnk2+Bsn.*hnk2).*exp(-1i.*n_nmax.*phi_nmax);
    E_phi_temp=(1./(1i*eps_in_nmax*E0)).*
        (Asn.*jpnk2+Bsn.*hpnk2).*exp(-1i.*n_nmax.*phi_nmax);

    E_r=squeeze(sum(E_r_temp,1)); %sums field over different modes n
    E_phi=squeeze(sum(E_phi_temp,1)); %sums field over different modes n

    Ex=cos(phi).*E_r-sin(phi).*E_phi;
    Ey=sin(phi).*E_r+cos(phi).*E_phi;

    Ey_source=exp(1i.*k(M+1).*X);

    Ey=Ey+Ey_source.*squeeze(r_in(M+1,:,:));
    result(:,:,1)=Ex;
    result(:,:,2)=Ey;
    result(:,:,3)=X;
    result(:,:,4)=Y;
end

%Calculates Qscat and Qext
%bn is the coefficients for the outgoing field of outermost layer
bn=squeeze(Bsn(:,1,1));
for nn=-nmax:nmax
    bn(nn+nmax+1)=-bn(nn+nmax+1)./1i^nn;
end
Qext=bn(nmax+1);
```

```
for nn=1:nmax
    Qext=Qext+2*bn(nn+nmax+1);
end
Qext=real(Qext);
Qscat=abs(bn(nmax+1)).^2;
for nn=1:nmax
    Qscat=Qscat+2*abs(bn(nn+nmax+1))^2;
end
Qscat=Qscat.*2/(2.*pi./Lambda.*max(Radius));
Qext=Qext.*2./(2.*pi./Lambda.*max(Radius));
Q=[Qscat;Qext];
```

A.3 Cly2D_ML_PS.m

```
function [result Gamma]=Cyl2D_ML_PS(Lambda,Radius,epsilon,source,SourceDir)
%code will find the fields from a multilayered cylinder in 2D with a Point
%Source excitation at wavelength Lambda (nm)
%Radius is vector giving the radius of each layer of the cylinder
%Epsilon gives the electric permittivity of each layer, the last entry is
%the permittivity of the surrounding medium
%source gives the location of the source in [x y] (nm)
%SourceDir gives the orientation of the dipole moment 1->x, 2->y, 3->z
%Gamma = [G Gr Gnr], G is the normalized PDOS, Gr is the normalized power
%radiated to the far field, Gnr = G-Gr.

% Bessel and Hankel functions will be precalculated for speed
clear global hnk jnk hpnk jpnk hnk1 jnk1 hpnk1 jpnk1 jnk_s hnk_s
global hnk jnk hpnk jpnk hnk1 jnk1 hpnk1 jpnk1 jnk_s hnk_s

%source location in polar
[rsource(2) rsource(1)]=cart2pol(source(1),source(2));
rs=rsource(1);

if SourceDir==3
    isEz=1;
else
```

```
    isEz=0;
end

nParticle=sqrt(epsilon);

M=length(Radius);
k=2*pi/Lambda.*nParticle;

c=3e8;                    %speed light in m/s
omega=2*pi*c/(Lambda*1e-9);     %angular frequency
e0=8.85e-12;
imp_freespace=376.73;
E0=e0*1e-9*omega*imp_freespace; %constant required to normalize Er,Ephi when
    doing Hz polarization

%number of modes to be plotted
nmax=real(ceil(max(k)*max(Radius)+4*(max(k)*max(Radius))^(1/3)+2));

sz=3; %extents of field plot region, scaled by cylinder radius
npts=250; %Field plots will be npts x npts

%determines x values for field plotting
numx=npts;
xstart=-sz*max(Radius);
xstop=sz*max(Radius);
x=xstart:(xstop-xstart)/(numx-1):xstop;

%determines y values for field plotting
numy=npts;
ystart=-sz*max(Radius);
ystop=sz*max(Radius);
y=ystart:(ystop-ystart)/(numy-1):ystop;

[X Y Z]=meshgrid(x,y,0); %creates 2-D grid of values where each point
[phi r z]=cart2pol(X,Y,Z); %converts values to cylindrical coordinates

%matrix telling whether source is in each layer
```

```
%k_in will be the k vector of each point for field plotting
r_in=zeros(M,size(r,1),size(r,2));
k_in=zeros(size(r));
eps_in=zeros(size(r));
for kk=1:M
    r_in(kk,:,:)=r<Radius(kk);
end
r_in(M+1,:,:)=ones(size(r,1),size(r,2))-squeeze(r_in(M,:,:));
r_in(2:M,:,:)=r_in(2:M,:,:)-r_in(1:M-1,:,:);
for kk=1:M+1
    k_in=k_in+squeeze(r_in(kk,:,:)).*k(kk);
    eps_in=eps_in+squeeze(r_in(kk,:,:)).*epsilon(kk);
end

%creates matricies that are stacks of original matrix with height nmax
for nn=1:2*nmax+1
    phi_nmax(nn,:,:)=phi;
    r_nmax(nn,:,:)=r;
    n_nmax(nn,:,:)=(nn-nmax-1).*ones(size(r,1),size(r,2));
    eps_in_nmax(nn,:,:)=eps_in;
end

%find layer which contains the source
rtemp=[Radius rs];
rtemp=sort(rtemp);
slayer=find(rtemp==rs);

%calculates necessary Bessel/Hankel function, two sets are needed that
%use different k-vectors
for nn=-nmax-1:nmax+1
    hnk(:,nn+1+nmax+1)=besselh(nn,k(1:(length(k)-1)).*Radius);
    jnk(:,nn+1+nmax+1)=besselj(nn,k(1:(length(k)-1)).*Radius);
    hnk1(:,nn+1+nmax+1)=besselh(nn,k(2:(length(k))).*Radius);
    jnk1(:,nn+1+nmax+1)=besselj(nn,k(2:(length(k))).*Radius);
    jnk_s(nn+1+nmax+1) = besselj(nn,k(slayer).*rs);
    hnk_s(nn+1+nmax+1) = besselh(nn,k(slayer).*rs);
end
```

```
%calculates derivatives of Bessel/Hankel functions based on recursive
%properties of bessel functions
for nn=-nmax:nmax
    hpnk(:,nn+1+nmax)=transpose((k(1:(length(k)-1))./2)).*
        (hnk(:,nn+1+nmax)-hnk(:,nn+1+nmax+2));
    jpnk(:,nn+1+nmax)=transpose((k(1:(length(k)-1))./2)).*
        (jnk(:,nn+1+nmax)-jnk(:,nn+1+nmax+2));
    hpnk1(:,nn+1+nmax)=transpose((k(2:(length(k)))./2)).*
        (hnk1(:,nn+1+nmax)-hnk1(:,nn+1+nmax+2));
    jpnk1(:,nn+1+nmax)=transpose((k(2:(length(k)))./2)).*
        (jnk1(:,nn+1+nmax)-jnk1(:,nn+1+nmax+2));
    hpnk_s(nn+1+nmax)=transpose((k(slayer)./2)).*
        (hnk_s(nn+1+nmax)-hnk_s(nn+1+nmax+2));
    jpnk_s(nn+1+nmax)=transpose((k(slayer)./2)).*
        (jnk_s(nn+1+nmax)-jnk_s(nn+1+nmax+2));
end
if SourceDir==3
    hnk_s=hnk_s(2:size(hnk_s,2)-1);
    jnk_s=jnk_s(2:size(jnk_s,2)-1);
end
%removes extra elements from Bessel/Hankel functions that were used for
%recursive calculation of derivatives
hnk=hnk(:,2:size(hnk,2)-1);
jnk=jnk(:,2:size(jnk,2)-1);
hnk1=hnk1(:,2:size(hnk1,2)-1);
jnk1=jnk1(:,2:size(jnk1,2)-1);

%Calculates scattering coefficients
ab=Cly2D_ML_coeff_v12(epsilon,Radius,nmax,Lambda,source,0,SourceDir);
Asn=zeros(size(r_nmax));
Bsn=zeros(size(r_nmax));
%makes larger matricies of A/B coefficients to speed multiplication later
for nn=-nmax:nmax
    for mm=1:M+1
        Asn(nn+nmax+1,:,:)=squeeze(Asn(nn+nmax+1,:,:))+
            ab(mm,nn+nmax+1).*ones(size(r)).*squeeze(r_in(mm,:,:));
```

```
        Bsn(nn+nmax+1,:,:)=squeeze(Bsn(nn+nmax+1,:,:))+
            ab(mm+M+1,nn+nmax+1).*ones(size(r)).*squeeze(r_in(mm,:,:));
    end
end
Asn=squeeze(Asn);
Bsn=squeeze(Bsn);

%precalculated Bessel/Hankel functions and derivatives for plotting fields
hnk2=zeros([2*nmax+1 size(r)]);
jnk2=zeros([2*nmax+1 size(r)]);
hpnk2=zeros([2*nmax+1 size(r)]);
jpnk2=zeros([2*nmax+1 size(r)]);
for nn=-nmax-1:nmax+1
    hnk2(nn+2+nmax,:,:)=besselh(nn,k_in.*r); %H_n(k_l*r) a set is calculated
        for each layer
    jnk2(nn+2+nmax,:,:)=besselj(nn,k_in.*r);
end
hpnk2=(permute(repmat(k_in/2,[1 1 2*nmax+1]),[3 1 2])).*
    (hnk2(1:size(hnk2,1)-2,:,:)-hnk2(3:size(hnk2,1),:,:));
jpnk2=(permute(repmat(k_in/2,[1 1 2*nmax+1]),[3 1 2])).*
    (jnk2(1:size(jnk2,1)-2,:,:)-jnk2(3:size(jnk2,1),:,:));

hnk2=hnk2(2:size(hnk2,1)-1,:,:);
jnk2=jnk2(2:size(jnk2,1)-1,:,:);
hnk2=squeeze(hnk2);
jnk2=squeeze(jnk2);

%distance for each plot point from source
Xs = X - ones(size(X))*source(1);
Ys = Y - ones(size(Y))*source(2);
[PHIs Rs] = cart2pol(Xs,Ys);

%calculates electric field
if SourceDir==3
    %contribution of scattered fields
    E_z_temp=(Asn.*jnk2+Bsn.*hnk2).*exp(1i.*n_nmax.*phi_nmax);
```

```
    Ez_source=besselh(0,k(slayer).*Rs)/(4*1i);

    E_z=squeeze(sum(E_z_temp,1)); %sums field over different modes n

    E_z=squeeze(E_z)+Ez_source.*squeeze(r_in(slayer,:,:));
    result(:,:,1)=E_z;
    result(:,:,3)=X;
    result(:,:,4)=Y;

elseif SourceDir==1
    %contribution of scattered fields
    %Er Ephi found in Hz pol derivation of e field
    E_r_temp=-(n_nmax./(eps_in_nmax.*E0.*r_nmax)).*
        (Asn.*jnk2+Bsn.*hnk2).*exp(1i.*n_nmax.*phi_nmax);
    E_phi_temp=(1./(1i*eps_in_nmax*E0)).*
        (Asn.*jpnk2+Bsn.*hpnk2).*exp(1i.*n_nmax.*phi_nmax);

    Er_source=-1./(1i*E0*Rs).*(cos(PHIs)).* (-besselh(1,k(slayer)*Rs)/4);
    Ephi_source=-k(slayer)/(2*1i*E0).*(sin(PHIs)/4).*
        (besselh(0,k(slayer)*Rs)-besselh(2,k(slayer)*Rs));

    E_r=squeeze(sum(E_r_temp,1)); %sums field over different modes n
    E_phi=squeeze(sum(E_phi_temp,1));

    E_r=squeeze(E_r);
    E_phi=squeeze(E_phi);
    Ex=cos(phi).*E_r-sin(phi).*E_phi;
    Ey=sin(phi).*E_r+cos(phi).*E_phi;

    %Source Contribution
    E_r_s=Er_source.*squeeze(r_in(slayer,:,:));
    E_phi_s=Ephi_source.*squeeze(r_in(slayer,:,:));
    Ex_s=cos(PHIs).*E_r_s-sin(PHIs).*E_phi_s;
    Ey_s=sin(PHIs).*E_r_s+cos(PHIs).*E_phi_s;

    result(:,:,1)=Ex+Ex_s;
    result(:,:,2)=Ey+Ey_s;
```

```
    result(:,:,3)=X;
    result(:,:,4)=Y;

elseif SourceDir==2
    %contribution of scattered fields
    %Er Ephi found in Hz pol derivation of e field
    E_r_temp=-(n_nmax./(eps_in_nmax.*E0.*r_nmax)).*
        (Asn.*jnk2+Bsn.*hnk2).*exp(1i.*n_nmax.*phi_nmax);
    E_phi_temp=(1./(1i*eps_in_nmax*E0)).*
        (Asn.*jpnk2+Bsn.*hpnk2).*exp(1i.*n_nmax.*phi_nmax);

    Er_source=1./(1i*E0*Rs).*(-sin(PHIs)).* (-besselh(1,k(slayer)*Rs)/4);
    Ephi_source=k(slayer)/(2*1i*E0).*(cos(PHIs)/4).*
        (besselh(0,k(slayer)*Rs)-besselh(2,k(slayer)*Rs));

    E_r=squeeze(sum(E_r_temp,1)); %sums field over different modes n
    E_phi=squeeze(sum(E_phi_temp,1));

    E_r=squeeze(E_r);
    E_phi=squeeze(E_phi);
    Ex=cos(phi).*E_r-sin(phi).*E_phi;
    Ey=sin(phi).*E_r+cos(phi).*E_phi;

    %Source Contribution
    E_r_s=Er_source.*squeeze(r_in(slayer,:,:));
    E_phi_s=Ephi_source.*squeeze(r_in(slayer,:,:));
    Ex_s=cos(PHIs).*E_r_s-sin(PHIs).*E_phi_s;
    Ey_s=sin(PHIs).*E_r_s+cos(PHIs).*E_phi_s;

    result(:,:,1)=Ex+Ex_s;
    result(:,:,2)=Ey+Ey_s;
    result(:,:,3)=X;
    result(:,:,4)=Y;

end
```

```
%calculates radiated power Gr by integrating the opynting vector flux through
%a surface outside the structure. Same thing is done in BH, this can be
%calculated from the outgoing field coefficients
bn=squeeze(Bsn(:,1,1));
n=(-nmax:nmax);
if slayer==M+1 %if source is outside particle
    if SourceDir==1
        C_out=((-1/(8*1i)).*sqrt(epsilon(slayer)).*
            (jnk_s(1:2*nmax+1).*exp(-1i.*(n-1).*rsource(2))+
            jnk_s(3:2*nmax+3).*exp(-1i.*(n+1).*rsource(2))));
    elseif SourceDir==2
        C_out=((1/(8)).*sqrt(epsilon(slayer)).*
            (jnk_s(1:2*nmax+1).*exp(-1i.*(n-1).*rsource(2))-
            jnk_s(3:2*nmax+3).*exp(-1i.*(n+1).*rsource(2))));
    elseif SourceDir==3
        C_out=(jnk_s.*(1/(4*1i))).*exp(-1i.*n.*rsource(2));
    end
else
    C_out=zeros(size(bn));
end

%Calculates the radiated Power, Gr
Gr=0;
for nn=-nmax:nmax
    Gr=Gr+(bn(nn+nmax+1)+C_out(nn+nmax+1)).*
        conj(bn(nn+nmax+1)+C_out(nn+nmax+1));
end

if not(SourceDir==3)
    hnk_s=hnk_s(2:size(hnk_s,2)-1);
    jnk_s=jnk_s(2:size(jnk_s,2)-1);
end

%calculate Gamma (G) from the LDOS
if SourceDir==3
    %A,B coefficients for source location
    An_s=ab(slayer,:);
```

```
    Bn_s=ab(slayer+M+1,:);

    %Calculates electric field
    E_z_temp=(An_s.*jnk_s+Bn_s.*hnk_s) .*exp(1i.*n.*rsource(2));
    E_z=squeeze(sum(E_z_temp)); %sums field over different modes n

    %take imaginary part of greens funciton and add source contribution
    LDOS=imag(E_z+1/(4*1i));

elseif SourceDir==1
    %A,B coefficients for source location
    An_s=ab(slayer,:);
    Bn_s=ab(slayer+M+1,:);

    E_r_temp=-(n./(epsilon(slayer).*E0.*rsource(1))).*
        (An_s.*jnk_s+Bn_s.*hnk_s).*exp(1i.*n.*rsource(2));
    E_phi_temp=(1./(1i*epsilon(slayer)*E0)).*
        (An_s.*jpnk_s+Bn_s.*hpnk_s).*exp(1i.*n.*rsource(2));

    E_r=squeeze(sum(E_r_temp));
    E_phi=squeeze(sum(E_phi_temp));

    E_x=cos(rsource(2)).*E_r-sin(rsource(2)).*E_phi;
    E_y=sin(rsource(2)).*E_r+cos(rsource(2)).*E_phi;

    LDOS=imag(E_x+1/(8*1i));

elseif SourceDir==2
    %A,B coefficients for source location
    An_s=ab(slayer,:);
    Bn_s=ab(slayer+M+1,:);

    E_r_temp=-(n./(epsilon(slayer).*E0.*rsource(1))).*
        (An_s.*jnk_s+Bn_s.*hnk_s).*exp(1i.*n.*rsource(2));
    E_phi_temp=(1./(1i*epsilon(slayer)*E0)).*
        (An_s.*jpnk_s+Bn_s.*hpnk_s).*exp(1i.*n.*rsource(2));
```

```
    E_r=squeeze(sum(E_r_temp));
    E_phi=squeeze(sum(E_phi_temp));

    E_x=cos(rsource(2)).*E_r-sin(rsource(2)).*E_phi;
    E_y=sin(rsource(2)).*E_r+cos(rsource(2)).*E_phi;

    LDOS=imag(E_y+1/(8*1i));
end
G=LDOS;
Gnr = G - Gr;
Gamma=[G Gr Gnr];
```

References

Adam, J. A. (2009). *A mathematical nature walk*. Pricnceton University Press.

Akahane, Y., Asano, T., and Song, B.-S. (2003). High-Q photonic nanocavity in a two-dimensional photonic crystal. *Nature*, 425(6961):944–7.

Allen, L., Barnett, S., and Padgett, M. J. (2003). *Optical Angular Momentum*. Bristol.

Allen, L., Beijersbergen, M., Spreeuw, R., and Woerdman, J. (1992). Orbital angular momentum of light and the transformation of Laguerre-Gaussian laser modes. *Physical Review*, 45(11):8185–8189.

Altug, H., Englund, D., and Vučković, J. (2006). Ultrafast photonic crystal nanocavity laser. *Nature Physics*, 2(7):484–488.

Armani, D. K., Kippenberg, T. J., Spillane, S. M., and Vahala, K. J. (2003). Ultra-high-Q toroid microcavity on a chip. *Nature*, 421(6926):925–928.

Asatryan, A. A., Busch, K., Mcphedran, R. C., and Botten, L. C. (2007). Two-dimensional Green tensor and local density of states in finite-sized two-dimensional photonic crystals. *Waves Random Media*, 13(2003):9–25.

Bao, J., Yu, N., Capasso, F., Mates, T., Troccoli, M., and Belyanin, A. (2007). Controlled modification of erbium lifetime in silicon dioxide with metallic overlayers. *Applied Physics Letters*, 91(13):131103.

Barsi, C., Wan, W., and Fleischer, J. W. (2009). Imaging through nonlinear media using digital holography. *Nature Photonics*, 3(4):211–215.

Barton, J. S., Skogen, E. J., Mašanović, M. L., Denbaars, S. P., and Coldren, L. A. (2003). A widely-tunable high-speed transmitter using an integrated SGDBR laser-Semiconductor Optical Amplifier and Mach- Zehnder modulator. *IEEE Journal of Selected Topics in Quantum Electronics*, 9(5):1113–1117.

Bashevoy, M., Fedotov, V., and Zheludev, N. (2005). Optical whirlpool on an absorbing metallic nanoparticle. *Optics Express*, 13(21):8372–9.

Becker, P. C., Olsson, N. A., and Simpson, J. R. (1999). *Erbium-Doped Fiber Amplifiers*. Academic Press.

Benisty, H., Danglot, J., Talneau, A., Enoch, S., Pottage, J. M., and David, A. (2008). Investigation of Extracting Photonic Crystal Lattices for Guided Modes of GaAs-Based Heterostructures. *IEEE Journal of Quantum Electronics*, 44(8):777–789.

Berenger, J. (1994). A perfectly matched layer for the absorption of electromagnetic waves. *Journal of Computational Physics*, 114(2):185–200.

Berkhout, G., Lavery, M., Courtial, J., Beijersbergen, M., and Padgett, M. (2010). Efficient Sorting of Orbital Angular Momentum States of Light. *Physical Review Letters*, 105(15):8–11.

Biteen, J. S., Pacifici, D., Lewis, N. S., and Atwater, H. A. (2005). Enhanced radiative emission rate and quantum efficiency in coupled silicon nanocrystal-nanostructured gold emitters. *Nano Letters*, 5(9):1768–73.

Bohren, C. F. and Huffman, D. R. (1998). *Absorption and scatteirng of light by small particles*. Wiley-VCH.

Boriskin, A. and Nosich, A. (2002). Whispering-gallery and Luneburg-lens effects in a beam-fed circularly layered dielectric cylinder. *IEEE Transactions on Antennas and Propagation*, 50(9):1245–1249.

Bozinovic, N., Yue, Y., Ren, Y., Tur, M., Kristensen, P., Huang, H., Willner, A. E., and Ramachandran, S. (2013). Terabit-Scale Orbital Angular Momentum Mode Division Multiplexing in Fibers. *Science*, 340(6140):1545–1548.

Brongersma, M. L. and Kik, P. G. (2007). *Surface Plasmon Nanophotoincs*. Springer.

Catrysse, P. B. and Fan, S. (2009). Understanding the dispersion of coaxial plasmonic structures through a connection with the planar metal-insulator-metal geometry. *Applied Physics Letters*, 94(23):231111.

Chavez-Cerda, S., Padgett, M., Allison, I., New, G., Gutierrez-Vega, J., O'Neil, A., MacVicar, I., and Courtial, J. (2002). Holographic generation and orbital angular momentum of high-order Mathieu beams. *Journal of Optics B: Quantum and Semiclassical Optics*, 4(2):S52.

Choi, S.-J., Djordjev, K., and Dapkus, P. (2003). Microdisk lasers vertically coupled to output waveguides. *IEEE Photonics Technology Letters*, 15(10):1330–1332.

Chuang, S. L. (2009). *Physics of Photonic Devices*. Wiley, Hoboken, NJ.

Coldren, L. A. and Corzine, S. W. (1995). *Diode Lasers and Photonic Integrated Circuits*. John Wiley & Sons, Inc., New York.

Colombo, C., Heiβ, M., Gratzel, M., and Fontcuberta i Morral, A. (2009). Gallium arsenide p-i-n radial structures for photovoltaic applications. *Applied Physics Letters*, 94(17):173108.

Creatore, C., Andreani, L. C., Miritello, M., Lo Savio, R., and Priolo, F. (2009). Modification of erbium radiative lifetime in planar silicon slot waveguides. *Applied Physics Letters*, 94(10):103112.

Dal Negro, L. and Boriskina, S. (2012). Deterministic aperiodic nanostructures for photonics and plasmonics applications. *Laser & Photonics Reviews*, 6(2):178–218.

Dal Negro, L., Lawrence, N., and Trevino, J. (2012). Analytical light scattering and orbital angular momentum spectra of arbitrary Vogel spirals. *Optics Express*, 20(16):18209–18223.

Dal Negro, L., Li, R., Warga, J., and Basu, S. N. (2008). Sensitized erbium emission from silicon-rich nitride/silicon superlattice structures. *Applied Physics Letters*, 92(18):181105.

David, A., Benisty, H., and Weisbuch, C. (2007). Optimization of Light-Diffracting Photonic-Crystals for High Extraction Efficiency LEDs. *Journal of Display Technology*, 3(2):133–148.

David, A., Fujii, T., Matioli, E., Sharma, R., Nakamura, S., DenBaars, S. P., Weisbuch, C., and Benisty, H. (2006). GaN light-emitting diodes with Archimedean lattice photonic crystals. *Applied Physics Letters*, 88(7):073510.

David, A., Meier, C., Sharma, R., Diana, F. S., DenBaars, S. P., Hu, E., Nakamura, S., Weisbuch, C., and Benisty, H. (2005). Photonic bands in two-dimensionally patterned multimode GaN waveguides for light extraction. *Applied Physics Letters*, 87(10):101107.

David, S., Chelnokov, A., Lourtioz, J., and Member, S. (2001). Isotropic Photonic Structures : Archimedean-Like. *IEEE Journal of Quantum Electronics*, 37(11):1427–1434.

Desurvine, E. (1994). *Erbium-doped fiber amplifiers: principles and applications.* Wiley, New York, 19 edition.

Djordjev, K., Choi, S.-J., and Dapkus, P. (2002a). Vertically coupled InP microdisk switching devices with electroabsorptive active regions. *IEEE Photonics Technology Letters*, 14(8):1115–1117.

Djordjev, K., Choi, S.-J., and Dapkus, R. (2002b). Microdisk tunable resonant filters and switches. *IEEE Photonics Technology Letters*, 14(6):828–830.

Duan, X., Huang, Y., Agarwal, R., and Lieber, C. (2003). Single-nanowire electrically driven lasers. *Nature*, 421(6920):241–245.

Einstein, A. (1916). Strahlungs-emission und absorption nach der quantentheorie. *Deutsche Physikalische Gesellschaft*, 18:318–323.

Fan, S., Villeneuve, P., Joannopoulos, J., and Schubert, E. (1997). High Extraction Efficiency of Spontaneous Emission from Slabs of Photonic Crystals. *Physical Review Letters*, 78(17):3294–3297.

Fang, A. W., Park, H., Cohen, O., Jones, R., Paniccia, M. J., and Bowers, J. E. (2006). Electrically pumped hybrid AlGaInAs-silicon evanescent laser. *Optics Express*, 14(20):9203–10.

Fujii, T., Gao, Y., Sharma, R., Hu, E. L., DenBaars, S. P., and Nakamura, S. (2004). Increase in the extraction efficiency of GaN-based light-emitting diodes via surface roughening. *Applied Physics Letters*, 84(6):855.

Gerard, J. M., Barrier, D., Marzin, J. Y., Kuszelewicz, R., Manin, L., Costard, E., Thierry-Mieg, V., and Rivera, T. (1996). Quantum boxes as active probes for photonic microstructures: The pillar microcavity case. *Applied Physics Letters*, 69(4):449.

Gibson, G., Courtial, J., Padgett, M., Vasnetsov, M., Pas'ko, V., Barnett, S., and Franke-Arnold, S. (2004). Free-space information transfer using light beams carrying orbital angular momentum. *Optics Express*, 12(22):5448–56.

Gong, Y., Makarova, M., Yerci, S., Li, R., Stevens, M. J., Baek, B., Nam, S. W., Dal Negro, L., and Vuckovic, J. (2010a). Observation of transparency of Erbium-doped silicon nitride in photonic crystal nanobeam cavities. *Optics Express*, 18(13):13863–73.

Gong, Y., Makarova, M., Yerci, S., Li, R., Stevens, M. J., Baek, B., Nam, S. W., Hadfield, R. H., Dorenbos, S. N., Zwiller, V., Vučković, J., and Dal Negro, L. (2010b). Linewidth narrowing and Purcell enhancement in photonic crystal cavities on an Er-doped silicon nitride platform. *Optics Express*, 18(3):2680–2682.

Gopinath, A., Boriskina, S. V., Yerci, S., Li, R., and Dal Negro, L. (2010). Enhancement of the 1.54 μm Er3+ emission from quasiperiodic plasmonic arrays. *Applied Physics Letters*, 96(7):071113.

Grier, D. G. (2003). A revolution in optical manipulation. *Nature*, 424(6950):810–6.

Guichard, A. R., Barsic, D. N., Sharma, S., Kamins, T. I., and Brongersma, M. L. (2006). Tunable Light Emission from Quantum-Confined Excitons in TiSi2 -Catalyzed Silicon Nanowires. *Nano Letters*, 6(9):2140–2144.

Hao, F., Nordlander, P., Burnett, M., and Maier, S. (2007). Enhanced tunability and linewidth sharpening of plasmon resonances in hybridized metallic ring/disk nanocavities. *Physical Review B*, 76(24):245417.

Hao, F., Nordlander, P., Sonnefraud, Y., Van Dorpe, P., and Maier, S. A. (2009). Tunability of subradiant dipolar and fano-type plasmon resonances in metallic ring/disk cavities: implications for nanoscale optical sensing. *ACS Nano*, 3(3):643–52.

Hardy, G. H. and Wright, E. M. (2008). *An Introduction to the Theory of Numbers*. Oxford University Press.

Havil, J. (2012). *The Irrationals: A Story fo the Numbers You Can't count On*. Princeton University Press.

Heckenberg, N. R., McDuff, R., Smith, C. P., and White, A. G. (1992). Generation of optical phase singularities by computer-generated holograms. *Optics Letters*, 17(3):221.

Hill, M. T., Marell, M., Leong, E. S. P., Smalbrugge, B., Zhu, Y., Sun, M., van Veldhoven, P. J., Geluk, E. J., Karouta, F., Oei, Y.-S., Nötzel, R., Ning, C.-Z., and Smit, M. K. (2009). Lasing in metal-insulator-metal sub-wavelength plasmonic waveguides. *Optics Express*, 17(13):11107–12.

Hill, M. T., Oei, Y.-S., Smalbrugge, B., Zhu, Y., de Vries, T., van Veldhoven, P. J., van Otten, F. W. M., Eijkemans, T. J., Turkiewicz, J. P., de Waardt, H., Geluk, E. J., Kwon, S.-H., Lee, Y.-H., Nötzel, R., and Smit, M. K. (2007). Lasing in metallic-coated nanocavities. *Nature Photonics*, 1(10):589–594.

Hu, J., Ouyang, M., Yang, P., and Lieber, C. (1999). Controlled growth and electrical properties of heterojunctions of carbon nanotubes and silicon nanowires. *Nature*, 399(6731):48–51.

Iacona, F., Pacifici, D., Irrera, a., Miritello, M., Franzo, G., Priolo, F., Sanfilippo, D., Di Stefano, G., and Fallica, P. G. (2002). Electroluminescence at 1.54 μm in Er-doped Si nanocluster-based devices. *Applied Physics Letters*, 81(17):3242.

Irrera, A., Artoni, P., Iacona, F., Pecora, E. F., Franzò, G., Galli, M., Fazio, B., Boninelli, S., and Priolo, F. (2012). Quantum confinement and electroluminescence in ultrathin silicon nanowires fabricated by a maskless etching technique. *Nanotechnology*, 23(7):075204.

Jayaraman, V., Chuang, Z.-M., and Coldren, L. (1993). Theory, design, and performance of extended tuning range semiconductor lasers with sampled gratings. *IEEE Journal of Quantum Electronics*, 29(6):1824–1834.

Jin, J. (2011). *Theory and Computation of Electromagnetic Fields*. John Wiley & Sons, Inc., Hoboken, NJ.

Johnson, P. and Christy, R. (1972). Optical Constants of the Nobel Metals. *Physical Review B*, 6(12):4370.

Jun, Y. C., Briggs, R. M., Atwater, H. a., and Brongersma, M. L. (2009). Broadband enhancement of light emission in silicon slot waveguides. *Optics Express*, 17(9):7479–90.

Kalkman, J., Gersen, H., Kuipers, L., and Polman, A. (2006). Excitation of surface plasmons at a SiO2/Ag interface by silicon quantum dots: Experiment and theory. *Physical Review B*, 73(7):075317.

Kang, Y., Liu, H.-D., Morse, M., Paniccia, M. J., Zadka, M., Litski, S., Sarid, G., Pauchard, A., Kuo, Y.-H., Chen, H.-W., Zaoui, W. S., Bowers, J. E., Beling, A., Mcintosh, D. C., Zheng, X., and Campbell, J. C. (2008). Monolithic germanium / silicon avalanche photodiodes with 340 GHz gain bandwidth product. *Nature Photonics*, 3(1):59–63.

Khajavikhan, M., Simic, A., Katz, M., Lee, J. H., Slutsky, B., Mizrahi, A., Lomakin, V., and Fainman, Y. (2012). Thresholdless nanoscale coaxial lasers. *Nature*, 482(7384):204–207.

Kik, P. G., Brongersma, M. L., and Polman, A. (2000). Strong exciton-erbium coupling in Si nanocrystal-doped SiO\subsc{2}. *Applied Physics Letters*, 76(17):2325.

Kik, P. G. and Polman, A. (2002). Gain limiting processes in Er-doped Si nanocrystal waveguides in SiO2. *Journal of Applied Physics*, 91(1):534.

Kippenberg, T., Kalkman, J., Polman, A., and Vahala, K. (2006). Demonstration of an erbium-doped microdisk laser on a silicon chip. *Physical Review A*, 74(5):72–75.

Kittel, C. (1996). *Introduction to Solid State Physics*. John Wiley & Sons, Inc., Hoboken, NJ.

Kroekenstoel, E. J. A., Verhagen, E., Walters, R. J., Kuipers, L., and Polman, A. (2009). Enhanced spontaneous emission rate in annular plasmonic nanocavities. *Applied Physics Letters*, 95(26):263106.

Kushwaha, M. and Djafari-Rouhani, B. (2003). Green-function theory of confined plasmons in coaxial cylindrical geometries: Zero magnetic field. *Physical Review B*, 67(24):245320.

Lai, C.-F., Chao, C.-H., Kuo, H.-C., Yen, H.-H., Lee, C.-E., and Yeh, W.-Y. (2009). Directional light extraction enhancement from GaN-based film-transferred photonic crystal light-emitting diodes. *Applied Physics Letters*, 94(12):123106.

Lawrence, N. and Dal Negro, L. (2010). Light scattering, field localization and local density of states in co-axial plasmonic nanowires. *Optics Express*, 18(15):16120–32.

Lawrence, N. and Dal Negro, L. (2013). Radiation Rate Enhancement in Subwavelength Plasmonic Ring Nanocavities. *Nano Letters*, 13(8):3709–3715.

Lawrence, N., Trevino, J., and Dal Negro, L. (2012). Aperiodic arrays of active nanopillars for radiation engineering. *Journal of Applied Physics*, 111(11):113101.

Le Thomas, N., Houdré, R., Beggs, D., and Krauss, T. (2009). Fourier space imaging of light localization at a photonic band-edge located below the light cone. *Physical Review B*, 79(3):1–4.

Lee, S. Y., Forestiere, C., Pasquale, A. J., Trevino, J., Galli, P., Romagnoli, M., and Negro, L. D. (2011). Plasmon-enhanced structural coloration of metal films with isotropic Pinwheel nanoparticle arrays. *Optics Express*, 19(24):14430–14438.

Li, R. (2010). *Energy Transfer Phenomena and Radiative Process in Silicon Nitride Based Materials*. PhD thesis, Boston University.

Li, R., Schneck, J. R., Warga, J., Ziegler, L. D., and Dal Negro, L. (2008). Carrier dynamics and erbium sensitization in silicon-rich nitride nanocrystals. *Applied Physics Letters*, 93(9):091119.

Liew, S. F., Noh, H., Trevino, J., Negro, L. D., and Cao, H. (2011). Localized photonic band edge modes and orbital angular momenta of light in a golden-angle spiral. *Optics Express*, 19(24):23631–42.

Lindsey, C. P. and Patterson, G. D. (1980). Detailed comparison of the WilliamsWatts and ColeDavidson functions. *The Journal of Chemical Physics*, 73(7):3348.

Liu, A., Liao, L., Rubin, D., Nguyen, H., Ciftcioglu, B., Chetrit, Y., Izhaky, N., and Paniccia, M. (2007). High-speed optical modulation based on carrier depletion in a silicon waveguide. *Optics Express*, 15(2):660–8.

Liu, J., Sun, X., Camacho-Aguilera, R., Kimerling, L. C., and Michel, J. (2010). Ge-on-Si laser operating at room temperature. *Optics Letters*, 35(5):679–81.

Lu, Z. H., Lockwood, D. J., and Baribeau, J.-M. (1995). Quantum confinement and light emission in SiO2/Si superlattice. *Nature*, 378(16):258–60.

Lumerical. Lumerical Solutions, Inc. `http://www.lumerical.com/tcad-products/fdtd/`.

Ma, R.-M., Oulton, R. F., Sorger, V. J., Bartal, G., and Zhang, X. (2010). Room-temperature sub-diffraction-limited plasmon laser by total internal reflection. *Nature Materials*, 10(2):110–113.

Ma, R.-M., Oulton, R. F., Sorger, V. J., and Zhang, X. (2013). Plasmon lasers: coherent light source at molecular scales. *Laser & Photonics Reviews*, 7(1):1–21.

Maier, S. A. (2006). Plasmonics: Metal Nanostructures for Subwavelength Photonic Devices. *IEEE Journal of Selected Topics in Quantum Electronics*, 12(6):1214–1220.

Maier, S. A. (2007). *Plasmonics: fundamentals and Applications*. Springer.

Mair, A., Vaziri, A., Weihs, G., and Zeilinger, A. (2001). Entanglement of the orbital angular momentum states of photons. *Nature*, 412(6844):313–6.

Malacara, D. (1992). *Optical Shop Testing*. John Wiley & Sons, Inc.

Matsuda, K., Ito, Y., and Kanemitsu, Y. (2008). Photoluminescence enhancement and quenching of single CdSeZnS nanocrystals on metal surfaces dominated by plasmon resonant energy transfer. *Applied Physics Letters*, 92(21):211911.

McGroddy, K., David, a., Matioli, E., Iza, M., Nakamura, S., DenBaars, S., Speck, J. S., Weisbuch, C., and Hu, E. L. (2008). Directional emission control and increased light extraction in GaN photonic crystal light emitting diodes. *Applied Physics Letters*, 93(10):103502.

Melli, M., Polyakov, A., Gargas, D., Huynh, C., Scipioni, L., Bao, W., Ogletree, D. F., Schuck, P. J., Cabrini, S., and Weber-Bargioni, A. (2013). Reaching the Theoretical Resonance Quality Factor Limit in Coaxial Plasmonic Nanoresonators Fabricated by Helium Ion Lithography. *Nano Letters*, 13(6):2687–2691.

Mie, G. (1908). Beiträge zur Optik trüber Medien, speziell kolloidaler Metallösungen. *Annalen der Physik*, 330(3):377–445.

Miller, D. (2009). Device Requirements for Optical Interconnects to Silicon Chips. *Proceedings of the IEEE*, 97(7):1166–1185.

Mitchison, G. J. (1977). Phyllotaxis and the Fibonacci series. *Science*, 196(4287):270–275.

Munechika, K., Chen, Y., Tillack, A. F., Kulkarni, A. P., Plante, I. J.-L., Munro, A. M., and Ginger, D. S. (2010). Spectral control of plasmonic emission enhancement from quantum dots near single silver nanoprisms. *Nano Letters*, 10(7):2598–603.

Nagarajan, R., Kato, M., Lambert, D., Evans, P., Corzine, S., Lal, V., Rahn, J., Nilsson, A., Fisher, M., Kuntz, M., Pleumeekers, J., Dentai, A., Tsai, H.-S., Krause, D., Sun, H., Wu, K.-T., Ziari, M., Butrie, T., Reffle, M., Mitchell, M., Kish, F., and Welch, D. (2012). Terabit/s class InP photonic integrated circuits. *Semiconductor Science and Technology*, 27(9):094003.

Nagpal, P., Lindquist, N. C., Oh, S.-H., and Norris, D. J. (2009). Ultrasmooth patterned metals for plasmonics and metamaterials. *Science*, 325(5940):594–7.

Naik, G. V., Liu, J., Kildishev, A. V., Shalaev, V. M., and Boltasseva, A. (2012). Demonstration of Al:ZnO as a plasmonic component for near-infrared metamaterials. *Proceedings of the National Academy of Sciences of the United States of America*, 109(23):8834–8.

Noginov, M., Zhu, G., Bahoura, M., Small, C. E., Davison, C., Adegoke, J., Drachev, V., Nyga, P., and Shalaev, V. (2006). Enhancement of spontaneous and stimulated emission of a rhodamine 6G dye by an Ag aggregate. *Physical Review B*, 74(18):184203.

Noginov, M. A., Zhu, G., Belgrave, A. M., Bakker, R., Shalaev, V. M., Narimanov, E. E., Stout, S., Herz, E., Suteewong, T., and Wiesner, U. (2009). Demonstration of a spaser-based nanolaser. *Nature*, 460(7259):1110–2.

Novotny, L. and Hecht, B. (2006). *Principles of Nano-Optics*. Cambridge University Press.

O'Neil, A. T., MacVicar, I., Allen, L., and Padgett, M. J. (2002). Intrinsic and Extrinsic Nature of the Orbital Angular Momentum of a Light Beam. *Physical Review Letters*, 88(5):5–8.

Ossicini, S., Pavesi, L., and Priolo, F. (2004). *Light Emitting Silicon for Microphotonics*. Springer-Verlag, Berlin Heidelberg.

Oulton, R. F., Sorger, V. J., Zentgraf, T., Ma, R.-M., Gladden, C., Dai, L., Bartal, G., and Zhang, X. (2009). Plasmon lasers at deep subwavelength scale. *Nature*, 461(7264):629–32.

Pacifici, D., Irrera, A., Franzo, G., Miritello, M., Iancona, F., and Priolo, F. (2003). Erbium-doped Si nanocrystals: optical properties and electroluminescent devices. *Physica E: Low-dimensional Systems and Nanostructures*, 16:331–340.

Padgett, M., Courtial, J., and Allen, L. (2004). Light's Orbital Angular Momentum. *Physics Today*, 57(5):35.

Painter, O., Lee, R. K., Scherer, A., Yariv, A., O'Brien, J. D., Dapkus, P. D., and Kim, I. (1999). Two-Dimensional Photonic Band-Gap Defect Mode Laser. *Science*, 284(5421):1819–1821.

Pavesi, L. (2008). Silicon-Based Light Sources for Silicon Integrated Circuits. *Advances in Optical Technologies*, 2008:1–12.

Pavesi, L., Dal Negro, L., Mazzoleni, C., Franzò, G., and Priolo, F. (2000). Optical gain in silicon nanocrystals. *Nature*, 408(6811):440–4.

Pavesi, L. and Guillot, G. (2006). *Optical Interconnects: The Silicon Approach*. Springer-Verlag, Berlin Heidelberg.

Pavesi, L. and Lockwood, D. J. (2004). *Silicon Photonics*. Springer, Berlin.

Pelton, M., Vučković, J., Solomon, G. S., Scherer, A., and Yamamoto, Y. (2002). Three-Dimensionally Confined Modes in Micropost Microcavities : Quality Factors and Purcell Factors. *IEEE Journal of Quantum Electronics*, 38(2):170–177.

Polman, A., Min, B., Kalkman, J., Kippenberg, T. J., and Vahala, K. J. (2004). Ultralow-threshold erbium-implanted toroidal microlaser on silicon. *Applied Physics Letters*, 84(7):1037.

Priolo, F., Franzo, G., Pacifici, D., Vinciguerra, V., Iacona, F., and Irrera, A. (2001). Role of the energy transfer in the optical properties of undoped and Er-doped interacting Si nanocrystals. *Journal of Applied Physics*, 89(1):264.

Prodan, E. and Nordlander, P. (2003). Structural Tunability of the Plasmon Resonances in Metallic Nanoshells. *Nano Letters*, 3(4):543–547.

Prodan, E., Radloff, C., Halas, N. J., and Nordlander, P. (2003). A Hybridization Model for the Plasmon Response of Complex Nanostructures. *Science*, 302(5644):419–422.

Purcell, E. M. (1946). Spontaneous emission probabilities at radio frequencies. *Physical Review*, 69:681.

Radin, C. (1994). The pinwheel tilings of the plane. *The Annals of Mathematics*, 139(3):661–702.

Rattier, M., Benisty, H., Schwoob, E., Weisbuch, C., Krauss, T. F., Smith, C. J. M., Houdre, R., and Oesterle, U. (2003). Omnidirectional and compact guided light extraction from Archimedean photonic lattices. *Applied Physics Letters*, 83(7):1283.

Rong, H., Jones, R., Liu, A., Cohen, O., Hak, D., Fang, A., and Paniccia, M. (2005). A continuous-wave Raman silicon laser. *Nature*, 433(7027):725–7.

Ruan, J., Fauchet, P. M., Dal Negro, L., Cazzanelli, M., and Pavesi, L. (2003). Stimulated emission in nanocrystalline silicon superlattices. *Applied Physics Letters*, 83(26):5479.

Russell, K. J., Liu, T.-L., Cui, S., and Hu, E. L. (2012). Large spontaneous emission enhancement in plasmonic nanocavities. *Nature Photonics*, 6(7):459–462.

Rybczynski, J., Kempa, K., Herczynski, A., Wang, Y., Naughton, M. J., Ren, Z. F., Huang, Z. P., Cai, D., and Giersig, M. (2007). Subwavelength waveguide for visible light. *Applied Physics Letters*, 90(2):021104.

Saleh, B. E. A. and Teich, M. C. (2007). *Fundamentals of Photonics*. John Wiley & Sons, Inc., Hoboken, NJ.

Schonbrun, E., Tinker, M., Park, W., and Lee, J.-B. (2005). Negative Refraction in a Si-Polymer Photonic Crystal Membrane. *IEEE Photonics Technology Letters*, 17(6):1196–1198.

Schroeder, M. R. (1985). *Number Theory in Science and Communications*. Springer Verlag.

Schubert, E. F., Hunt, N. E. J., Vredenberg, A. M., Harris, T. D., Poate, J. M., Jacobson, D. C., Wong, Y. H., and Zydzik, G. J. (1993). Enhanced photoluminescence SiO2 / Si microcavities by resonant absorption in Er-doped. *Applied Physics Letters*, 63(19):2603–2605.

Senechal (1996). *Quasicrystals and Geometry*. Cambridge Univ Press.

Shalaev, V. M. and Kawata, S. (2006). *Nanophotonics with surface plasmons.* Elsevier Science, 2 edition.

Simon, D. S., Lawrence, N., Trevino, J., Dal Negro, L., and Sergienko, A. V. (2013). High-capacity quantum Fibonacci coding for key distribution. *Physical Review A*, 87(3):032312.

Sivakov, V. A., Voigt, F., Berger, A., Bauer, G., and Christiansen, S. H. (2010). Roughness of silicon nanowire sidewalls and room temperature photoluminescence. *Physical Review B*, 82(12):125446.

Solomon, G., Pelton, M., and Yamamoto, Y. (2000). Modification of Spontaneous Emission of a Single Quantum Dot. *Physica Status Solidi (a)*, 178(1):341–344.

Soref, R. A. (1993). Silicon-Based Optoelectronics. *Proceedings of the IEEE*, 81(12).

Steigerwald, D., Bhat, J., Collins, D., Fletcher, R., Holcomb, M., Ludowise, M., Martin, P., and Rudaz, S. (2002). Illumination with solid state lighting technology. *IEEE Journal of Selected Topics in Quantum Electronics*, 8(2):310–320.

Suhr, T., Gregersen, N., Yvind, K., and Mø rk, J. (2010). Modulation response of nanoLEDs and nanolasers exploiting Purcell enhanced spontaneous emission. *Optics Express*, 18(11):11230–41.

Tian, B., Zheng, X., Kempa, T. J., Fang, Y., Yu, N., Yu, G., Huang, J., and Lieber, C. M. (2007). Coaxial silicon nanowires as solar cells and nanoelectronic power sources. *Nature*, 449(7164):885–9.

Trevino, J. (2013). *Engineering Aperiodic spiral Order For Photonic-Plasmonic Device Applications*. PhD thesis, Boston University.

Trevino, J., Cao, H., and Dal Negro, L. (2011). Circularly symmetric light scattering from nanoplasmonic spirals. *Nano Letters*, 11(5):2008–16.

Trevino, J., Liew, S. F., Noh, H., Cao, H., and Dal Negro, L. (2012). Geometrical structure , multifractal spectra and localized optical modes of aperiodic Vogel spirals. *Optics Express*, 20(3):3015–3033.

Vahala, K. J. (2003). Optical microcavities. *Nature*, 424(6950):839–846.

Vesseur, E. J. R., de Abajo, F. J. G., and Polman, A. (2010). Broadband Purcell enhancement in plasmonic ring cavities. *Physical Review B*, 82(16):165419.

Vesseur, E. J. R. and Polman, A. (2011). Controlled spontaneous emission in plasmonic whispering gallery antennas. *Applied Physics Letters*, 99(23):231112.

Vogel, H. (1979). A better way to construct the sunflower head. *Mathematical Bioscience*, 44(3):179–189.

Vredenberg, A. M., Hunt, N. E. J., Schubert, E. F., Jacobson, D. C., Poate, J. M., and Zydzik, J. (1993). Controlled Atomic Spontaneous Emission from Er in a Transparent Si/SiO2 Microcavity. *Physical Review Letters*, 71(4):517–520.

Vučković, J., Pelton, M., Scherer, A., and Yamamoto, Y. (2002). Optimization of three-dimensional micropost microcavities for cavity quantum electrodynamics. *Physical Review A*, 66(2):023808.

Wang, J., Yang, J.-y., Fazal, I. M., Ahmed, N., Yan, Y., Huang, H., Ren, Y., Yue, Y., Dolinar, S., Tur, M., and Willner, A. E. (2012). Terabit free-space data transmission employing orbital angular momentum multiplexing. *Nature Photonics*, 6(7):488–496.

Wang, Z., Lukyanchuk, B., Hong, M., Lin, Y., and Chong, T. (2004). Energy flow around a small particle investigated by classical Mie theory. *Physical Review B*, 70(3):035418.

Warga, J., Li, R., Basu, S. N., and Dal Negro, L. (2008). Electroluminescence from silicon-rich nitride/silicon superlattice structures. *Applied Physics Letters*, 93(15):151116.

Wierer, J. J., David, A., and Megens, M. M. (2009). III-nitride photonic-crystal light-emitting diodes with high extraction efficiency. *Nature Photonics*, 3(3):163–169.

Wiesmann, C., Bergenek, K., Linder, N., and Schwarz, U. (2009). Photonic crystal LEDs - designing light extraction. *Laser & Photonics Review*, 3(3):262–286.

Wu, M.-L., Lee, Y.-C., Yang, S.-P., Lee, P.-S., and Chang, J.-Y. (2009). Azimuthally isotropic irradiance of GaN-based light-emitting diodes with GaN microlens arrays. *Optics Express*, 17(8):6148–55.

Xu, Q., Schmidt, B., Pradhan, S., and Lipson, M. (2005). Micrometre-scale silicon electro-optic modulator. *Nature*, 435(7040):325–7.

Yamaguchi, I., Matsumura, T., and Kato, J.-I. (2002). Phase-shifting color digital holography. *Optics Letters*, 27(13):1108–10.

Yee, K. (1966). Numerical solution of initial boundary value problems involving Maxwell's equations in isotropic media. *IEEE Transactions on Antennas and Propagation*, 14(3):302–307.

Yerci, S. (2011). *Erbium-doped Amorphous Silicon Nitride Light Emitters for On-Chip Photonics Applications*. PhD thesis, Boston University.

Yerci, S., Li, R., and Dal Negro, L. (2010). Electroluminescence from Er-doped Si-rich silicon nitride light emitting diodes. *Applied Physics Letters*, 97(8):081109.

Yerci, S., Li, R., Kucheyev, S. O., van Buuren, T., Basu, S. N., and Dal Negro, L. (2009). Energy transfer and 1.54μm emission in amorphous silicon nitride films. *Applied Physics Letters*, 95(3):031107.

Yu, N., Genevet, P., Kats, M., Aieta, F., Tetienne, J., Capasso, F., and Gaburro, Z. (2011). Light propagation with phase discontinuities: generalized laws of reflection and refraction. *Science*, 344(6054):333–337.

Zia, R., Schuller, J. A., Chandran, A., and Brongersma, M. L. (2006). Plasmonics : the next chip-scale technology The development of chip-scale electronics and photonics has led to. *Materials Today*, 9(7):20–27.

Zia, R., Selker, M. D., Catrysse, P. B., and Brongersma, M. L. (2004). Geometries and materials for subwavelength surface plasmon modes. *Journal of the Optical Society of America A*, 21(12):2442–6.

CURRICULUM VITAE

Nathaniel Lawrence
8 St. Mary's St.
Boston, MA 02215
nlaw85@bu.edu

EDUCATION

Ph.D., Electrical Engineering Advisor: Prof. Luca Dal Negro	Boston University	Sep 2013
M.S., Electrical Engineering	Boston University	May 2012
B.S. Summa Cum Laude, Physics	University of Richmond	May 2008

JOURNAL PUBLICATIONS

Intonti F, Caselli N, **Lawrence N**, Trevino J, Wiersma D, Dal Negro L. "Near-field distribution and propagation of scattering resonances in Vogel spiral arrays of dielectric nanopillars" *New Journal of Physics* 15 (8), 085023 (2013)

Lawrence N, Dal Negro L. "Radiative rate enhancement in subwavelength plasmonic ring nanocavities" *Nano Letters* 13 (8), 3709-15 (2013)

Simon DS, **Lawrence N**, Trevino J, Dal Negro L, Sergienko AV. "Quantum Key Distribution with Fibonacci Orbital Angular Momentum States." *Physical Review A* 87, 032312 (2013)

Lawrence N, Trevino J, and Dal Negro L. "Control of optical orbital angular momentum by Vogel spiral arrays of metallic nanoparticles," *Optics Letters* 37, 5076-5078 (2012)

Dal Negro L, **Lawrence N**, and Trevino J. "Analytical light scattering and orbital angular momentum spectra of arbitrary Vogel spirals." *Optics Express* 20, 18209-18223 (2012)

Lawrence N, Trevino J, and Dal Negro L. "Aperiodic arrays of active nanopillars for radiation engineering." *Journal of Applied Physics* 111, 113101 (2012)

Pecora EF, **Lawrence N**, Gregg P, Trevino J, Artoni P, Irrera A, Priolo F, Dal Negro L. "Nanopatterning of silicon nanowires for enhancing visible photoluminescence." *Nanoscale* 4 2863-2866 (2012)

Lawrence N, Dal Negro L, "Light scattering, field localization and local density of states in co-axial plasmonic nanowires," *Optics Express* 18, 16120-16132 (2010)

Lawrence N, Kehoe JM, Hoffman DB, Marks CB, Yarbrough JM, Atkinson GM, Register RA, Fasolka MJ, Trawick ML, "Combinatorial Mapping of Substrate Step Edge Effects on Diblock Copolymer Thin Film Morphology and Orientation," *Macromolecular Rapid Communications* 31, (11), 1003, (2010)

Vargo ML, Gulka CP, Gerig JK, Manieri CM, Dattelbaum JD, Marks CB, **Lawrence N**, Trawick ML, and Leopold MC. "Distance Dependence of Electron Transfer Kinetics for Azurin Protein Adsorbed to Monolayer Protected Nanoparticle Film Assemblies" *Langmuir* 26 (1), 560-569 (2010)

CONFERENCE PRESENTATIONS

Lawrence N, Dal Negro L, "Radiation rate enhancement in multilayered photonic and plasmonic nanopillars," *American Physical Society*, Baltimore, MD, (2013)

Lawrence N, Trevino J, Dal Negro L, "Engineering structured light with Vogel arrays of nanoparticles", *American Physical Society*, Baltimore, MD, (2013)

Trevino J, Walsh G, **Lawrence N**, Dal Negro L, "Bandgap analysis and emission enhancement from Aperiodic Vogel Spiral Arrays of dielectric nanopillars", *American Physical Society*, Baltimore, MD, (2013)

Lawrence N, Trevino J, Dal Negro L, "Radiation Engineering with Aperiodic Pillar Arrays", *Materials Research Society*, Boston, MA, (2012)

Lawrence N, Trevino J, Dal Negro L, "Aperiodic Arrays of Active Nanopillars for Radiation Engineering", *Optical Society of America*, Rochester, NY, (2012)

Pecora E, **Lawrence N**, Gregg P, Trevino J, Artoni P, Irrera A, Priolo F, Dal Negro L, "Nanopatterning of optically-active silicon nanowires", *Optical Society of America*, Rochester, NY, (2012)

Lawrence N, Trevino J, Dal Negro L, "Aperiodic Arrays of Active Nanopillars for Radiation Engineering", *American Physical Society*, Boston, MA, (2012)

BOOK CHAPTERS

Dal Negro, L, Trevino, J, **Lawrence, N**, Orbital Angular Momentum in Aperiodic Arrays, in "Singular and Chiral Nanoplasmonics," ed. Zheludev, N. and Boriskina, S., Pan Stanford Publishing, To be published (2013)

Dal Negro, L, Forestiere, C, **Lawrence, N**, Lee, S, Trevino, J, Walsh, G, Aperiodic Order in Nanoplasmonics, in "Plasmonics: Theory and applications," ed. Shahbazyan, T V and Stockman, M I Springer Publishing Company, to be published (2013)

Dal Negro, L, **Lawrence, N**, Trevino, J, Walsh, G, Aperiodic Order in Nanophotonics, in "Optics of Aperiodic Structures: Fundamentals and Applications," ed. Dal Negro, L, Pan Stanford Scientific, to be published (2013)